Ion Channels in Mixed Tethered Bilayer Lipid Membranes

Dissertation zur Erlangung des Grades
"Doktor der Naturwissenschaften"

am Fachbereich Biologie
der Johannes Gutenberg-Universität Mainz

vorgelegt von

Jing Li-Fries

geboren in Beijing, V. R. China

Mainz, July 2007

Table of Contents

1. Introduction

1.1 Biological membranes

1.1.1 Structure and functions

All living organisms consist of cells as the fundamental building block. All cells are surrounded by the plasma membrane. The membrane surrounding the living cell serves several functions such as control of solute permeability and recognition events. These membranes are composed of a two-dimensional lipid bilayer in which peripheral and integral proteins are located. In 1972 Singer and Nicholson[1] presented a fluid mosaic model of the cell membrane which showed the membrane as a fluid-like bilayer in which proteins either embedded in the bilayer or associated with cytoplasmic or extarcellular face are able to move freely (Figure1.1).

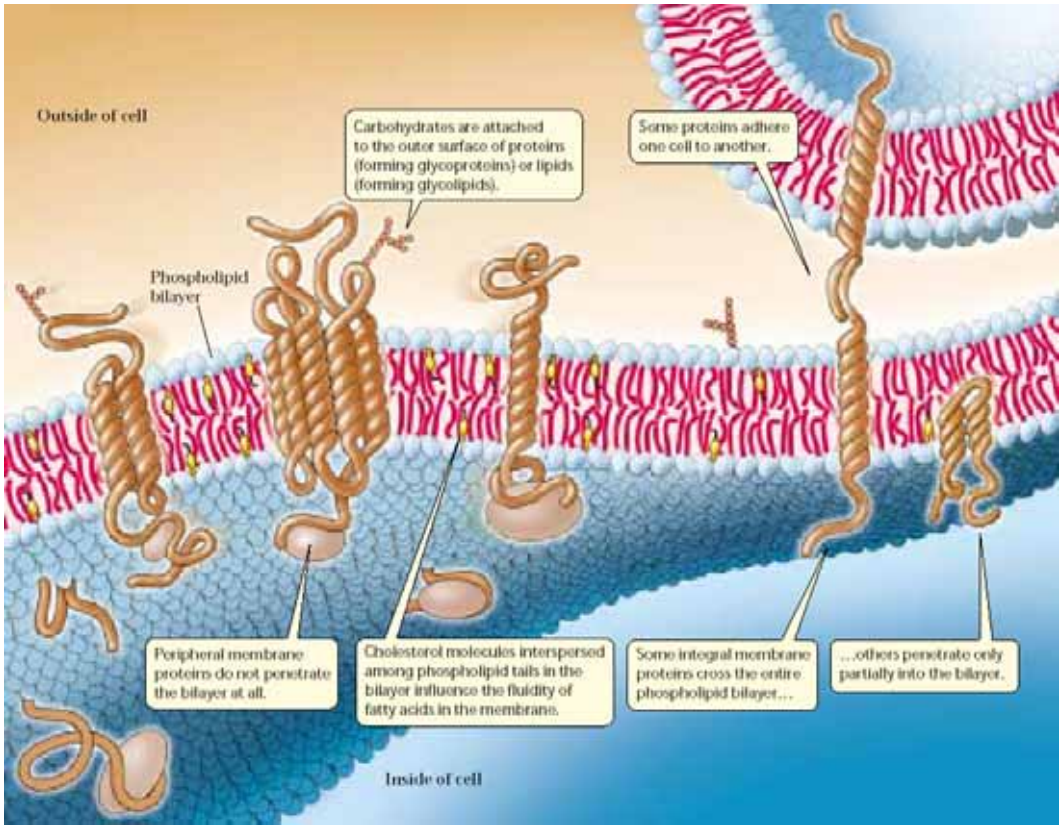

Figure 1.1: *The fluid mosaic model of cell membrane described by Singer & Nicolson*

In this model the concept of peripheral and intergral proteins was introduced. The lipids and proteins were thought to organize randomly through lateral diffusion in the plane of the bilayer, but to have restricted rotational mobility.

The cell membrane keeps the components of the cell isolated from the external environment. The ability provided by the cell membrane to continuously uphold chemical and electrical gradients is a fundamental and necessary capability of life. The membrane itself is actually asymmetric in composition and works as a bipolar electrode. Furthermore, the membrane acts as a supporting matrix for proteins and other functional components of the cell. The cell membrane is also involved in regulating the flow of materials into and out of the cell, mediating intercellular communication and adhesion and a multitude of other functions.

A membrane is a mosaic of different proteins embedded and dispersed in the phospholipid bilayer. These proteins may either attach to cytoskeleton or float freely in lipid bilayer. They define functional characteristics such as membrane transport, cell adhesion, intercellular communication, etc. Membrane proteins can act as enzymes, channels, adhesion molecules. Proteins exhibit many interesting biological and pharmacological activities. To investigate the protein-protein interactions and lipid-protein interactions in the bilayer may lead to a better understanding of many biological processes, such as nerve conduction, mass and information transport, energy conversion or cellular signaling.

1.1.2 The structure and properties of membrane lipids

Most cell membranes are composed of approximately 50 w-% lipids and 50 w-% proteins. Lipids are amphiphilic structures, which consist of a polar head group and an attached hydrophobic hydrocarbon chain (Figure 1.2).

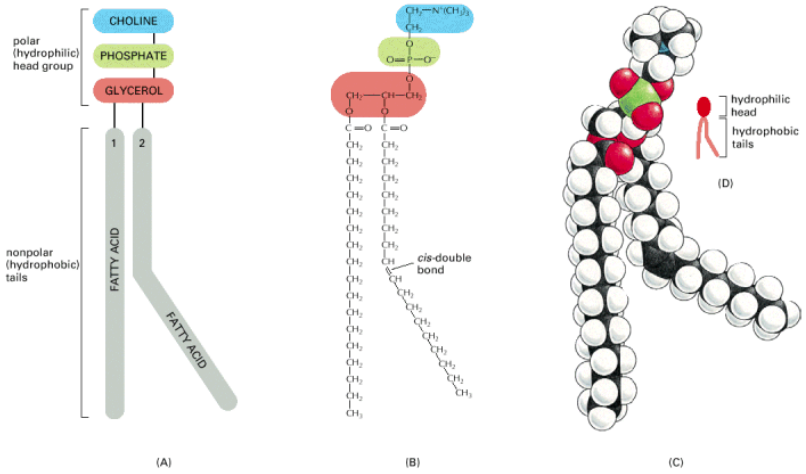

Figure 1.2: *The chemical structure of membrane phospholipids*

Lipids are fats, like oil, and are insoluble in water. There are two important regions of a lipid that provide the structure of the lipid bilayer: the hydrophilic region and hydrophobic region. The hydrophilic region is attracted to aqueous water while the hydrophobic region is repelled from it. Due to their specific structure, phospholipids are allowed to form lipid bilayer membrane and other configurations such as micelles and liposomes. Micelles are relatively small, spherical structures composed of an aggregate of surfactant molecules dispersed in a liquid colloid. They can form when the lipid amount is low relative to water ratio and at the regions of membrane instability. Liposomes are bilayered lipid vesicles formed by hydrating lipids in aqueous solution. Lipid molecules in lipid bilayers can change their conformation, rotate around their molecular axis, diffuse laterally, protrude out of bilayer plane, and flip-flop between the two monolayers[2]. This allows the membranes to be flexible, which is a property required for various modes of their principle functions.

1.2 Model systems of the biological membrane

Artificial lipid membranes are useful models to gain insight into the processes occurring at the cell membrane, such as molecular recognition, signal transduction, ion transport across the membrane. These membranes are often used to characterize

membrane proteins or to study membrane active substances[3-5]. These membranes with incorporated receptors have a great potential in biosensor applications[6-10]. Various methods have been used to create artificial lipid membranes including free suspended membranes as well as membranes supported on a solid surface. Different model systems depicted in Figure 1.3 will be described below.

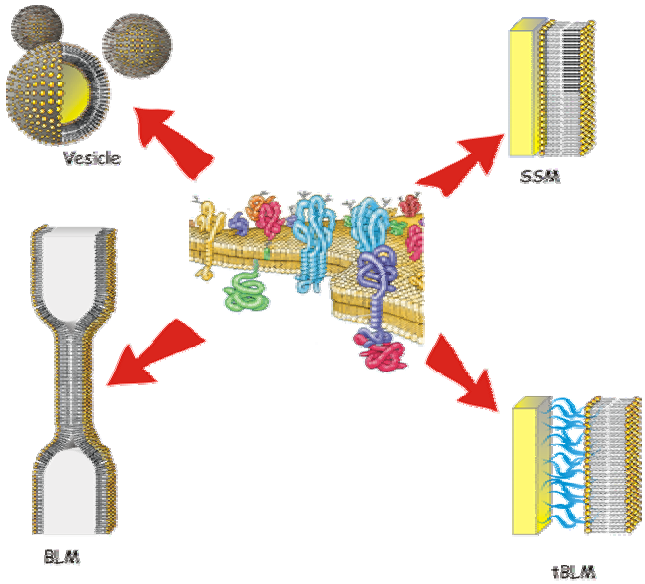

Figure 1.3: *Model systems used in biomimicing of cell membrane*

1.2.1 Liposomes

Liposomes, or lipid vesicles, are spherical structures in which an aqueous volume is enclosed by one or several lipid bilayers. They are usually made from phospholipids, which form energy-favourable structures in an aqueous solution due to the hydrophilic and hydrophobic interactions. Depending on the size and the number of bilayers, liposomes are classified as large multilamellar vesicles (MLV's) or large and small unilamellar vesicles (LUV's and SUV's). The size of unilamellar liposomes vary between 20 nm and 500 nm and the thickness of one lipid bilayer is about 4 nm. The structure of liposomes makes it possible to either encapsulate water-soluble molecules in the water interior of the liposome or immobilise molecules within the lipid membrane.

Liposomes can be modified in a desired manner through the choice of membrane components and this has made them attractive as model system for cell membrane. In addition liposomes are frequently used as a delivery system for anticancer agents, increasing the effectiveness and circulation time of drugs. It is also possible to target specific cells by attaching an appropriate molecule at the liposome surface that binds specifically to the receptor site [11-12].

However, the accessibility to only one side of the membrane limits the usefulness of liposomes for electrochemical approaches, with the exception of pach-clamp measurements. Nevertheless, they appear in various contexts in this work, more often under the name of unilamelar lipid vesicles.

1.2.2 Black lipid membranes (BLM)

In 1962 Müller et al pioneered the work of using black lipid membranes (BLM) as recognition elements[13]. Unlike liposomes, BLMs are originally formed by spreading a lipid solution in a small hole (Ø0.5mm) of a wall separating two aqueous compartments. Evaporation or diffusion of the lipid solvent leads to thinning of the film to its final bilayer state. Black lipid membranes are very suitable for electro-chemical measurements, since there is easy electrochemical access to both sides of the membrane. They have the ability to control the constituents of each side of the membrane. In addition, there is no perturbing surface, and both the membrane and incorporated functionalities are likely to be close to their native state.

The physical stability of these BLMs is very low and much effort has been put on improving the stability of this particular model membrane[14-16]. The residues left from solvent inside the bilayer have affected material properties of the bilayer, such as thickness[17], elasticity[18], and electrical properties[19]. The conduction of incorporated ion-channels is affected as well[20]. It is impossible to form large area BLMs because of the size limitation[21]. Nonetheless they have been extremely valuable in the history of membrane research.

1.2.3 Supported bilayer lipid membranes (sBLM)

An alternative to the BLM is to use lipid bilayers immobilized on a solid support. These membranes can be prepared on various surfaces, i.e., glass, silicon, mica, or on gold surfaces. The standard methods of preparing supported lipid membranes on planar solid surface are the Langmuir-Blodgett (LB) transfer and liposome spreading techniques.

The major advantage of this membrane is its attachment to a solid support, resulting in a long-term and high mechanical stability. Solid supported membranes can be accessed by a variety of sensitive surface analysis tools such as surface plasmon resonance spectroscopy, quartz crystal microbalance, scanning probe microscopy, as well as electrochemical measurements. But their close surface proximity between the artificial membrane and the bare solid surface onto which it is deposited restricts or even prevents the incorporation of large transmembrane-spanning proteins. The membrane-substrate distance is not sufficiently large to avoid direct contact between transmembrane proteins incorporated in the membrane and the solid surface. No ion transport can be detected with such membrane. Because embedded transmembrane proteins often have hydrophilic sections that protrude outside the lipid bilayer and may become immobile or denatured upon contact with the solid support. The lack of a well-defined ionic reservoir on the substrate side of the bilayer is a major drawback when studying membrane transport through ion carriers and channels.

Hybrid bilayers have been developed to improve some of the above-mentioned shortcomings of the solid supported BLMs. In such sBLMs, the first monolayer is typically an alkanethiol monolayer, covalently attached to a metal substrate, onto which a phospholipids monolayeris deposited either by LB transfer or vesicle fusion. Such thiol/lipid solid supported BLMs are stable in air and constitute an improved barrier towards charge transfer[22-23]. However, the rigidity of alkanethiol/phospholipids solid supported BLMs is much higher than that of fluid biological membranes. In addition, the structure of thiol-based solid supported BLMs

prevents the formation of a water layer between the bilayer and the metal support. Because of these conformational restraints, they are unsuitable for the incorporation of integral proteins and studies of ion transport through ionphores[24].

1.2.4 Polymer-supported bilayer lipid membranes (psBLM)

Attempts have been made to separate the membrane from the solid substrate by polymer cushions that rest on the substrate and support the membrane. Strategies include attachment to water-rich gels[25-26], linking with covalently bound spacers[27-31] and hole spanning membranes[32]. A water layer is formed between the support and the hydrophilic headgroups. Tamm[33] and co-worker reported on the successful formation of tethered polymer-supported planar lipid bilayers. In their work a lineare polyethyleneglycol (PEG) polymer was attached at its two ends to the substrate and a lipid molecule, respectively. Polymer-supported BLMs were developed in order to combine the most benefits of unsupported BLMs and solid supported BLM, such as bilayer fluidity and stability, accessibility to various characterization methods, and the possibility of incorporation and investigation of membrane proteins. Polymer-supported BLMs are stable and the presence of a thin, lubricating water layer between the substrate and the inner monolayer allow the incorporation and characterization of proteins. Reviews on the progress in supported membrane research can be found by, *e.g.*, E. Sackman *et al.*[34], R. Tampé *et al.*[35], A. Plant *et al.*[36] and H.T. Tien *et al.*and A.L. Ottova *et al.*[14, 25].

However, these polymer-supported BLMs yield low impedance which is insufficient to match the electrical properties of biological membranes. Lower impedance of such membranes limits the application of polymer-supported BLMs for biosensor purposes. The sealing property of such membrane is not comparable to the BLMs. The defects of the membrane may also prevent the incorporation of channel peptides and proteins. Therefore, another model system should be found to solve these problems.

1.2.5 Tethered bilayer lipid membranes (tBLM)

In an attempt to overcome these drawbacks, while preserving the stability provided by the covalently bound alkanethiol monolayer, so-called thiolipids have been synthesized[30, 37-40]. The thiolipids are composed of lipid derivatives, extended at their polar headgroups by hydrophilic spacers, which terminate in a thiol or disulfide group for covalent binding to the substrate. These molecules interact with gold surfaces, thus forming self-assembled monolayers hydrophobic to the outside. Once exposed to a suspension of liposomes, they tend to fusion and form lipid bilayers tethered to the gold surface by the hydrophilic spacer. Vogel and co-workers[37] were the first to introduce this concept. They synthesized so-called thiolipids with a head group composed of 1-3 ethyleneglycol units acting as a hydrogel and a thiol end group for covalent linkage to the gold surface. Bilayers were formed by depositing a second monolayer of different phosphocholines by the detergent dilution technique. Such bilayers exhibit a very high membrane resistance. Steinem *et al*.[38] used different spacer and vesicle fusion technique to form a bilayer membrane with 0.8-1.0 μFcm^{-2} capacitance. Knoll and co-workers[39,41] were the first to introduce to use oligopeptide sequences as hydrophilic spacers attached to the head group of lipid, resulting in the formation of peptide-tethered bilayers. Cornell and coworkers[6, 30,42-43] were the first using half-membrane spanning tether lipids with benzyl disulphide (DPL) and synthetic archaea analogue full membrane spanning lipids with phytanoly chains to stabilize the structure and polyethyleneglycol units as a hydrophilic spacer. Bilayer formation was achieved by immersion of a gold electrode in an ethanolic solution of the lipid mixture for the outer leaflet. Terrettz et al. employed a thiol compound with a single phytanoic acid and the detergent dilution technique to form the second monolayer of DPhyPC mixed with cholesterol.

Similar approaches using phytanyl containing lipids leading to highly electrically insulating membranes were reported by Schiller *et al*.[44] They described to use ultraflat template stripped gold to deposit tBLMs composed of a monolayer of the thiol-bearing 3-di-*O*-phytanyl-*sn*-glycerol-1-tetraethyleneglycol-D, L-α-lipoic acid

ester lipid (DPTL) (Fig.1.4) and a second monolayer by vesicle fusion of 1,2-diphythanolyl-sn-glycero-3-phosphocholine (DPhyPC).

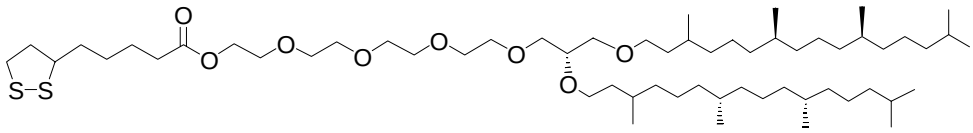

Figure1.4*: Structure of 2,3-di-O-phytanl-sn-glycerol-1-tetraetheylene glycol-DL-α-lipoic acid ester lipid (DPTL) used to build up tethered lipid bilayers.*

DPTL consists of two phytanyl lipid groups attached to a glycerol-tetraethyleneoxy spacer. Both kinds of functionalities are held responsible for the sealing properties of tBLMs prepared from this compound. Tethered bilayer lipid membranes (tBLMs) are produced in such way that the spacer groups provide the possibility of an aqueous compartment between the lipid bilayer and the gold film. Therefore, a water-containing submembrane space which reduces the hydrophobic influence of the metal surface is established[45]. The resulting aqueous phase between the electrode surface and the lipid bilayer has been designed to accommodate extracellular part of transmembrane proteins. This region acts as a reservoir for ions transported across the membrane[6,30,44]. The ionic reservoir can be accessed electrically through connection to the gold electrode. In the presence of an applied potential, ions flow between the reservoir and the external solution when the channel are conductive.

tBLMs can be formed with high insulation electrical properties similar to the biological natural membrane. The capacitance and ionic sealing ability of tBLM based on pure DPTL molecules indicated that the bilayer membranes were comparable to those of solvent-free black (or bilayer) lipid membranes (BLM). Electrochemical impedance spectroscopy was employed to observe the changes in ion conductance induced by the ion carrier valinomycin. But since all the DPTL molecules are tightly bound to the gold surface, the membranes have no possibility for lipids to float freely. The decreased bilayer fluidity possesses a problem particularly for the incorporation of large peptides and channel proteins. Only small ion carrier like valinomycin were effectively incorporated into those tBLM formed by

pure thiolipids. Channel peptides and proteins typically adsorb to the surface of these tBLMs if gold surfaces are used as the support. Channel proteins are hard to incorporate. Thus, an alternative approach should be found so that the larger peptides and channel proteins could be incorporated.

1.3 Motivation

The general purpose of the present work is the development, characterization and application of a biomemmbrane model which could be feasible for the incorporation of channel peptides and proteins so that the functionality of incorporated proteins into such membrane model system can be further used in electrochemical studies. The specific objectives were set as follows:

1. Development. The aim was to develop a model membrane that was stable, reproducible and free from substrate induced defects. Control of membrane composition and state was desirable. The model system was to allow for studies of transmembrane ion transfer.
2. Characterization. The model membrane was to be characterized by surface plasmon resonance spectroscopy, a variety of electrochemical methods to assess its similarity to a biological membrane. In addition, atomic force spectroscopy and quartz crystal microbalance were employed in the characterization of the formation of the bilayers.
3. Application. The applicability of the developed mode system was investigated. The probing of ion transfer, membrane activity of peptides, ion channels were the application of interest. Such model system can be of further use for biosensor applications.

By engineering an ionically conductive submembrane compartment into a thiolipid monolayer, tBLMs provide a biomimetic platform for the investigation of membrane related proteins and processes such as ion transport across the lipid bilayer. As described in the early work[44], pure DPTL molecules were used in preparing a self

assembled monolayer, a tBLM later was then formed via vesicle fusion with high sealing properties which can mimic the electrical properties of biological membrane. But as all the thiolipids are tightly bound to the gold surface, the bilayers formed from pure DPTL SAMs after vesicle fusion have limited fluidity and the bilayer can not freely move, resulting in the difficulty of incorporation of large channel proteins. Only the small ion carrier valinomycin has been shown to be successfully incorporated into tBLM formed from pure DPTL SAM.

To overcome the drawback concerning the tBLMs formed from pure thiolipids, the goal of this thesis is to develop tBLMs based on mixed self-assembled monolayers to achieve the incorporation of channel proteins for biosensor application. In order to achieve the increase of the fluidity of the membrane and the incorporation of channel proteins and other large membrane proteins into tBLMs, spatial dilution of self-assembled monolayer needs to be considered. Thus, we are interested in designing the formation of tBLMs which are less densely packed, but highly insulated, meaning that the tethering molecule in the SAM must be spatially diluted to allow for channel peptides and channel proteins to be incorporated into a bilayer.

The present work will focus on developing a membrane model by use of solutions containing thiolipids and shorter hydrophilic thiol molecules to prepare a mixed self-assemble monolayer in order to dilute monolayers. Vesicles were then fused to complete the assembly to an electrically sealing bilayer.

2. Ion channels

2.1 Overview

Membranes build hydrophobic, low dielectric barriers to hydrophilic and charged molecules from the intracellular to extracellular domains and vice versa, thus they function as electrical insulators. In order to transport ions between the two ionic reservoirs on either side of the plasma membrane, specialized, gated transmembrane proteins, known as ion channels serve to facilitate the diffusion of ions across the biological membrane[46]. Ion channels have many distinct features that make them of interest for biophysical and physiological study. First of all, ion channels are highly ion selective[47]. Secondly, they are dynamic proteins, which demonstrate identifiable responses under specified conditions. Particularly interesting is gated ion channels. At resting potential, the channels are completely closed and impermeable to ion current flow. However, by either a change in the membrane potential or the binding of particular ligands, the channels can be opened. All gated ion channels can be classified as either voltage-gated or ligand-gated to control the opening of the pore and determine which ions will be allowed to pass through the channel pore. Voltage-gated channels usually undergo a conformational change within the membrane due to a particular structure orienting within the electric fields between the membrane bilayer. Ligand-gated channels undergo a conformational change when a particular agonist binds to a receptor site.

In addition to their biological importance, ion channel proteins are particular interesting in the field of biosensors. Immobilization of these proteins at the sensor surface plays an important role in the generation of a functional biosensor. The electrical recordings of ion channel activity provide the most detailed insight into the function of these important membrane proteins. Patch clamp technique on planar lipid bilayer and electrical impedance spectroscopy on artificial or native membranes make it possible to study them in the micro- and nanometer scale. In the present studies, different channel forming peptides and proteins have been tried to incorporate into

mixed tethered lipid bilayer membranes and their activities within the membranes have been investigated. A brief description of each of the proteins is given below.

2.2 α-Hemolysin

α-hemolysins are bacterial toxins from *Staphylococcus aureus* that function by assembling identical subunits into a membrane-spanning pore. Cell lysis (and death) is caused by the leakage of small molecules and ions through the large water-filled central channel. α-hemolysin consists of seven identical subunits arranged around a central axis (Figure 2.1). Seven hairpins associate to form a transmembrane β-barrel of 52Å length and 26Å diameter. The transmembrane part of the lumen is a β-sheet with two antiparallel strands. The extramembraneous domain contains a large cavity that houses the transmembrane domain during the assembly process, which is available for engineering an assembled pore[48]. α-hemolysin is secreted as a monomer, but associated into heptamer at the surface of the target cells. These water-soluble monomers bind to the lipid bilayer before associating to form a nonlytic heptameric prepore[49-50], subsequently, the heptameric membrane-associated species inserts through the bilayer, forming a channel. The channel formed by α-hemolysin allows any kinds of ions to penetrate through the membrane.

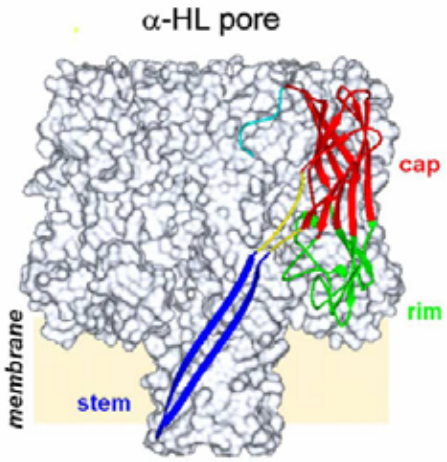

Figure 2.1: *Schematic structure of α-hemolysin pore.*

2.2 Melittin

Melittin, one of the best studied amphipathic α-helical membrane active peptides, was found from the *bee venom of Apis mellifera*[51-52]. It consists of 26 amino acids with a total molecular weight of 2850 Da. This peptide composes of mainly hydrophobic residues and is characterized by six positive charges, four of which are located at the C-termius as Lys-Arg-Lys-Arg. Its molecular structure (Figure 2.2), determined from crystals grown in aqueous solution, is a bent α-helical rod[53]. Depending on conditions such as pH, ionic strength and peptide concentration, melittin is either monomeric α-helices in the membrane interface arranged parallel to the bilayer plane, or tends to form tetramers in solution. Once the melittin bound to the cell surface, it induces lysis of the cell by forming defects in the lipid bilayer.

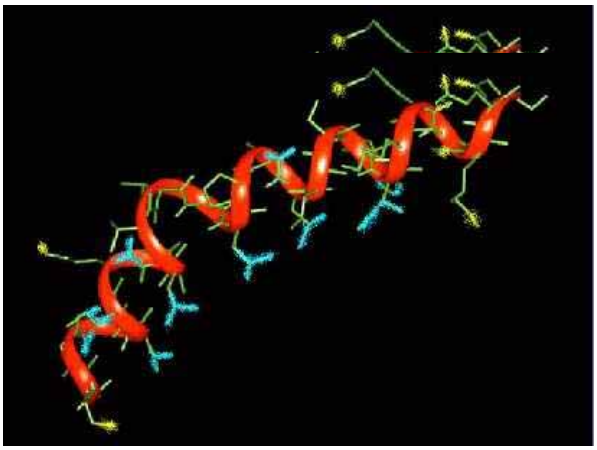

Figure 2.2: *Structure of melittin, simple helical peptide*

2.4 Gramicidin

Gramicidin is a linear peptide produced by *Bacillus brevis*, which consists of 15 alternating L- and D-amino acid residues (Figure 2.3)[54]. In organic solvents, such as methanol, gramicidin exists as a mixture of dimeric forms in equilibrium with monomers[55]. The most abundant species is an antiparallel, left-hand β double helical dimer[56]. However, when two of these helical peptides linked transiently, gramicidin forms a head-to-head single-helix dimer channel to span a lipid bilayer membrane[57].

Gramicidin channels conduct monovalent cations to flow down their electrochemical gradients. Unlike melittin, gramicidin shows conductance specific for particular ions, the gramicidin conductance is dependent on the dimerization constant and on the species and the concentration of ions in the bathing solution, whereas the K^+ and Na^+ ions penetrate the channel, other ions like the bigger tetramethylammonium ($(CH_3)_4N^+$) or ammonium (NH_4^+) ions are excluded.

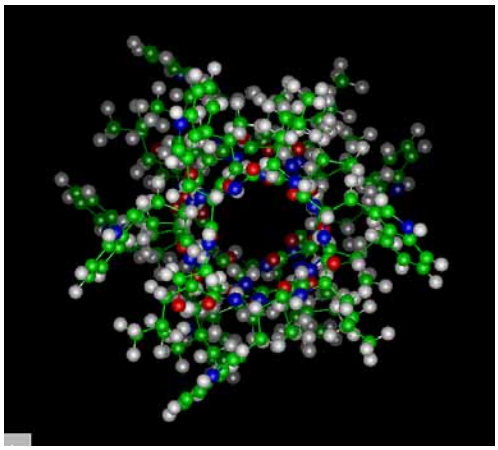

Figure 2.3: *Gramicidin structure*

2.5 M2 channel-forming segment

M2 is the channel-forming transmembrane segment of the nicotinic Acetylcholine Receptor (nAChR). The actual pore forming sequence is small, only 23 to 25 amino acid residues in length. The M2 segments are amphipatic in nature and modeled as a α-helical secondary structure based on electron microscopy studies of intact nAChR. This structure has recently been confirmed for lone M2 segments self-assembled in lipid bilayers by two-dimensional solid-state NMR[58] (Figure 2.4). Although the full nAChR is ligand-gated, the channel formed by the M2 pentamer functions as a voltage-gated channel[59-60]. The hydrophobic portions of the helices face the lipid bilayer and act to anchor the peptides in the bilayer while the hydrophilic portion lines the pore region. When gated open, there is a conformational change in the

orientation of the M2 segments, allowing permeation of ions through the pore. The channel is selective for cations, although it does not discriminate between monvalent cations such as K^+ or Na^+ and even allows permeation of Ca^{2+} to some extent[61].

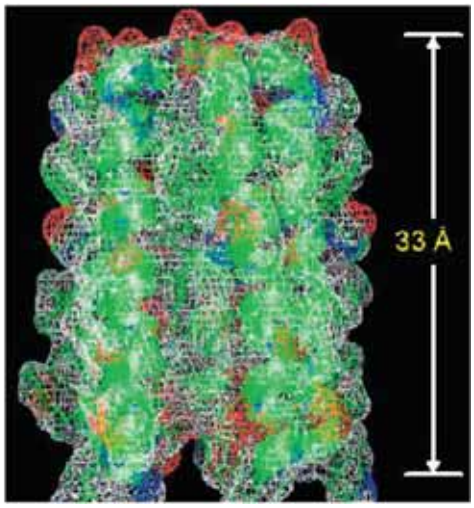

Figure 2.4: *View of M2 Pentamer. Each subunit forms a α-helix and the length of the ion channel is 33Å.*

2.6 Maxi-K channel

The Maxi-K channels are membrane-spanning proteins that selectively conduct K^+ ions across the cell membrane along its electrochemical gradient. These channels compose of six membrane-spanning domains (S1-S6), with a pore region between S5 and S6 (Figure 2.5).

An additional membrane-spanning domain (S0) places the amino terminal outside the plasma membrane. The extended carboxyl terminal tail domain, comprising about two-thirds of the α subunit protein sequence includes a negatively charged region (the so-called calcium bowl) that has been implicated in calcium binding, and is the site of interaction with several channel modulatory proteins. The β subunits are small proteins with two membrane-spanning domains (T1 and T2).

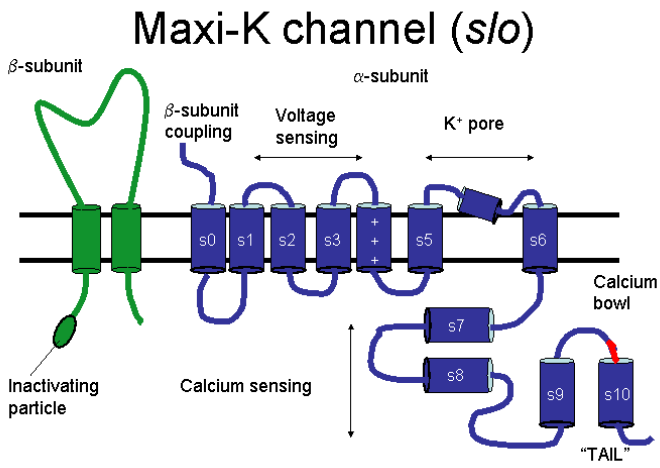

Figure 2.5: *Schematic structure of Maxi-K channel*

Under physiological conditions Maxi-K channels are activated by voltage and an increase in free intracellular calcium concentration. The S4 domain that harbors four to eight positively charged amino acids. This segment experience intense forces in an electrical field, and membrane depolarization drives S4 across the cell membrane from an inner state to an outer state. This displacement is the first step in the sequence of events leading to channel opening[62]. But under low or zero calcium conditions the channel behaviours like a purely voltage-dependent channel[63-64]. Therefore, the voltage-gated mechanism is independent of the binding of calcium to the channel during the activation process, and calcium is not absolutely required to activate Maxi-K channels. However, other reports demonstrate the calcium shifts many of the voltage-dependent parameters of Maxi-K channels to more negative voltages and thereby allows the channel to function under physiological conditions[65-66].

It seems that the voltage dependence of Maxi-K channel is at least in part mediated by the basic residue-studded S4 segment which, as an intrinsic voltage sensor, may be propelled by depolarization and move halfway across the membrane[67], thereby causing further conformation changes that lead to channel opening. But compared with the voltage-dependent K^+ channel α subunits, which contain six transmembrane segments (S1-S6), the Maxi-K channel α subunits have a much larger C-terminal

region, which includes four additional segments (S7-S10) that contain predominantly hydrophobic residues. The tail domain that encompasses the S9 and S10 segments can be expressed separately from the rest of α subunit (the "core") that contains the voltage sensor and the pore-lining structures, and still confer Ca^{2+} sensitivity to the channel formed by the split α subunit[68]. The Ca^{2+} dependence of he Maxi-K channel is affected not only by the tail domain of the α subunit but also by the β subunit, which contains two transmembrane segments [69-71].

These K+ channels play critical roles in cellular signalling processes regulating neurotransimitter release; hear rate; insulin secretion; neuronal excitability; epithelial electrolyte transport; smooth muscle contraction; and cell volume regulation. Their specific sensitivity to a variety of substances that can either prevent or enhance current through these channels give a rise of these channel for therapeutic interventions and applications as biosensors.

2.7 Nicotinic acetycholine receptor

The nicotinic acetylcholine receptor (nAChR) is the neurotransmitter-gated ion channel responsible for the rapid communication between cells at the nerve-muscle synapse and the brain[72-74]. The nAChR is postsynaptic membrane protein composed of five transmembrane subunits, which have large hydrophilic parts that protrude from the membrane in a stoichiometry of $\alpha_2\beta\gamma\delta$ (Figure 2.6). The five subunits are arranged in a circular fashion around a central hole that provides an ion pathway across the postsynaptic cell membrane. Two of the subunits have one binding site each for the transmitter acetylcholine. When acetylcholine is released from the nerve terminal, it binds to the nAChR and induces a conformational change on a distant place in the receptor unit that transiently opens the channel[75]. Among the family of the ligand-gated ion channels, the nAChR is the best characterized. This receptor has been studied in planar lipid membrane[76], black lipid membrane[77], supported lipid membrane[78], and tBLMs[79].

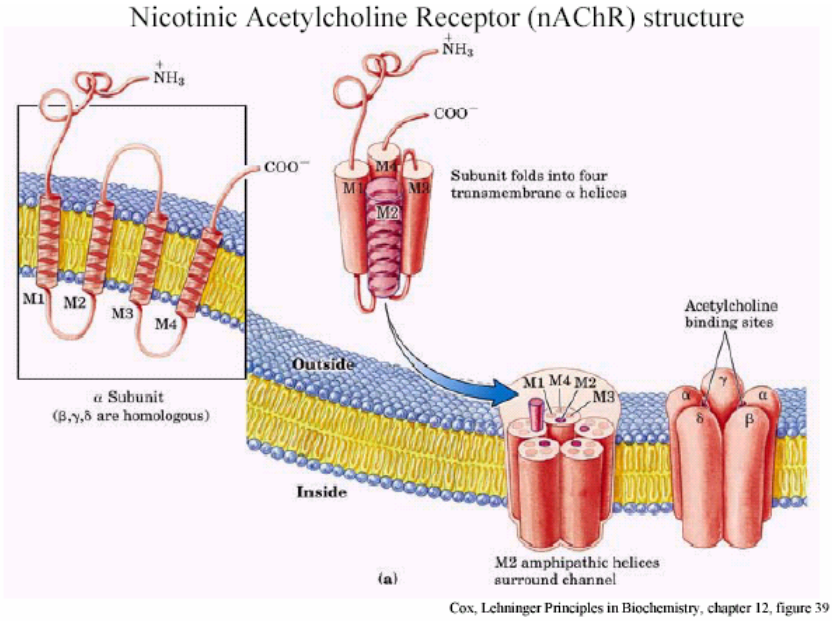

Figure 2.6: Structure of nicotinic acetylcholine receptor

2.8 Bacteriorhodopsin

The purple membrane from *Halobacterium salinarium* (previously *Halobacterium halobium*) contains the protein bacteriorhodopsin (bR), which is organised within the membrane into a two-dimensional hexagonal pattern of trimers. Bacteriorhodopsin is a relatively small protein (MW = 24 000) composed of seven transmembrane α-helices, which are almost fully embedded within the lipid membrane. Bacteriohodopsin is an transmembrane protein. It functions as a light-driven proton pump. Upon illumination, light energy is converted into an electrochemical pH gradient across the cell membrane. The energy generated from this gradient is used for the bacterium's entire cellular metabolism, including the production of ATP for driving chemical processes like biosynthesis.

3. Methods of investigation

3.1 Surface plasmon resonance

Surface Plasmon Resonance (SPR) or Surface Plasmon Resonance Spectroscopy (SPS) for biosensing was first introduced by Lundström and coworkers in 1983[80], although it had already been used for several years to study organic layers on metal surfaces[81-83]. Today, SPR has been widely used as a detection technique in sensors as well as for characterizing molecular interactions at the interface between the analyte and the sensor surface. Many efforts have been directed to the development of various SPR combinations for improving the sensitivity and allowing for quantitative measurement[84-87].

3.1.1 Evanescent light and surface plasmon

The most simple and effective way to illustrate the phenomenon of evanescent light is to employ a classic scheme of total internal reflection of a plane of electromagnetic wave at an interface between materials with different refractive indicies, n_1 and n_2 ($n_1 > n_2$).

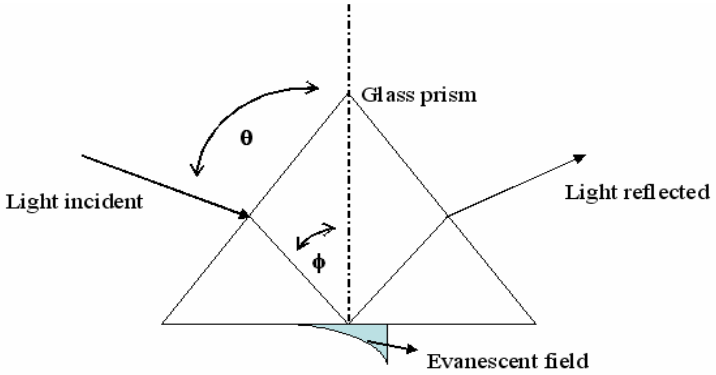

Figure3.1: *Evanescent field excitation using total internal reflection (TIR) mode*

As shown in Fig.3.1, a light beam passes from material with a high refractive index n_1 (e.g. glass) into material with a low refractive index n_2 (e.g. water) some light is reflected from the interface. When the angle at which the light strikes the interface (the angle of incidenceθ) is greater than the critical angle θ_c, the light approaches for

total internal reflectance (TIR). The relationship between the reflected light intensity and the angle of incidence θ is governed by Snell's law and depends on the refractive indices of two media. The critical angle is given by:

$$\sin\theta_c = \frac{n_2}{n_1} \qquad \text{Equ. 1}$$

with $n_1 > n_2$. Monitoring the reflection as a function of the angle of incidence yields the reflection spectrum (with $R = I_r / I_0$, where I_r is the intensity of the reflected and I_0 the intensity of the excitation light, respectively).

However, a more scrutinized examination of the electric field distribution in the immediate vicinity of the interface indicates that when TIR occurs above the critical angle, the light intensity does not disappear completely. Instead, a harmonic wave with an exponentially decaying amplitude perpendicular to the interface is found to be traveling parallel to the surface. Such an electromagnetic field distribution is called an evanescent wave[88]. The decay length *l* which is a function of the angle of incidence is defined by:

$$l = \frac{\lambda}{2\pi\sqrt{(n\cdot\sin\theta)^2 - 1}} \qquad \text{Equ. 2}$$

If the glass surface is coated with a thin conducing film (e.g. gold), this reflection is not total; some of the light is lost into the conducting film shown in Figure 3.2.

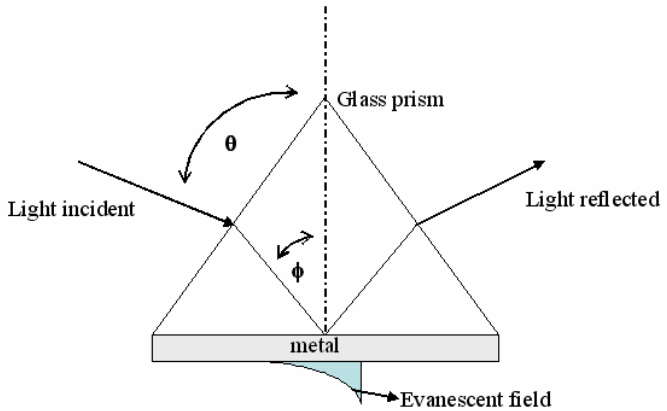

Figure3.2: *SPR occurs when a thin conducting film is placed at the interface between two optical media*

There exists a second angle higher than the critical angle at which this loss is the greatest and at which the intensity of reflected light reaches a minimum. This angle is so called surface plasmon resonance angle (θ_{spr}). It is a consequence of oscillation of plasma at the surface of the metal film. These oscillating plasma waves are called surface plasmons. When the wave vector of the incident light matches the wavelength of the surface plasmons, the electrons resonate. The coupling of the incident light to the surface plasmons results in a loss of energy and therefore a reduction in the intensity of the reflected light. This is because the amplititude of the wave vector in the plane of a metallic film depends on the angle at which it strikes the interface that a θ_{spr} is observed. An evanescent (decaying) electrical field associated with the plasma wave travels for a short distance into the medium from the metal film.

The dispersion relation (i.e. the energy momentum relation) for surface plamons at a metal / dielectric interface is given by:

$$k_x = k_x' + ik_x'' = \frac{\omega}{c}\sqrt{\frac{\varepsilon_m \cdot \varepsilon_d}{\varepsilon_m + \varepsilon_d}} \qquad \text{Equ. 3}$$

Equ.3 has important consequences for the properties of surface plamons. Since ε_m is complex, the wave vector k_x is complex, too because here k_x" represents the damping part of the surface plasmons. Consequently, surface plasmons travelling along a metal/dielectric interface posses a finite propagation length which can be calculated by $L_x = 1/k''_x$. The propagation length limits the lateral resolution of surface plasmon based microscopical methods. In the spectral range of concern we have the following relationship

$$\sqrt{\varepsilon_d} \le \sqrt{\frac{\varepsilon_m \varepsilon_d}{\varepsilon_m + \varepsilon_d}} \qquad \text{Equ. 4}$$

As a consequence, the momentum of a free photon propagating in a dielectric medium given by the following

$$k_{ph} = \frac{\omega}{c}\sqrt{\varepsilon_d} \qquad \text{Equ. 5}$$

will always be smaller than the momentum of a surface plasmon mode propagating along the exact same surface.

Figure 3.3 illustrates the dispersion of photons with the light line (a). In the excitation of surface plasmons, the photon wave vector projection onto the x-direction is the only parameter of concern. This means that in case of reflection of photons at a planar dielectric/metal surface, the curve is tilted from point 0 to point 1 by increasing the angle θ from 0° to the grazing angle. In addition to the energy conservation, the momentum-matching conditions for the resonant surface plasmon excitation can not be sufficiently met because the surface plasmon dispersion curve (Figure 3.3 b) approaches the light line (Figure 3.3 a) asymptotically at very low energies. At higher energies, it reaches a maximum angular frequency ω_{max} determined by the plasmon frequency of the employed material.

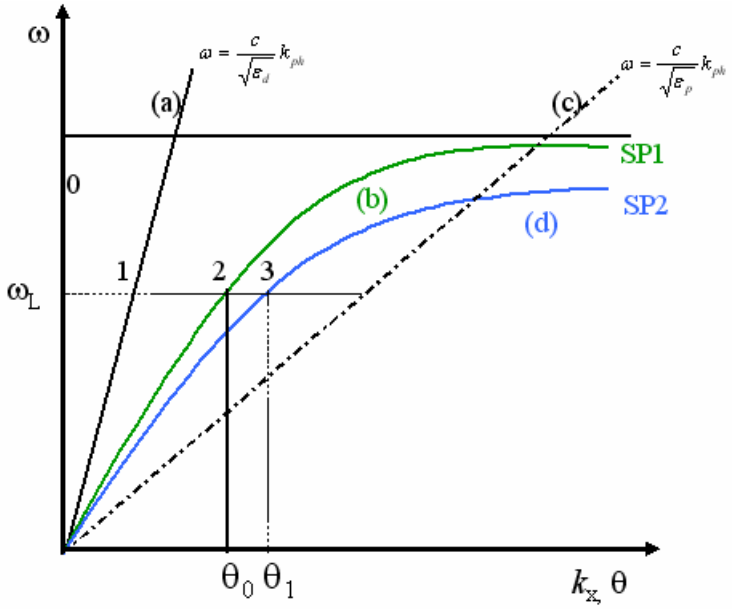

Figure 3.3: *The dispersion relationship for free photons in a dielectric (a), and in a coupling prism (c); surface plasmon at a metal/dielectric interface before (b) and after (d) the adsorption of an additional dielectric layer*

3.1.2 Surface plasmon spectroscopy with prism coupling

The common ways to accelerate the momentum of light are methods based on prism coupling. Using this method, the photons are not directly coupled to the metal/dielectric interface but are instead coupled to the evanescent tail of the light undergoing total internal reflection at the base of a high-index prism (with $\varepsilon_p > \varepsilon_d$). Otto configuration and Kretschmann configuration are two different configurations for exciting surface plasmons by use of a high refractive index prism. In the case of the Otto configuration, (Figure 3.4) the evanescent field bridges a 200 nm wide air gap between the prism and the metal and the plasmons are excited at the metal/air interface[89].

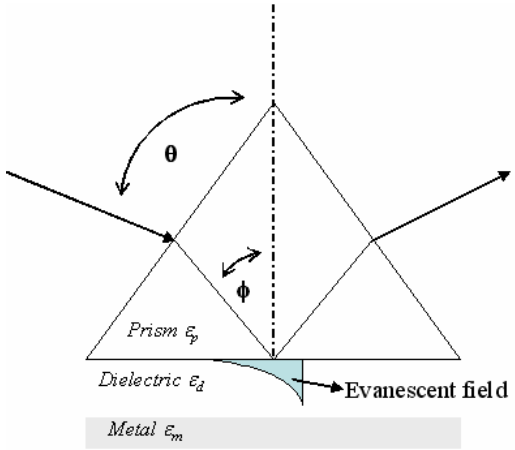

Figure 3.4: *The Otto configuration: total internal reflection of a plane wave incident at an angle θ at the base of a prism. The evanescent tail of this non-homogeneous wave can excite surface plasmon states at metal/dielectric interface if the coupling gap is sufficiently narro.*

Nowadays, the most practical and widespread version of surface plasmon spectroscopy is based on the Kretschmann configuration (Figure3.5)[90]. In Kretschmann-Raecher configuration, a high refractive index prism is coated with a thin gold layer (50nm) adjacent to a low refractive index dielectric. The laser beam is reflected at the base of the prism under an angle of incidence higher than the critical angle. The evanescent field resulting form total internal reflection overlaps with the surface plasmon mode and resonance is achieved by tuning the angle of incidence. When the intensity of reflected light while sweeping through a range of angles is

reached, the plasmon resonance turns up as a sharp dip in the reflectivity spectrum at the resonance angle. The deposition of a thin layer of material with a refractive index larger than that of the dielectric for surface plasmon mode is equivalent to an increase of the overall index integrated over the evanescent field. This results in a shift of the dispersion curve (Figure 3.3) that corresponds to an increase of k_x for any given ωL. As a consequence, the angle of incidence at which the photon wave vector is projected along the propagation direction of the surface plasmons will be increased (from θ at point 2 to θ at point 3 in Figure 3.3) so as to achieve the same resonant coupling to surface plasmon modes.

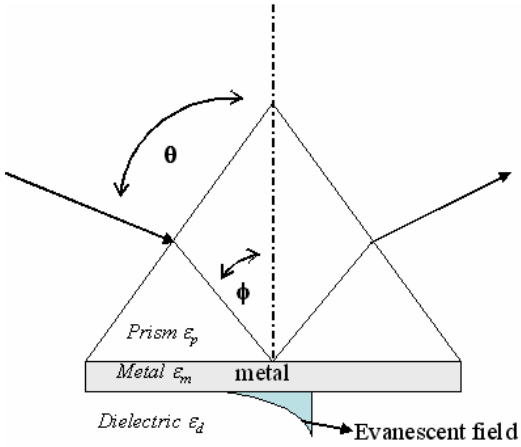

Figure 3.5: *Attenuated total internal reflection setup for SP excitation in the Kretschmann congiguration. A thin metal film (50nm) is evaporated onto the base of the prism and acts as a resonantor driven by the photo field incident at an external angle*

3.1.3 Measuring methods

Scan and the kinetic mode are two commonly used options to record the shift in the resonance angle for surface plasmon excitation induced by changes in interfacial refractive index. A scan curve monitors the intensity of the light reflected at the base of the prism as a function of the angle of incidence. Typical SPR scan spectrum and kinetics scans are illustrated in Figure 3.6.

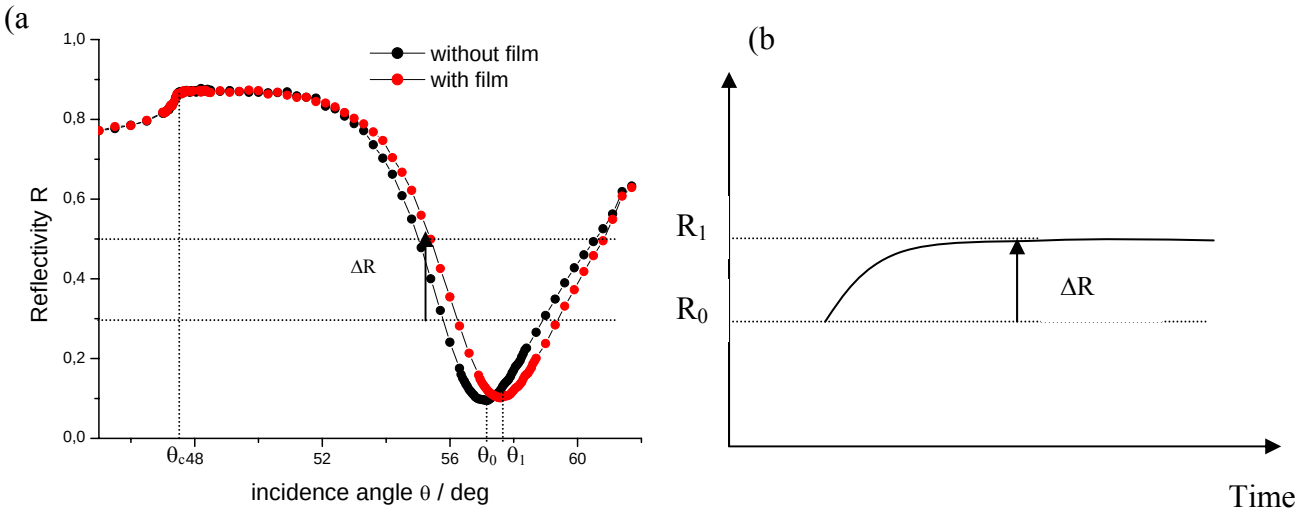

Figure 3.6: *Typical surface plasmon resonance curves. (a) Adsorption of a dielectric film leads to the shift of resonance angle. (b) Kinetic measurement monitors the change in the intensity of the reflected light as a function of time.*

Alternatively, kinetic mode monitors the changes in reflectivity as a function of time at a constant angle. Normally, the angle chosen for kinetic measurement was the one corresponding to 30% reflectivity. The connection between scan and kinetic curves is explained in Figure 3.6. Kinetic measurements allow observing surface reactions in real-time. In this work SPR kinetic measurements were performed to follow the vesicle fusion process to form the 2nd lipid leaflet.

3.2 Electrochemical impedance spectroscopy (EIS)

Electrochemical impedance spectroscopy (EIS) is a powerful tool for examining many chemical and physical processes in solutions as well as solids. For solution phase electrochemistry a complex sequence of coupled processes such as electron transfer, mass transport and chemical reaction can all control or influence the output from an electrochemical measurement[91]. EIS has gained importance in biophysical researches because of its capability in the characterization of dielectric biomaterials or sensor application by transducing signals from organic systems[6]. Impedance spectroscopy is a non-invasive and label-free technique and suitable for the study of ion transport through the bilayer membranes.

3.2.1 Electrical double layer

An ion or charged particle in an electrolyte exerts an influence on its immediate enviornment by virtue of its electric field. This electric field causes dipolar molecules in the immediate vicinity to orientate themselves according to the sign of the charge, like charged ions to be repelled from the area whereas oppositely charged ions experience an attractive potential. As a consequence of the attractive potential counter ions would be expected to approach the charge until the smallest possible distance was achieved. However, the random thermal motion of ions in solution acts against this tendency. This combination of electrical potential energy and thermal energy gives rise to a locally organised region of electrolyte, whereby the ionic distribution in the vicinity of the charge results from the relative magnitudes of the two opposing factors. The resulting locally modified region is referred to the ion atmosphere of the ion. Many solid surfaces acquire a charge through elf ionisation when in contact with an electrolyte. In this case the surface together with its associated structured region of electrolyte is known as the electrical double layer[92-93].

3.2.2 Helmholtz model

A theoretical model of the electrical double layer was first introduced by Helmholtz in 1850´s[94]. He assumed in this model that no electron transfer reactions occurred at the electrode and the solution was composed only of electrolyte. The interaction between ions in solution and the electrode surface were assumed to be electrostatic in nature and resulted from the fact that the electrode holds a charge density (q^m) which arises from either an excess or deficiency of electrons at the electrode surface. For the interface to remain neutral, the charge held on the electrode was balanced by the redistribution of ions close to the electrode surface. The ions approached the electrode surface and formed a layer balanced the electrode charge. The overall result was two layers of charge and a potential drop which is confined to only this region (termed outer Helmholtz Plane OHP) in solution. Helmholtz mode (Fig.3.7) is the simplest mode of the electrical double layer, which was treated as a simple capacitor which hypothesized rigid layers of opposite charges. This model was however inadequate in its explanation of observed electrokinetic effect.

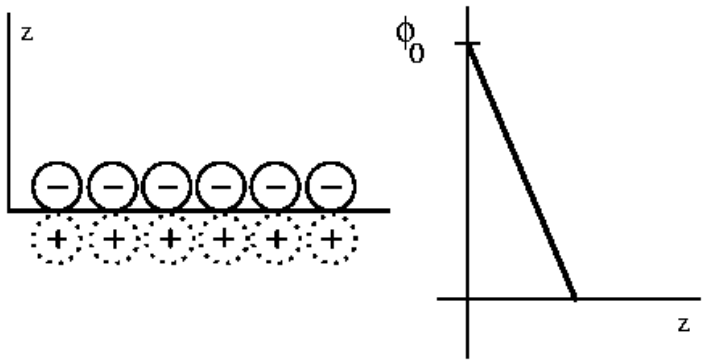

Figure 3.7: *(a) Diagram of the Helmholtz model. The negative ions adsorbed onto the surface are shown with solid lines. The positive ``image'' charges are shown with dotted lines. (b) Potential vs. distance z from the electrode.*

3.2.3 Gouy-Chapman model

In 1910 Gouy[95] and Chapman[96] suggested that interfacial potential at the charged surface could be attributed to the presentation of a number of ions of given sign attached to its surface, and an equal number of ions of opposite charge in the solution (Fig.3.8).

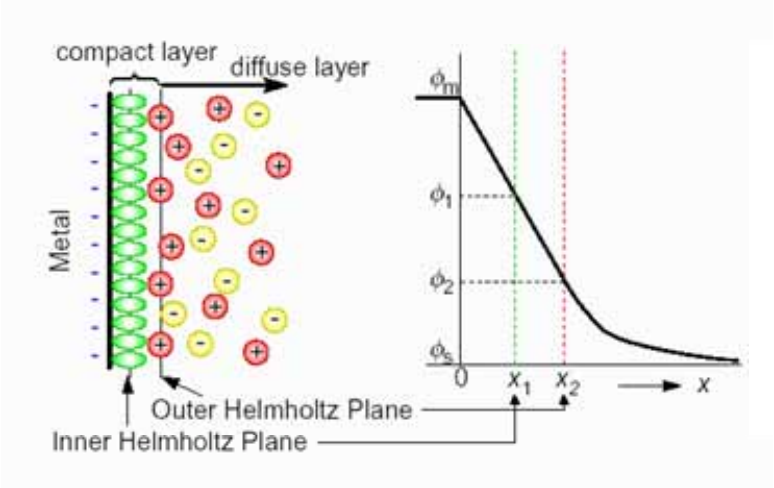

Figure 3.8: *Diagram of the Gouy-Chapman model*

The double layer was considered as a diffuse layer of counter ions, whose concentration decreases with increasing distance from the surface. This view was also to some extent inadequate since, according to this model, unrealistically high concentration of counter ions were predicted at positions close to the surface.

3.2.4 Stern model

The Gouy-Chapmann theory provides a better approximation of reality than does the Helmholtz theory, but it still has limited quantitative application. It assumed that ions behave as point chargesm, which they cannot, and it assumed that there was no physical limits for the ions in their approach to thesurface, which is not true. Therefore, in 1924 Stern[97] combined the Helmholtz single adsorbed layer with the Gouy-Chapman diffuse layer (Fig.3.8).

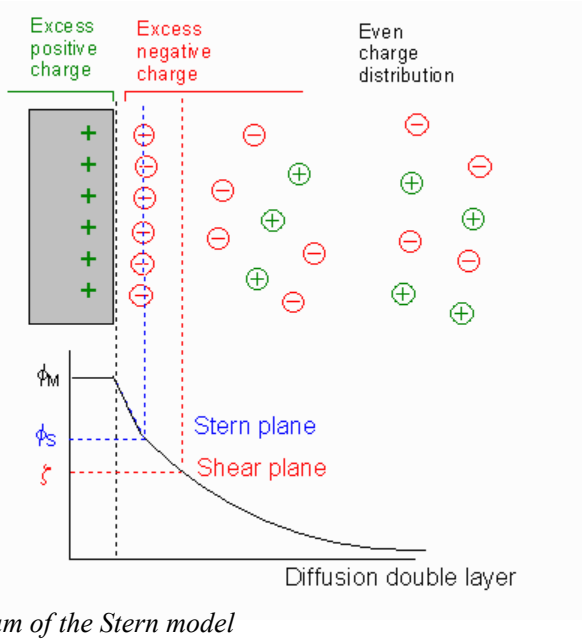

Figure 3.9: *Diagram of the Stern model*

His theory states that ions do have finite size, so can not approach the surface closer than a few nm. The first ions of the Gouy-Chapmann diffuse double layer are not at the surface, but at some distance δ away from the surface. This distance will usually be taken as the radius of the ion. As a result, the potential and concentration of the diffuse part of the layer is low enough to justify treating the ions as point charges. Stern also assumed that it was possible that some of the ions were specifically adsorbed by the surface in the plane δ, and this layer had become known as the Stern layer. Therefore, the potential will drop by $\psi_0 - \psi_\delta$ over the molecular condenser (i.e. the Helmholtz Plane) and by ψ_δ over the diffuse layer. ψ_δ is known as the zeta (ζ) potential.

The only significant interactions were coulombic. The electrical permittivity was constant throughout the double layer and the solvent was uniform at the atomic scale. According to Stern model, the electrical double layer is viewed as consisting of two distinct regions,hereby the excess charges in the electrolyte are distributed between a layer of counter ions (the rigid layer) situated at the shortest possible distance from the charged surface and a diffuse layer.

3.2.5 Electrochemical impedance spectroscopy (EIS)

Electric impedance spectroscopy (EIS) is a routine method of characterizing of various electrical properties (i.e., conductivity, capacitance, and inductance) of materials and their interfaces with electronically conducting electrodes. Additionally, it has been used to investigate the dynamics of bound or mobile charge in the bulk or interfacial regions of any kind of solid or liquid material: ionic, semi conducting, mixed electronic-ionic, and even insulators (dielectrics). EIS is a transient technique, the system under study is perturbed by a pulse or a periodical signal and the relaxation (i.e., the response as a function of time) resulting in a new equilibrium or steady state is analyzed to extract the desired kinetic information.

3.2.5.1 Basics of electric impedance spectroscopy (EIS)

The concept of electrical resistance is based on the ability of circuit elements to resist the flow of electrical current. The Ohm's law defines resistance, R, in terms of voltage, E, and current, I, ratio:

$$R = \frac{E}{I} \qquad \text{Equ. 6}$$

Like resistance, impedance is measure of the ability of a circuit to resist the flow of electrical current (Fig.3.10). It differs from resistance in two significant aspects. First, it's an alternating current (AC) phenomenon; second, it is usually specified at a particular frequency.

The impedance is normally measured by applying an AC potential to an electrochemical cell and measuring the current through the cell. The response to a sinusoidal potential is sinusoid at the same frequency but shifted in phase. Through the measured resistance by the impedance spectroscopy with AC voltage, the information about the conductivity can be obtained.

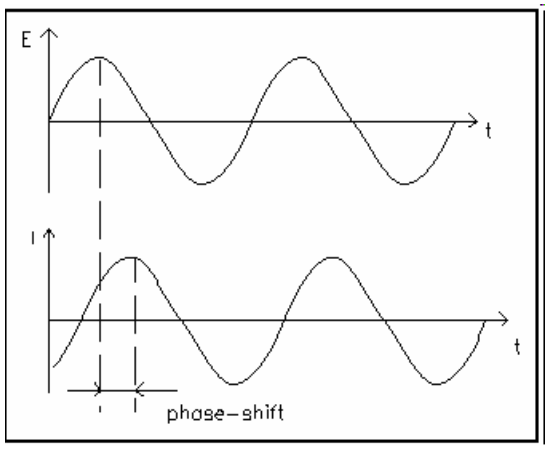

Figure 3.10: *Current and voltage as a function of time. The current response is shift in time.*

The excitation or input signal expressed as a function of time is:

$$E(t) = E_0 \cos(\omega t) \qquad \text{Equ. 7}$$

where *E(t)* is the potential at time t, E_0 is the amplitude of the signal, and ω is the radial frequency $\omega = 2\pi f$ and f is a frequency expressed in Hertz (Hz). In the linear system, the response or output signal *I(t)* with amplititude I_0 is shifted in phase

$$I(t) = I_0 \cos(\omega t - \varphi) \qquad \text{Equ. 8}$$

An expression analogous to Ohm's law allows us to calculate the impedance of the system as:

$$Z = \frac{E(t)}{I(t)} = \frac{E_0 \cos(\omega t)}{I_0 \cos(\omega t - \varphi)} = Z_0 \frac{\cos(\omega t)}{\cos(\omega t - \varphi)} \qquad \text{Equ. 9}$$

The impedance is therefore expressed in terms of a magnitude, Z_0, and a phase shift, *f*. Using Euler's relationship, the impedance is then represented as a complex number

$$\begin{aligned} Z &= \frac{E(t)}{I(t)} = \frac{E_0 \exp(j\omega t)}{I_0 \exp(j\omega t - j\varphi)} = Z_0 \exp(j\varphi) \\ &= Z_0(\cos\varphi + j\sin\varphi) \end{aligned} \qquad \text{Equ. 10}$$

Accordingly, the impedance is a vector quantity since it has a magnitude, Z_0, and direction given by phase shift, θ. The impedance vector, |Z|, in complex plane (Nyquist impedance plot) is described by two components, real, Z', and imaginary, Z".

The real part of Z'is in the direction of the real axis *x*, and the imaginary part is belong to the *y* axis. An impedance $|Z| = Z'+jZ''$ can be plotted in the plane with either rectangular or polar coordinated, as shown in Figure 3.11.

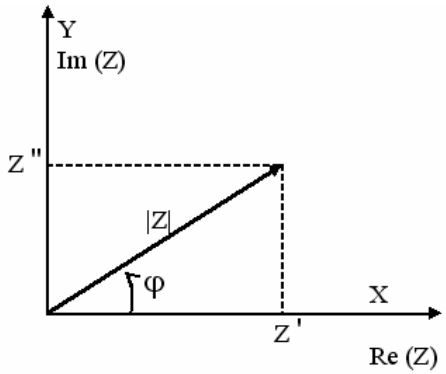

Figure 3.11: *The impedance Z plotted as a planar vector using rectangular and polar coordinates*

Here the two rectangular coordinate values are given as follows:

$$\mathrm{Re}(Z) = Z' = |Z| \cdot \cos\varphi$$
$$\mathrm{Im}(Z) = Z'' = |Z| \cdot \sin\varphi \qquad \text{Equ. 11}$$

with the phase angle

$$\varphi = \tan^{-1}(Z''/Z') \qquad \text{Equ. 12}$$

and the impedance can be calculated from the vector length |Z|

$$|Z| = \sqrt{(Z')^2 + (Z'')^2} \qquad \text{Equ. 13}$$

3.2.5.2 Impedance spectra

Data from impedance measurement can be expressed either in the Nyquist plot, the Bode plot, or in the admittance plot. The impedance Z, and the admittance Y, are usually described by complex numbers, whose real and imaginary parts represent their components for a phase delay of 0° and 90°, respectively.

- ***Nyquist-Plot***

A Nyquist plot is a parametric plot of the real and imaginary parts of the transfer function in the complex plane as the frequency is swept over a given range. If one plots the real part on the X axis and the imaginary part on the Y axis, the representation of the impedance at each frequency can be obtained, meaning that each point on the plot is the impedance at a particular frequency. Figure 3.12 shows a typical Nyquist plot for a resistor and capacitor in parallel.

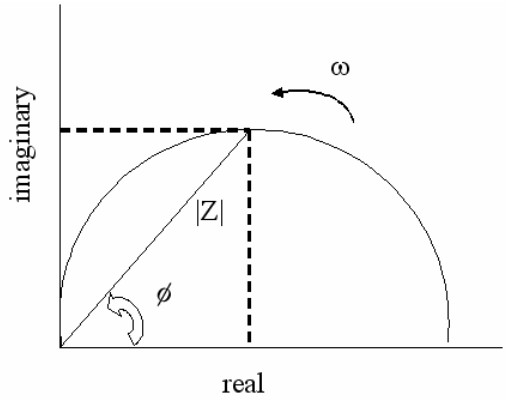

Figure 3.12: *The Nyquist plot provides a representation of impedance at each frequency*

The disadvantage of the Nyquist plot is that it can not provide information on frequency. Therefore, it is impossible to tell what frequency was used for particular impedance. For this reason, Nyquist plots are usually supplemented with other plots.

- ***Bode-Plot***

Another common presentation is the Bode plot. In a Bode impedance plot, the absolute magnitude of impedance is plotted against the frequency *f* or logarithm of

frequency, whereas a graph of phase angle versus the frequency or logarithm of frequency gives a Bode phase plot. In this case, the log of frequency is plotted on the X axis and both the absolute value of the impedance |Z| and phase shift are plotted on the Y axis. The Bode plot (Fig.3.13) presents impedance and phase shift as a function of frequency. Usually, the Nyquist plots and Bode plots are used together to understand a sensor element's transfer function.

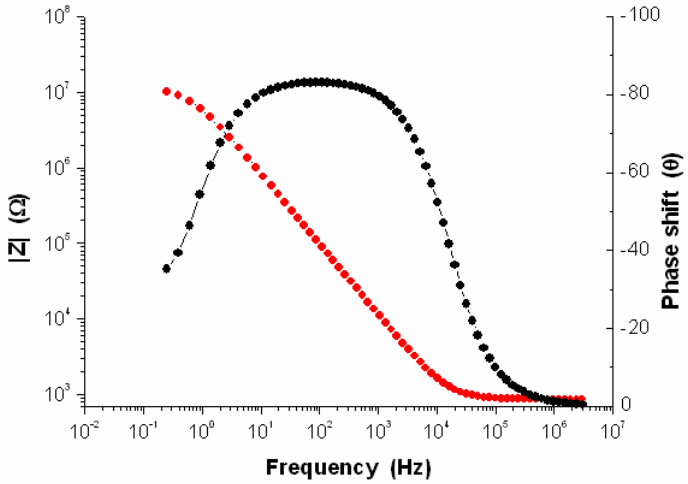

Figure 3.13: *Bode plots can examine both phaseshift and imdepance as a function of frequency*

- ***Complex Admittance (frequency normalized): High-frequency bias***

The advantage to analyze AC circuit in terms of the admittance Y, which is the inverse impedance Y=1/Z, and therefore represents a kind of conductance (Fig.3.14). The complex admittance Y and impedance Z hold the relation

$$Y = \frac{1}{Z} = Y' + jY'' = G + G_a + j\omega C \qquad \text{Equ. 14}$$

where the G is conductance and G_a is the conductance of electrolyte.The real part and imaginary part of adminttance can be obtained from

$$Y' = \frac{Z'}{(Z')^2 + (Z'')^2}$$
$$Y'' = \frac{-Z''}{(Z')^2 + (Z'')^2} \qquad \text{Equ. 15}$$

Variation of the AC frequency, ω (*f*), results in different figure in complex plane corresponding to changes in the ratio between real and imaginary components of the admittance.

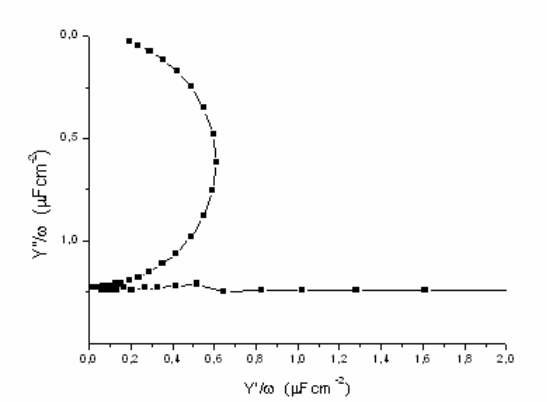

Figure 3.14: *Schematic of complex admittance. The capacitance of the system can be read directly from the graph.*

Equivalent circuits

Interpretation of EIS data is based on the combination of equivalent circuits composed of resistors and capacitors. The real and imaginary parts of the impedance and admittance of basic circuit elements are given in Table 3.1.

	Z_r[a]	$\|Z_i\|$[b]	Y_r[c]	Y_i[d]
Resistor	R	0	1/R	0
Capacitor	0	$1/\omega C$	0	ωC
RC parallel	$R/1+\omega^2R^2C^2$	$\omega CR^2/1+\omega^2R^2C^2$	1/R	ωC
RC series	R	$1/\omega C$	$R\omega^2C^2/1+\omega^2R^2C^2$	$\omega C/1+\omega^2R^2C^2$

Table 3.1: *Definition of the impedance Z and the admittance Y*

Notes: a means real part of the impedance
b means absolute value of the imaginary part of the impedance
c means real part of the admittance
d mean imaginary part of the admittance

3.3 Contact angle

The contact angles of liquid on solids are widely used to predict wetting and adhesion properties of these solids by calculating their solid-vapor surface tensions[98-100]. It can be defined as the angle between a solid surface and the tangent of the liquid-vapor interface of a liquid drop[101]. Contact angle, θ, is a quantitative measure of the wetting of a solid by a liquid. The possibility of estimating solid surface tensions from contact angles relies on a relation which has been reported by Young in 1805[102].

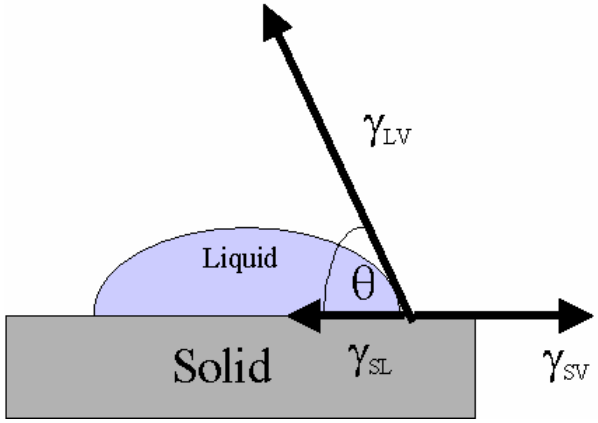

Figure 3.15: *Schematic of a sessile –drop contact angle system*

The contact angle (Fig.3.15) of a liquid drop on a solid surface is defined by the mechanical equilibrium of the drop under the action of three interfacial tensions: solid-vapor γ_{sv}, solid-liquid γ_{sl}, and liquid-vapor γ_{lv}. The equilibrium is described as Young's equation:

$$\gamma_{sv} - \gamma_{sl} = \gamma_{lv} \cos\theta \qquad \text{Equ. 16}$$

where θ is the contact angle. In words, this equation states that the surface free energy of the solid minus the interfacial free energy between the solid and the liquid is equal to the surface free energy of the liquid times the cosine of the contact angle.

Using the contact angle to estimate the solid-vapor and solid-liquid interfacial tension is because of the relative ease with that contact angle can be measured on suitable prepared solid surfaces. It can be seen from Figure 3.16 that low values of θ

indicate that the liquid spreads, or wets well, while high values indicate poor wetting. If the angle θ is less than 90, the liquid is said to wet the solid. If it is greater than 90, it is said to be non-wetting. A zero contact angle indicates complete wetting.

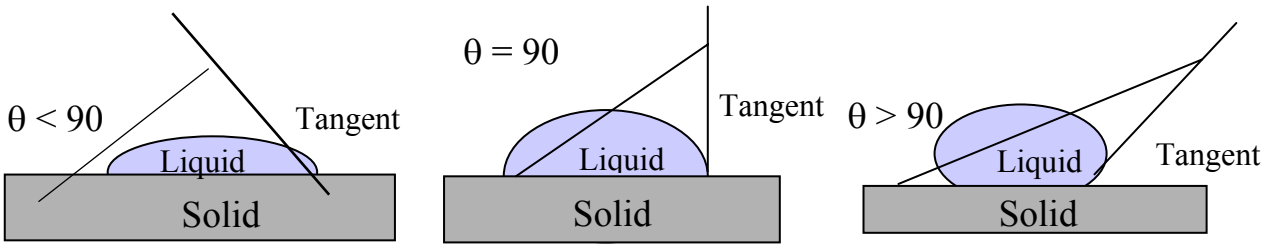

Figure 3.16: *Schematic of the angle formed by a liquid at three.phase boundary(liquid/gas/solid)*

On extremely hydrophilic surfaces, a water droplet will completely spread. This occurs for surfaces that have a large affinity for water. On highly hydrophobic surfaces, which are incompatible with water, water droplets are repelled.

Two different approaches are commonly used to measure the contact angle of non-porous solids, goniometry and tensiometry. Goniometry involves the observation of a sessile drop of test liquid on a solid substrate. Tensiometry involves measuring the forces of interaction as a solid is contacted with a test liquid. In this work, the first approach has been applied to determine the contact angle. The measurement of the static contact angle will help to define the properties of the monolayer which has an influence on the formation of the good bilayer. The information of a lipid bilayer is only possible by vesicle fusion on a highly hydrophobic surface (θ > 80°).

3.4 Atomic force microscopy (AFM)

The atomic force microscopy (AFM) or scanning force microscopy (SFM) was invented in 1986 by Binning, Quate, and Gerber[103], which belongs to the vast family of scanning probe microscopy. During the last years, AFM has become a standard tool to investigate the topography of all types of surfaces from a nanometric point of view. Moreover, force spectroscopy mode has made it possible to measure the mechanical properties of the surfaces and the interaction forces that arise between the surface and the measuring probe[104]. Indeed, the intermolecular forces near the surfaces in the nanometer scale play a key role in a wide range of chemical, biological, and physical processes, such as chemical and physical adsorption, wetting, wear, catalysis, adhesion, cell recognition, etc. The image technique provides three-dimensional images of the surface ultrastructure with molecular resolution, in real time, under physiological conditions, and with minimal sample preparation. Similar to other scanning probe microscope, the AFM images a surface by scanning a sharp tip attached to a cantilever at a close distance to the surface[105]. As one of the frequently used instruments, the sample is mounted on a piezoelectric scanner, which is most often in the form of a tube scanner and capable of nanoscopic resolution in three-dimensional positioning. The force is measured by detecting the bending or deflection of the cantilever during scanning. The larger the cantilever repulsion, the higher the force that will be experienced by the probe[106]. The deflection of the cantilever is detected by employing an optical lever technique.

As illustrated in Fig.3.17, a laser beam is focused on the free end of the cantilever, and the position of the reflected beam is detected by a photodiode. The cantilevers and probes used for AFM imaging are made of silicon or silicon nitride by microfabrication technique.

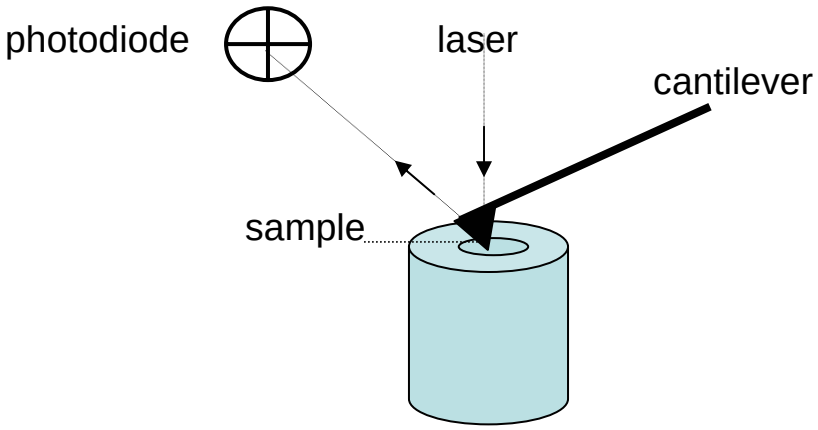

Figure 3.17: *Schematic of an AFM measurement in contact mode*

3.4.1 Imaging

AFM can be operated in different modes for imaging or force measurements. A number of AFM imaging modes are possible. The sample or tip is moved both vertically (in Z-direction) and laterally (in X- and Y-directions) by the piezoelectric actuator on which the sample or tip is mounted. The most widely employed imaging modes in the AFM are:

- *Contact mode*. The tip is actually in contact with the sample. The surface structure can be imaged at constant height or at constant force. The height image provides quantitative height measurements, allowing accurate measurement of surface roughness, the height of the surface features, or the thickness of biological layers. The topographic information results from the cantilever deflection or in the constant force mode from feedback current of the z-piezo. One drawback of remaining in contact with the sample is that large lateral forces are existed on the sample.

- *Tapping mode.* The cantilever is oscillated at its resonant frequency and positioned above the surface so that it only taps the surface for a very small fraction of its oscillation period. As the tip scans over the surface, the lateral forces are dramatically reduced. The tapping mode is often used to image poor immobilized or soft samples which are hardly detected by contact mode. The topographic information results from the amplitude damping.

3.4.2 Force measurements

As the cantilever obeys Hooke's Law for small displacement, measuring the interaction force between the AFM tips and the sample by means of force-distance curves, can probe the sample's physical properties. In an AFM force measurement, the tip attached to a cantilever is moved towards the sample in normal direction. Vertical position of the tip and deflection of the cantilever caused by force between the tip and the sample are recorded (Fig.3.18).

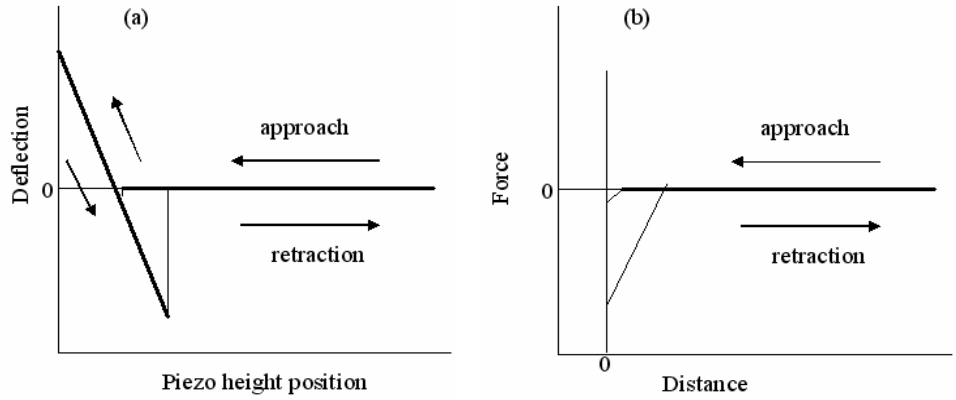

Figure 3.18: *(a).cantilever deflection vs. piezo position curve. (b). force vs. distance curve*

The result of such a measurement is a curve, which shows the cantilever deflection versus displacement. By using appropriate calculation of multiplying the cantilever deflection with the spring constant, one can obtain the force, and by subtracting the cantilever deflection from the height position, one can obtain the distance.

A wealth of information can be obtained from the different parts of a force-distance curve. As the tip approaches the surface, the cantilever may bend upwards because of the repulsive force until it jumps into constant distance when the gradient of attractive forces exceeds the spring constant plus the gradient of the repulsive force. The approach portion of the force-distance curve can be used to measure the forces, including Van der Waals force, electrostatic Coulombic interactions, solvation forces[107] and hydrogen bonding[108]. When the probe is retracted from the surface, the curve often shows a hysteresis referred to as the adhesion "pull-off" force, which can be used to estimate the surface energy of solids or the binding forces between complementary molecules[109]. The force-distance curve is used in this work to determine the thickness of mixed monolayer and bilayer formation.

3.5 Quartz crystal microbalance (QCM)

The quartz crystal microbalance (QCM) is a mass sensing device with the ability to measure very small mass changes on a quartz crystal resonator in real time. The QCM is capable of measuring mass changes as small as a fraction of a monolayer or single layer of atoms. The high sensitivity and the real time monitoring mass changes on the sensor crystal make QCM a very attractive technique for a large range of applications, as a sensor in thin film thickness monitoring, biochemistry and biotechnology, drug delivery and drug research. The use of QCM transducer offers an in-situ sensitive detection without the need for optical or redox indicators.

The physical basis of operation of QCM originates in the converse piezoelectric effect, in which the application of an electric field across a piezoelectric material induces a deformation of the material. In 1880 Jacques and Pierre Curie discovered the piezoelectric effect. It was that mechanical stress applied to the surface of acentric material such as quartz, resulted in an electrical potential across the crystal, whose magnitude was proportional to the applied stress. This effect is appearing since a single crystal of an acentric material possesses a polar axis due to dipoles associated with the arrangement of atoms in the crystalline lattice. Under mechanical stress the physical displacement of the atoms occurs, so the corresponding change in the net dipole moment takes place and as a result charge is generated in a crystal.

The quartz crystal commonly used for QCM application is cut in an angle of $\theta = 35°$ from the crystallographic zx- plane, which is referred to as AT-cut. The heart of the QCM is the piezoelectric AT-cut quartz crystal sandwiched between a pair of electrodes. Ideally, AT-cut quartz oscillates exhibiting a pure shear motion of the surfaces. The surfaces move parallel with respect to each other and the thickness of the plate does not change, i.e., there is no normal component. But when the electrodes are connected to an oscillator, due to the piezoelectric effect of the quartz crystal, the application of a voltage across the crystals resulted in a corresponding mechanical

strain. In Figure 3.19 the schematic representation of the converse piezoelectric effect for shear mode is shown.

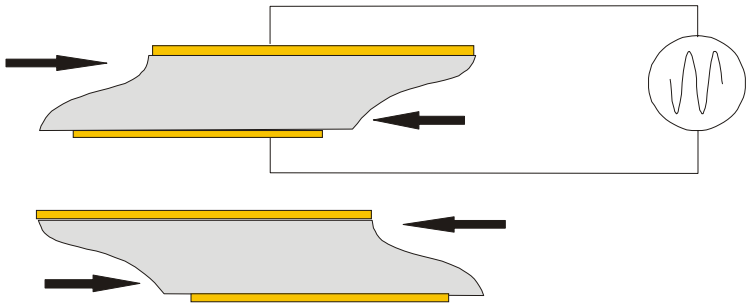

Figure 3.19: *An AT-cut quartz crystal deforms in shear mode when an electric potential applied*

The electric field induces the reorientation of the dipoles of the quartz, resulting a lattice strain and shear deformation at a given resonance frequency. The direction of the shear is dependent on the applied potential and the extent of the shear strain depends on the magnitude of the applied potential. The opposite polarity produces an identical strain but in the opposite direction. The result of the vibration motion of the quartz crystal leads to a transverse acoustic wave which propagates across the crystal and reflects back into the crystal at the surface. The surface electrodes can excite only odd harmonics, n=1, 3, 5, 7…. when a foreign mass layer is deposited rigidly and uniformly on the crystal surface. A standing wave condition is generated when the acoustic wavelength is equal to twice the thickness of the crystal. Therefore, the resonance frequency can be related to the thickness of the crystal by the following equation:

$$f_n = n \cdot f_0$$

$$f_0 = \frac{c_t}{\lambda} = \frac{c_t}{2d_q} \qquad \text{Equ. 17}$$

where c_t is the transversal velocity of sound, dq the thickness of the quartz plate, λ the wavelength and n is an odd overtone (n=1, 3, 5,7…). The thickness of the quartz plate d_q determines the fundamental frequency f_0 of the shear motion by defining the wavelength of the fundamental oscillation. Measured resonance frequency shifts (Δf)

are converted into mass changes (Δm) by the well-known Sauerbrey equation[110]:

$$\Delta m = -\frac{Z_q}{2f_0} \cdot \frac{\Delta f_n}{f_n} \qquad \text{Equ. 18}$$

where Δm are the mass coverage per unit area; Zq = 8.8 x 10^6 kg/ms the acoustic impedance of the quartz; Δf_n the frequency shift with respect to the unload frequency f_n of n^{th} harmonics. Knowing the effective density gives access to the effective thickness by:

$$d_{ac,f} = \frac{\Delta m}{\rho} \qquad \text{Equ. 19}$$

Sauerbrey's equation holds only true if the added mass is significantly smaller than the mass of the quartz crystal. Furthermore, the film has to be homogenous and rigidly attached to the quartz crystal surface. The resonant mechanical oscillations are basically fixed by the crystal thickness, whereas the damping depends on the characteristics of the mounting and surrounding medium.

It is also possible to determine viscoelastic properties of the films adjacent to the quartz surface from the combined evaluation of resonance frequency and dissipation. However, this was not the focus of the present work. In this work the QCM technique were applied to investigate the unrolling and spreading of vesicles to form a tBLM on gold surface, as we take the fusion of vesicles into consideration as a rigid, homogeneous spreading process.

4. The design of mixed tethered bilayer lipid membrane

Highly resistive tBLMs based on pure thiolipid with oxyethylene spacers (DPTL) have been obtained[44,111-113]. They have been prepared from a self-assembled monolayer (SAM) of DPTL on the template stripped gold (TSG) surface. Furthermore, the fusion of 1,2-diphythanolyl-sn-glycero-3- phosphocholine (DPhyPC) vesicle gave rise of the formation of a second lipid leaflet, leading to the formation of a complete, well-defined lipid bilayer[111]. But such tBLMs are exclusively designed to incorporate small ion carriers such as valinomycin. Even small channel peptides adsorb to the surface of these tBLMs[114].

In order to allow for the incorporation of channel peptides and proteins into a bilayer in a functionally active state, the tethering molecule in the SAM must be spatially diluted particularly when gold surfaces are used as the support [6,30,42,43,115]. Previous attempts to dilute monolayers of thiolipids with short hydrophilic thiols, such as mercaptoethanol or lipoic acid, have generally resulted in bilayers with poor electrical properties (i.e. the nonspecific conductivity is too high to observe ion channel behaviour)[116]. Electrical properties of tBLMs are critically dependent on the chemical nature and composition of the self-assembling molecules[117-119].

The tBLMs presented in this thesis are based on self-assembled monolayers of a mixture of two molecules, namely a newly designed hydrophilic thiol tetraethylene glycol-D,L-α-lipoic acid ester (TEGL) provided with a tetraethylene glycol moiety on gold mixed with the previously described archea analogue thiolipid (DPTL)[120-123]. Both components (see Fig.4.1) have the same ethyleneoxy chain close to the substrate, thus providing a disordered hydrophilic environment. The ethyleneoxy spacer unit separates the lipid layer from the gold surface, serving as a reservoir underneath the membrane to prevent the impairment of embedded proteins. The shorter thiol (TEGL) dilution molecules have the same thiol and spacer moiety as the thiolipid (DPTL). The role of the TEGL used in the SAM preparation is to spatially dilute the SAM on the surface so that the density of the bound lipids can be reduced. In addition, these dilution molecules bearing short chain ethoxy groups were found to promote the formation of lipid bilayers, resulting in a highly insulated bilayer after vesicle

fusion as illustrated in Figure 4.2. Compared with the undiluted tBLM architecture, it is envisaged that due to the addition of short spacer molecules among the thiolipids the mixed tBLMs possess some free lipids floating between the tightly bound thiolipids. These shorter spacer molecules make it possible to control the lateral fluidity, diffusivity and function of transmembrane proteins. Thus, the incorporation of large peptides and channel proteins should be facilitated.

In addition, the lipid composition of the vesicles also shows an influence on the fusion process. Composition and molecular shape of the lipids determine the physical properties of the lipid membrane (e.g., membrane fluidity, bilayer thickness, surface charge distribution, and lateral pressure). Consequently, these properties may affect the structure and function of the incorporated ion channels[124-127]. In this work, 1,2-diphythanolyl-sn-glycero-3-phosphocholine (DPhyPC), 1,2-diphytanoyl-sn-glycero-3-phosphate (DPhyPG), and cholesterol have been chosen to prepare mixed liposomes. All the compounds are shown in Figure 4.1. The use of cholesterol in a mixture of different lipids may influence the function of membrane proteins both by binding directly to the proteins and by changing biophysical properties of the lipid membranes. The role of cholesterol here is to promote the formation of the lipid bilayer and stabilize the bilayer. Furthermore, by using liposomes prepared in pure water, additional osmotic shock was utilized to promote the fusion process since a relatively high ionic strengthelectrolyte was used for the bathing solution.

(A)

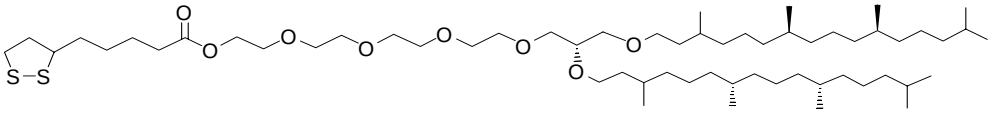

2,3-di-O-phytanyl-sn-glycerol-1-tetraethylen glycol-DL-α-lipoic acid ester (DPTL), tethered molecule, thiolipid

(B)

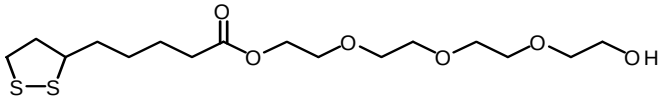

tetraethylene glycol-D,L-α-lipoic acid ester (TEGL), spacer molecule

(C)

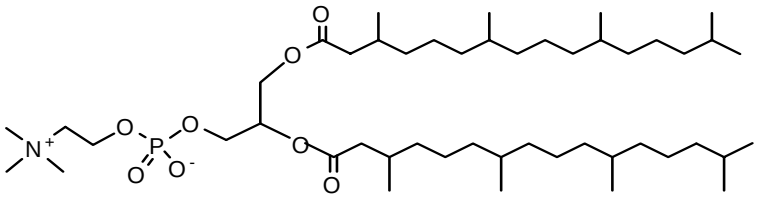

1,2-diphythanolyl-sn-glycero-3- phosphocholine (DPhyPC)

(D)

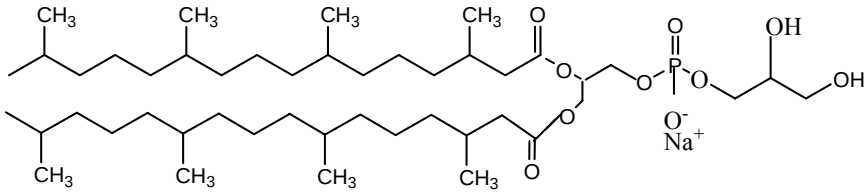

1,2-diphytanoyl-sn-glycero-3-phosphate (DPhyPG)

(E)

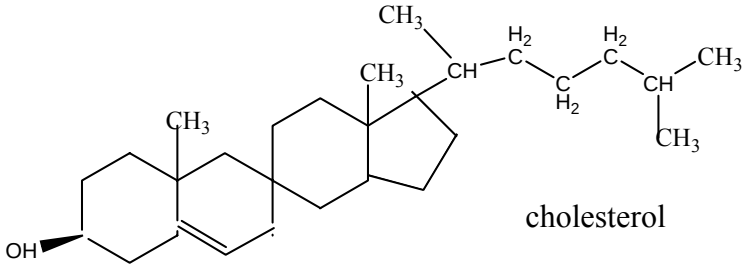

cholesterol

Figure 4.1: *Chemical structure of the components of the mixed tBLM*

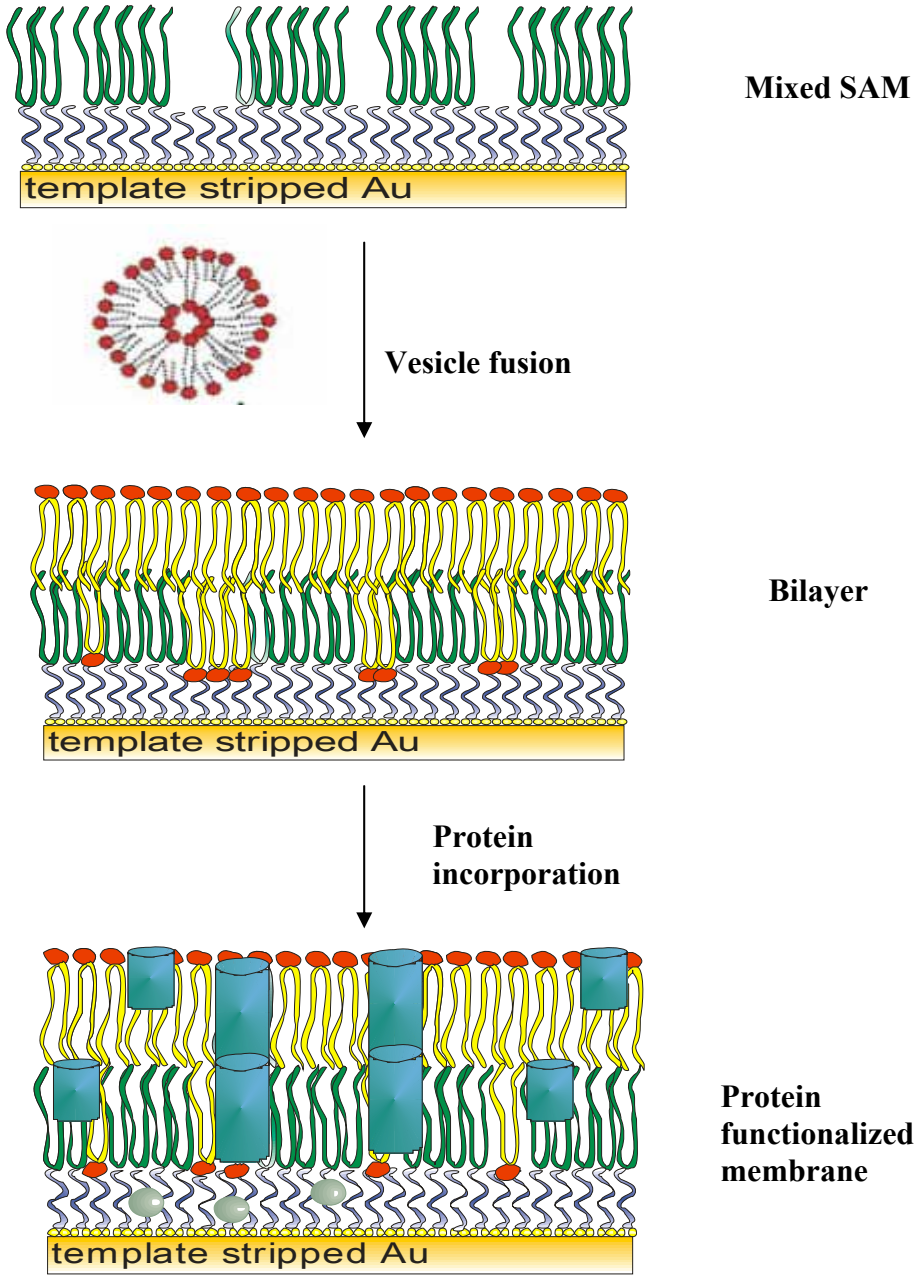

Figure 4.2: *Schematic illustration of the formation of a mixed tethered lipid bilayer membrane with incorporated channel peptide.*

5. Results and discussions

5.1 Principle preparation of mixed tBLMs

The combined set-up for surface plasmon optical investigation of interfacial architectures and their functional characterization by electrochemical instrumentation was used to study the formation and the final structure of the supported lipid layers on gold surface. Our first attempt on the preparation of mixed self-assembled monolayer was done by mixing 90% DPTL with 10% TEGL (molar ratio). The formation of the bilayer was monitored simultaneously by Surface Plasma Resonance Spectroscopy (SPR) and Impedance Spectroscopy (IS).

5.1.1 SPR measurements

Surface Plasma Resonance Spectroscopy (SPR) was used to demonstrate the formation of tethered lipid bilayers deposited on the mixed self-assembled monolayer based on the self-assembled DPTL mixed with TEGL. SPR was performed in a setup as described previously using the Kretschmann-configuration. The glass slide (LaSFN9 glass from Hellma Optik, Jena, refractive index n=1.85 at 633 nm) was optically matched to the base of a 90° glass prism (LaSFN9). Monochromatic light from a He/NeLaser, (Uniphase, San Jose, CA, λ = 632.8 nm) was directed through the prism and collected by a custom made photodiode detector. Based on a fitting routine using the Fresnel equations, the following parameters of the planar multilayer system were evaluated as given in Table 5.1 with ε and d being the dielectric constant and the thickness of the layers, respectively. The parameters d_{gold} , ε_{gold}, and ε_{water} were obtained by a reference scan taken from a clean gold surface of the same thickness. $\varepsilon_{thiolipid}$ is a reasonable assumption from $\varepsilon_{phospholipid}$, which is assumed to be equivalent to a pure alkane. Figure 5.1 shows SPR spectra of TSG in buffer solution on the bare gold and monolayer of the mixed SAM, before and after fusion of a mixture of liposomes, respectively.

Layer	d/nm	ε
Glass	∞	3.14[a]
Gold	~50[b]	-12.1 + i*1.2[a]
Thiolipid	Fitted	2.10[a]
phospholipid	Fitted	2.25[a]
Water (buffer)	∞	1.77[a]

Table 5.1: *optical constants (d = thickness, ε = dielectric constant) used for SPR fitting. [a] obtained from independent sources. [b] calculated from a reference sample.*

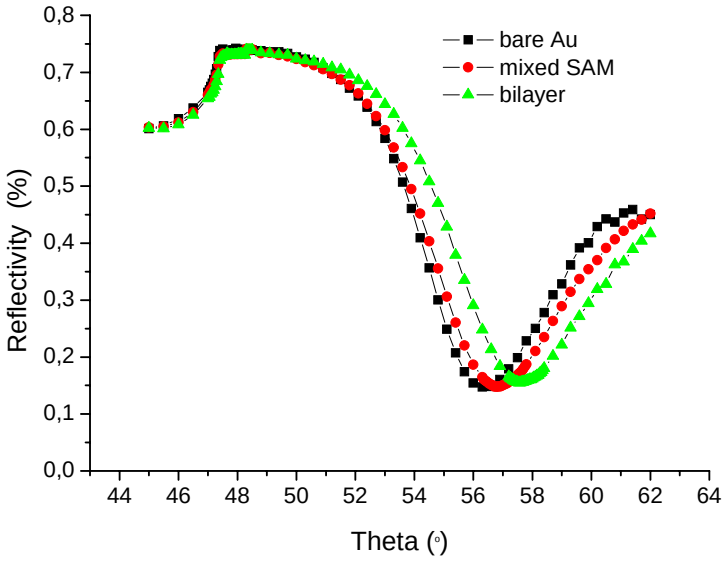

Figure 5.1: *Assembly of mixed tBLM on the gold surface. Angular scans of the reflected intensities for different interfacial architectures: the reference reflectivity curve (■) was measured for the TSG surface in contact with buffer solution. The self-assembled monolayer resulted in an angular shift of the reflectivity curve (●), and lipid bilayer obtained by vesicle fusion resulted in an additional angular shift (▲)*

The fusion of a mixture of liposomes to the mixed SAMs was followed by recording the reflectivity as a function of time at a fixed angle, θ = 56.5°. The recording was

transferred into a time-dependent increase of the thickness by calibration of the start- and endpoint (Figure 5.2). For small shifts in the resonance angle, the intensity in the quasi-linear range of the reflectivity scan can be assumed to be a linear function of the layer thickness.

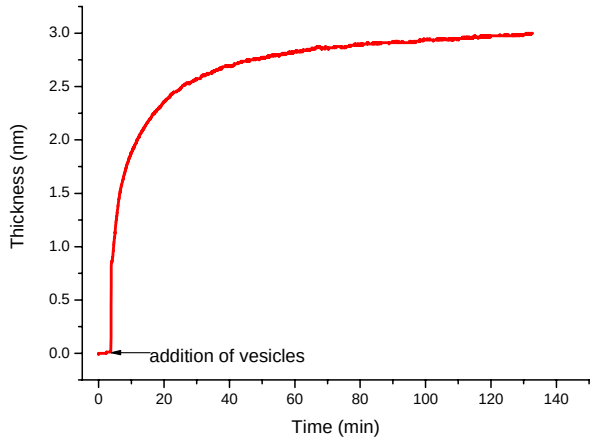

Figure 5.2: *The time resolved fusion of vesicles on mixed self-assembled monolayer measured by SPR. It shows the increase in thickness as a function of time during the fusion process of liposomes with a mixed self-assembled monolayer.*

The resulting SPR kinetic trace (Figure 5.2) displays clearly the adsorption of a 2nd adjacent layer on top of the self-assembled monolayer. The thickness of the 2nd layer is ~ 2.8 nm. It shows the increase in thickness as a function of time during the fusion process of liposomes with a mixed self-assembled monolayer, indicating the completion of the bilayer. Based on a fitting routine using the Fresnel equations, the thicknesses of each layer compared to those based on pure DPTL SAM are listed in Table 5.2.

	TSG	**Mixed SAM**		**Pure DPTL SAM**	
		before vesicle fusion	**after vesicle fusion**	**before vesicle fusion**	**after vesicle fusion**
Thickness increase Δd /(nm)	50	4.3	2.8	4.9	3.4

Table 5.2: *SPR data obtained by fitting to the Fresnel Equations of the mixed SAM on TSG before and after fusion of a mixture of liposomes*

5.1.2 Electrochemical impedance spectroscopy (EIS) measurements

Mixed SAMs before and after vesicle fusion were further investigated by electrochemical impedance spectroscopy (EIS). Figure 5.3 shows the admittance plot and Bode plot of the spectra before (black) and after (red) completion of the fusion process.

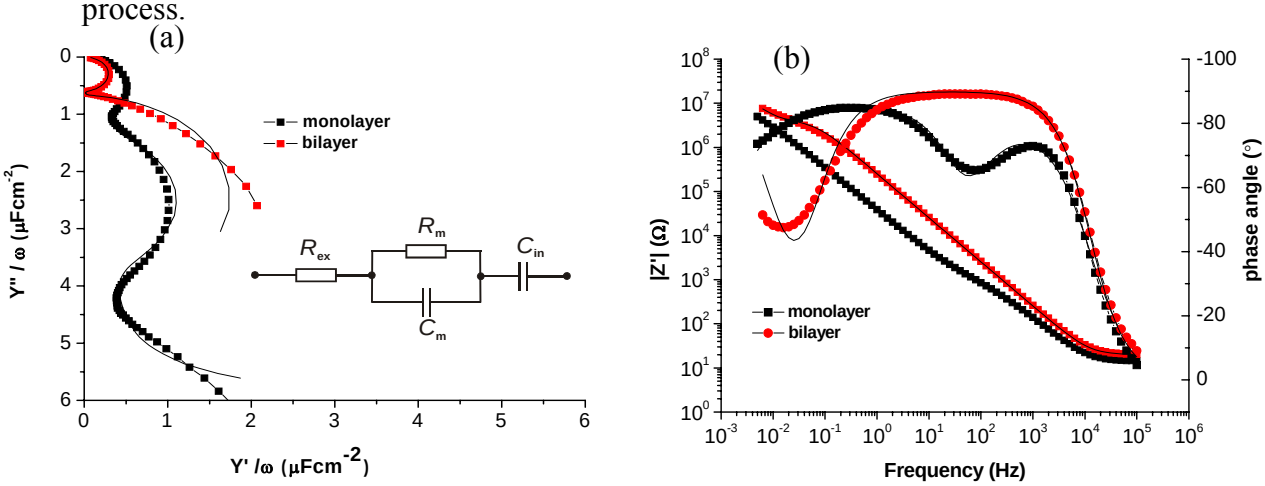

Figure 5.3: *EIS spectra of mixed SAM before and after vesicle fusion. The Admittance plot (a) and Bode plot (b) of monolayer (black) and bilayer (red) and equivalent circuit to fit the data.*

The capacitance and resistance of the mixed monolayers and bilayers obtained from EIS, were calculated by fitting the data to the equivalent circuit shown in the inset of Figure 5.3. The equivalent circuit consists of a resistance of electrolyte solution R_{ex} in series with a RC element (a resistance connected in parallel to a capacitance) representing the lipid bilayer membrane, the membrane resistance R_m and capacitance C_m respectively, in series with an internal reservoir capacitance C_{in}. The resulting fitted data are listed in Table 5.3.

	R_m (MΩcm^2)	C_m (μFcm^{-2})	C_{in} (μFcm^{-2})
Monolayer	0.7 ± 0.5	1.2 ± 0.05	4.3 ± 0.05
Bilayer	3.6 ± 1.1	0.8 ± 0.02	3.9 ± 0.03

Table 5.3: *EIS fitting parameter for the data in Figure 5.3*

The capacitance of the mixed monolayers obtained by fitting was 1.2 ± 0.05 μFcm^{-2}, while the resistances of the mixed monolayer vary in the range of several hundred KΩcm^2 to 1 MΩcm^2. During the vesicle fusion, the resistance increased to the range of MΩcm^2 and the capacitance decreased to 0.8 ± 0.02 μFcm^{-2} due to the increased thickness of the alkyl moiety of the lipid bilayer.

For comparison purposes, a tBLM was formed from a pure DPTL SAM after vesicle fusion. Impedance spectra (Figure 5.4) were fitted to the equivalent circuit described above.

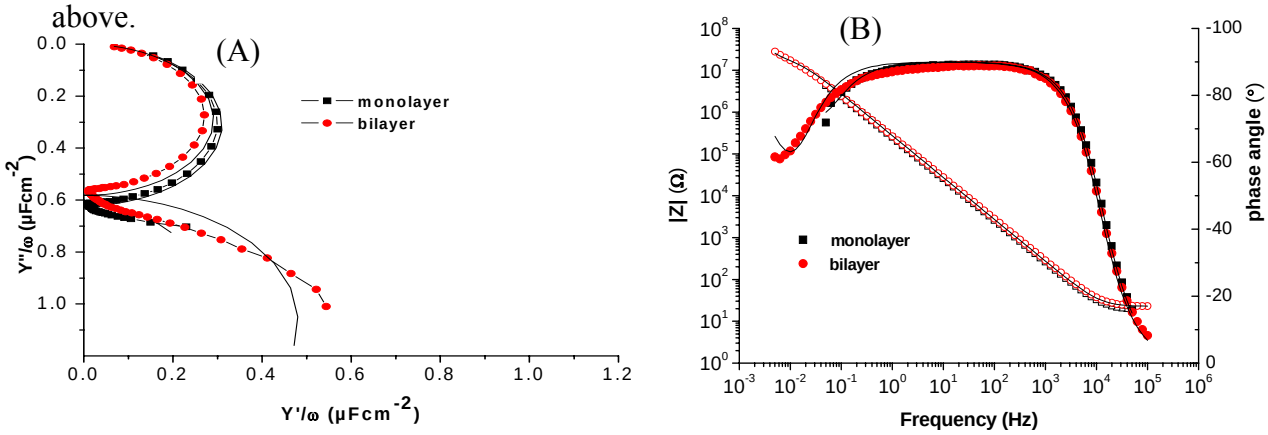

Figure 5.4: *EIS spectra of undiluted DPTL SAM before and after vesicle fusion. The Admittance plot (A) and Bode plot (B) of monolayer (black) and bilayer (red)*

The fitted data results are listed in Table 5.4.

	R_m (MΩcm^2)	C_m (μFcm^{-2})	C_{in} (μFcm^{-2})
Monolayer	2.4 ± 1.1	1.4 ± 0.02	3.6 ± 0.02
Bilayer	7.2 ± 1.5	0.7 ± 0.03	3.2 ± 0.03

Table 5.4: *EIS fitting parameter for the data in Figure 5.4*

Data obtained from undiluted DPTL show that the capacitance and resistance of the monolayer are 1.4 ± 0.02 μFcm^{-2} and 2.4 ± 1.1 MΩcm^2 respectively. The bilayer resistance increased to 7.2 ± 1.5 MΩcm^2 and the capacitance decreased to 0.7 ± 0.03 μFcm^{-2}.

5.1.3 Contact angle measurement

The contact angle of the mixed SAM in the present case (mixing ratio 10%) was $\theta = 95°$. More about contact angle measurements will be described in section 5.4.

5.1.4 Discussion

The optical thickness of the mixed monolayer thus obtained is 4.3 nm, lower than 4.9 nm reported earlier for an undiluted DPTL SAM. This suggests an inhomogeneous monolayer based on a mixed SAM. But as far the fusion of liposomes composed of DPhyPC, cholesterol and DPhyPG to the mixed self-assembled monolayers is concerned, the overall thickness of 7.1 nm thus obtained with a thickness increase $\Delta d = 2.8$nm (see Table 5.2) is quite reasonable compared to the calculated length of the molecules involved in the tethered bilayer formation. It is also comparable to the thickness of 8.3 nm for a bilayer obtained from an undiluted DPTL SAM after vesicle fusion.

The result shown by contact angle measurement indicates the hydrophobic interaction is still strong enough to provide the driving force for the formation of the bilayer. Such a surface was sufficiently hydrophobic to allow for a bilayer formation by fusion of liposomes.

The electrical properties investigated by EIS also confirm the formation of bilayers. Impedance spectra indicated the major differences on the level of SAMs based on pure DPTL and that with addition of TEGL, but only minor differences of the impedance spectra of the bilayers. The spectra of the mixed SAM display two time constants, while undiluted SAM have only one time constant. As soon as the bilayers are eventually formed, the spectra look quite the same either for the bilayers based on a mixed SAM or on an undiluted SAM. The capacitances of both SAM are above 1 μFcm^{-2}, and the decrease in membrane capacitance suggests the formation of the bilayers. The resistances of the mixed monolayer vary in the range of several hundred

$k\Omega cm^2$ to some $M\Omega cm^2$. The relative large range is thought to be due to a variable mixing ratio on the surface. But as the vesicle mixture fused to those mixed SAMs, the membrane resistance increased, as expected for the formation of a well sealed tethered lipid bilayer. The increase in bilayer resistances obtained from mixed SAMs implies that the gaps between the thiolipids and dilution molecules on the proximal bilayer leaflet have been filled by the free lipids, resulting in the formation of a highly insulated bilayer. It indicates that the free lipids from the liposomes have been successfully inserted into tBLMs. Therefore, tethered lipid bilayer membranes formed by addition of dilution molecules into the thiolipids in self-assembled monolayers with the purpose of increasing the fluidity of the bilayer can be achieved in the way described in the motivation section. It proves that the concept tBLMs based on mixed SAM really works on the way to obtain a good model system of the biological membrane.

5.2 Variation of the mixing ratio of the components in the mixed SAM

5.2.1 Electrical properties of mixed tBLMs determined by EIS

Once the concept of the mixed tBLM had been verified, the mixing ratio should be optimized. Therefore, the mixing ratios of DPTL and TEGL in the solution were varied from 90:10 to 65:35. In order to determine the electrical properties of tBLM, EIS were performed. Results are shown in the EIS spectra (Figure5.5) of monolayers and bilayers from the mixed SAMs with different mixing ratio.

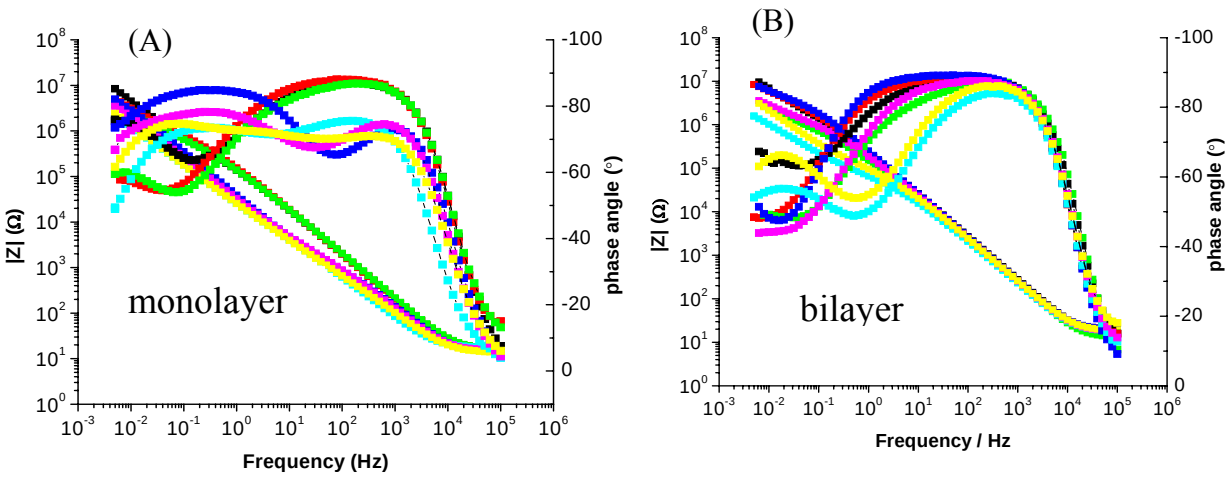

Figure 5.5: *Impedance spectra of mixed monolayers and bilayers for different mixing ratios*

For comparison purposes, capacitance and resistance of the mixed monolayers and bilayers obtained from EIS, were calculated by fitting the data to the equivalent circuit described above. The fitting results are plotted as a function of mixing ratio illustrated in Figure 5.6.

(A)

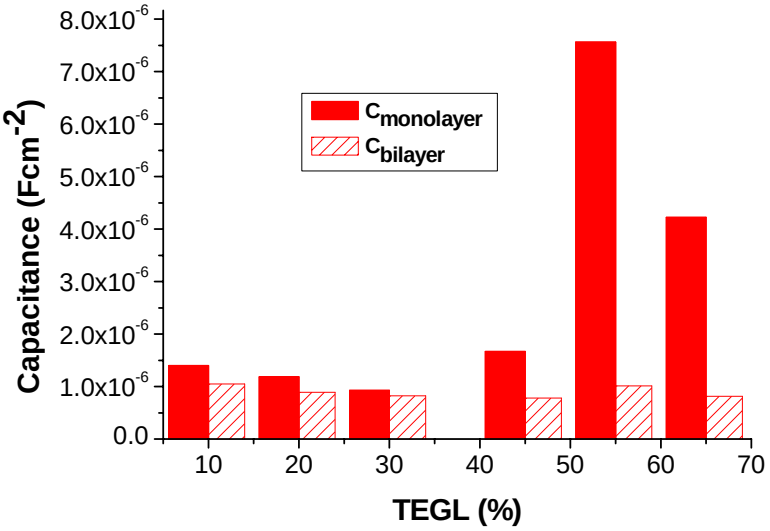

(B)

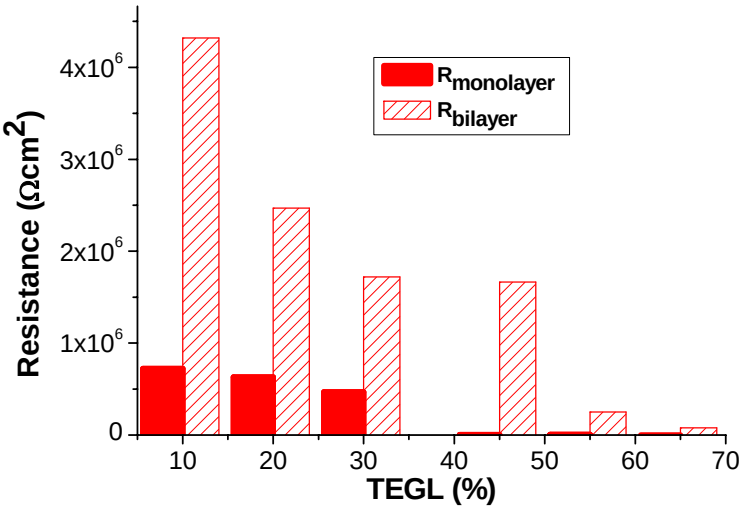

Figure 5.6: *Capacitances for mixed monolayers (A) and resistances) for bilayesr (B) as a function of percentage TEGL component in solutio*

For the monolayers, with the TEGL component in solution lower than 45%, the capacitances of mixed monolayers vary in the range from 1.1 to 1.6μFcm^{-2}, and the resistances are in the range of 700 to 900 kΩcm^2. With the TEGL component in solution higher than 45%, the capacitances vary from 2.3 to 6.5 μFcm^{-2}, while the resistance of the monolayer is as low as several hundred kΩcm^2.

Bilayers are formed in all cases as indicated by the decrease in membrane capacitance, which finally reaches the values also formed by pure tBLMs. The average bilayer capacitance, determined from at least 5 different samples, is about 0.6 ± 0.25 μFcm^{-2} for all mixing ratios.The resistances of the bilayers have noticeably larger values of 3.5 ±1 $M\Omega cm^2$ with the TEGL component in solution lower than 45%, while they reached only the range of about some hundred $k\Omega cm^2$ with the TEGL component in solution higher than 45%.

5.2.2 Discussion

For the TEGL component in solution lower than 45%, the DPTL component dominates in the solution of mixed SAMs, implying that more DPTL molecules than TEGL molecules were attached to the gold surface. When the TEGL component in solution is higher than 45%, the mixed SAMs have been more diluted, resulting in higher membrane capacitances. Similar information could be obtained from changes in membrane resistance. Resistances of the monolayers were even lower than those at TEGL lower than 45%. This suggests that the SAMs had been spatially diluted on the surface due to the large amount of TEGL molecules added.

By fusion of a mixture of liposomes to the mixed SAMs, the bilayers have been formed, which is indicated by the decrease in membrane capacitance. The values obtained from bilayer capacitance correspond to the values formed for pure tBLMs. But the resistance of the bilayers indicated the electrical sealing properties of these tBLMs. At TEGL component in solution lower than 45%, the bilayer resistances have noticeably larger values, indicating the highly insulated bilayer membranes. It suggests that formation of mixed tBLMs with good sealing properties can be achieved at TEGL component in solution lower than 45%. Such tBLMs can fulfill the requirement as model system to mimic the biological membranes. As the TEGL component in solution is higher than 45%, the mixed tBLMs are still formed but with some defects. These defects could be due to the fact, that the gaps between the DPTL molecules are no longer filled with free lipids. Moreover, the ratio on the surface

might change during the incubation of SAMs and might not correspond to ratio in the solution. Such defects may lead to the bilayers formed with insufficient electrical sealing properties, needed for the further study of ion transfer.

The measurements described so far, would suggest that the optimal mixing ratio of TEGL/DPTL in solution would be 45:55. However, in the course of the investigation, the purity and stability of the TEGL sample turned out to be ill defined. The TEGL molecule has a tendency to polymerize and /or to form degradation products. This was found out later by NMR and MS measurements of the samples of TEGL, stored for several months at -25°C.

5.3 Determination of composition of the mixed SAMs by reductive desorption

In order to quantify the amount of thiolipds and dilute molecules on the surface, reductive desorption of SAMs from pure DPTL, TEGL and mixed SAM from DPTL with TEGL were performed.

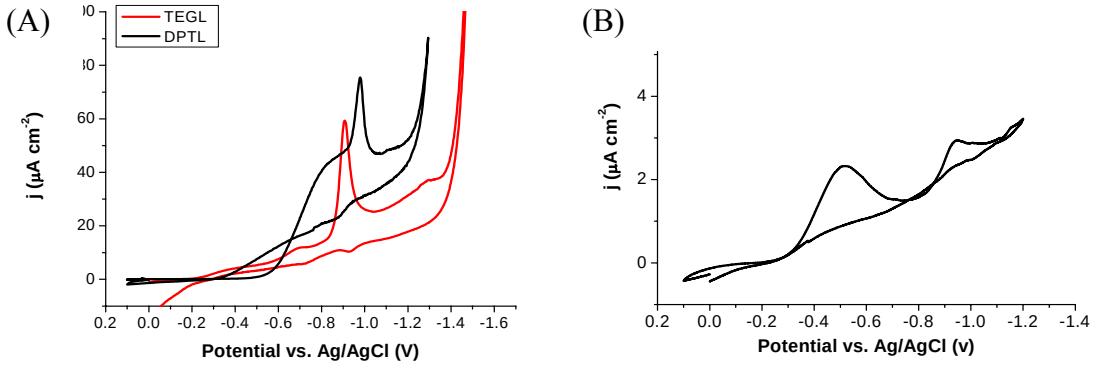

Figure 5.7: *Reductive desorption measurements of SAM prepared from pure DPTL (A black), pure TEGL (A red) and mixed SAM (B)*

Figure 5.7 shows the reductive desorption peaks of SAM prepared from pure DPTL (Figure 2A black), and pure TEGL (Figure 5.7 A red). Analysis of the area of desorption peak of the DPTL SAM resulted in an area of 43 $Å^2$ per molecule, assuming both sulphur groups of the lipoic acid moiety bind to the gold surface. The desorption peak of the TEGL SAM gave an area of 12 $Å^2$ per molecule.

Reductive desorption of mixed SAMs prepared from a mixture of DPTL and TEGL on gold surface (Figure 5.7 B) was shown to give rise to double peaks. However, the peak separation was insufficient to determine the relative proportion of thiols assembled on the surface. Therefore, another attempt has been made to determine the ratio of components in the mixed SAMs.

5.4 Determination of composition of the mixed SAMs by contact angle

By measuring the water contact angle of the mixed monolayer, the mixing ratio can be calculated according to an investigation carried out on monolayers of cholesterol functionalized thiol derivatives mixed with mercaptoethanol[40]. These authors showed a linear dependency between the percentage of cholesterol lipid and the cosine of the contact angle according to Cassie's law

$$\cos\theta = f_1 \cos\theta_1 + f_2 \cos\theta_2 \qquad \text{Equ. 20}$$

where θ, θ_1 and θ_2 are the advancing contact angles on the mixed surface and the two single component surfaces, respectively, and f_1 and f_2 are the fractions of each component present in the mixed monolayer[128].The contact angles of the mixed monolayer are listed in Table 5.5, compared to θ =109° of a pure DPTL monolayer[111], and θ = 25° of a pure TEGL monolayer. The mixing ratio on the surface calculated from these values was shown in Table 5.5.

As illustrated in Table 5.5, the water contact angle of these mixed SAMs with different mixing ratio varies in the range of 76° to 95°. The values of contact angle obtained are smaller than the 109° of a pure DPTL monolayer, but significantly larger than the 25° of a TEGL monolayer. The mixing ratios calculated from the measured values of water contact angles indicate the big variation of the mixing ratio of the components of DPTL and TEGL on the surface. 3% TEGL in the solution led to 20% TEGL molecules adsorbed on the surface. The mixing ratios obtained from contact angle measurements show that more TEGL molecules accumulate on the surface, as compared to their amount in the mixed solution. This indicates that small TEGL molecules adsorb faster than DPTL molecules on the surface. As mixing ratios in the solution were smaller than 10%, the surface was still relatively hydrophobic (θ > 80°). But at TEGL higher than 10%, the surface tended to hydrophilic (θ < 80°). The calculated mixing ratio on the surface shows more TEGL molecules adsorbed on the surface than those in the solution. However, the formation of bilayers was obtained only with mixing ratio in solution of

TEGL/ DPTL ≤ 10/90, corresponding to the ratio of TEGL/DPTL ≤ 40/60 on the surface. This result indicates that the hydrophobic force of the DPTL molecules on the surface is the dominating driving force of vesicle fusion. Such results correspond to those obtained from SPR and EIS data, considering that the bilayer would be on a TEGL mixed SAM with the TEGL component in solution lower than 45%, when the TEGL was freshly prepared.

Mixing ratio of DPTL/TEGL in the solution (molar ratio)	**Contact angle (°)**	**Calculated mixing ratio of DPTL/TEGL on the surface (molar ratio)**
100% DPTL	109	
100% TEGL	25	
97 : 3	95	80 : 20
95 : 5	92	76 : 24
93 : 7	85	67 : 33
90 : 10	81	60 : 40
85 : 15	76	54 : 46

Table 5.5: *Ratio of components self-assembled monolayer (SAMs) of thiolipid /spacer molecule mixture obtained by contact angle.*

From these values obtained by contact angle measurements, the amount of DPTL and TEGL molecules on the surface can be estimated. Mixing ratio on the surface gained from contact angle measurements can also prove that small TEGL molecules are easier and faster than DPTL molecules to chemisorb to the gold surface. The range of mixing ratio listed in Table 5.5 could be used as a reference for us to prepare the mixed self-assembled monolayers.

5.5 Bilayer formation monitored by the quartz crystal microbalance

More information about the unrolling and spreading of vesicles to form a bilayer can be obtained by measurements with the QCM. The discrimination between an adsorption and the fusion of vesicles has been reported by Keller and Kasemo[129] by monitoring the changes in both of frequency and dissipation. The change in frequency is proportional to the change in mass when the absorbed layer is rigid or homogenous. However, most of polymers, especially proteins are visoelastic. The detail from dissipation change can tell us the change in visoelastic and rheological properties of the adsorbed materials.

To further investigate the fusion of vesicles onto the self-assembled monolayers prepared from the mixture of DPTL and TEGL, QCM technique was applied to detect the property of the SAMs. As a control experiment, vesicle fusion on pure DPTL SAM was also performed.

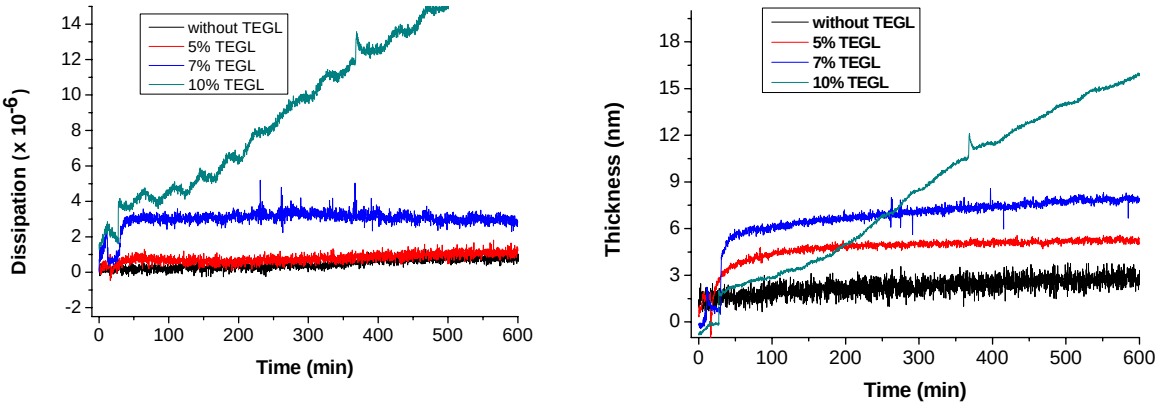

Figure 5.8: *(A) depicts the dissipation as a function of time (B) Thickness as a function of time resulting from vesicle mixture fusion onto pure DPTL monolayer (black line), 5% TEGL mixed SAM (red line), 7% TEGL mixed monolayer (blue line) and 10% TEGL mixed monolayer (navy blue line).*

Fusion of vesicle onto DPTL SAM and the mixed monolayers with different mixing ratios are shown in Figure 5.8. The results obtained from QCM are listed in Table 5.6.

Composition of mixed SAMs	Δf (Hz)	ΔD (x 10^{-6})	Thickness (nm)
100% DPTL	23	0.6	2
5% TEGL	27	1.0	3
7% TEGL	35	2.6	5.5
> 10% TEGL	45	15	10

Table 5.6: *Frequency shifts, dissipation changes and thicknesses of the second layers after vesicle fusion*

The adsorption of vesicles onto a SAM of pure DPTL displays a large shift in the resonance frequency (23 Hz) and minor shift in the dissipation (0.6 x 10^{-6}). The frequency shift corresponds to a thickness increase of 2 nm, indicating the formation of a second lipid leaflet on top of the proximal lipid monolayer. The low final dissipation is a good indicator for the quality of the bilayer[130]. The dissipation shift of the thin film is in excellent agreement with literature data for the formation of a freely floating bilayer on silica by Keller *et al*[131]

Once the adsorption of vesicles onto a SAM of 5% dilute molecule (TEGL) containing in the thiolipid solution is complete, the total frequency shift is 27 Hz and dissipation shifts about 1.0 x 10^{-6}, still in the range for a completion of vesicle fusion, forming a second lipid monolayer. The thickness obtained from frequency shift is approximately 3 nm. It indicates at a 5% dilution with TEGL, fusion of vesicles is taking place with no further adsorption of vesicles.

The SAM was further diluted with addition of 7% TEGL. The final frequency shift of 35 Hz corresponds to a film thickness of around 5.5 nm which is higher than as expected for second leaflet of lipid, indicating that the adsorption of liposomes had taken place. Also the dissipation is slightly higher than those observed for the formation of second lipid monolayer onto pure thiolipid SAM and SAM of 5% TEGL

mixed thiolipid solution. But somehow the formation of a bilayer with thickness of 5.5 nm still indicated, suggesting that some additional vesicle adsorption could have happened at the late stage of the vesicle fusion.

Having the TEGL mixing ratio higher than 10%, the QCM measurement shows preferable adsorption of vesicles on the surface instead of vesicle fusion, which kept increasing both in dissipation and in thickness of the lipid film. It implies that the swelling of the film has happned. Furthermore, it could be that more TEGL molecules adsorbed on the surfaces, which could result in the earlier sweeling of the film in the buffer solution, because the results obtained from contact angle measurements indicated that TEGL molecules adsorbed faster than DPTL molecules on the gold surface. This may further influence the process of vesicle fusion, leading to direct adsorption of vesicles onto the quartz crystal surface instead of fusion. Adsorption of vesicles could be accelerated by an increased swelling of the film due to the dilution with TEGL molecules.

The QCM measurements provide further proof for the possibility to form tBLMs either from pure DPTL SAM or from mixed SAMs, however at mixing ratios lower than 10% (this value may vary from one batch TEGL to the other because of impurities in the sample). The results obtained by QCM measurements indicated that fusion of liposomes onto more hydrophobic surface led to earlier saturation, avoiding the additional adsorption of the vesicles. Using QCM technique in the investigation of lipid bilayer formation give further information about the quality of the bilayers eventually formed. It can be used as tool to examine the kinetics of vesicle fusion. Therefore, the mixing ratio used for the preparation of mixed SAMs to form a tBLM for ion transport studies is DPTL/TEGL = 90:10.

5.6 Characterization of the SAMs by AFM

The quality of the self-assembled monolayers and the formation of bilayers were characterized by atomic force spectroscopy technique.

5.6.1 Imaging of TSG, SAM and mixed SAM

The mixed monolayers are not expected to show significant aggregation because of the relatively low van der Waals interactions present between the bulky phytanoyl chains. Mixed monolayers were first investigated by AFM in an attempt to prove the absence of lateral segregation of the two molecules. Figure 5.9 shows the comparison of an unmodified TSG surface (Fig.5.9A) and a TSG surface modified with a mixed monolayer of DPTL/TEGL (Fig. 5.9B) measured in air.

Figure 5.9A show a typical template stripped gold (TSG) surface with some slight inhomogeneity of the Au grain structure across the 1 μm^2 surface area of this analysis. The root mean square (RMS) roughness for this surface is 0.29 nm with a maximum peak-to-valley height of <2 nm. If a mixed monolayer is adsorbed on the surface, the RMS roughness increases to 0.5 nm with a similar peak-to-valley roughness. The components of the mixed SAM, DPTL and TEGL seem to be evenly distributed giving rise to very smooth surfaces with no significant increase of the roughness with respect to pure TSG[111,128]. However, the AFM procedure more appropriate to detect phase separation is lateral force microscopy. The result is shown in Fig.5.9c also giving no indication of an appreciable segregation.

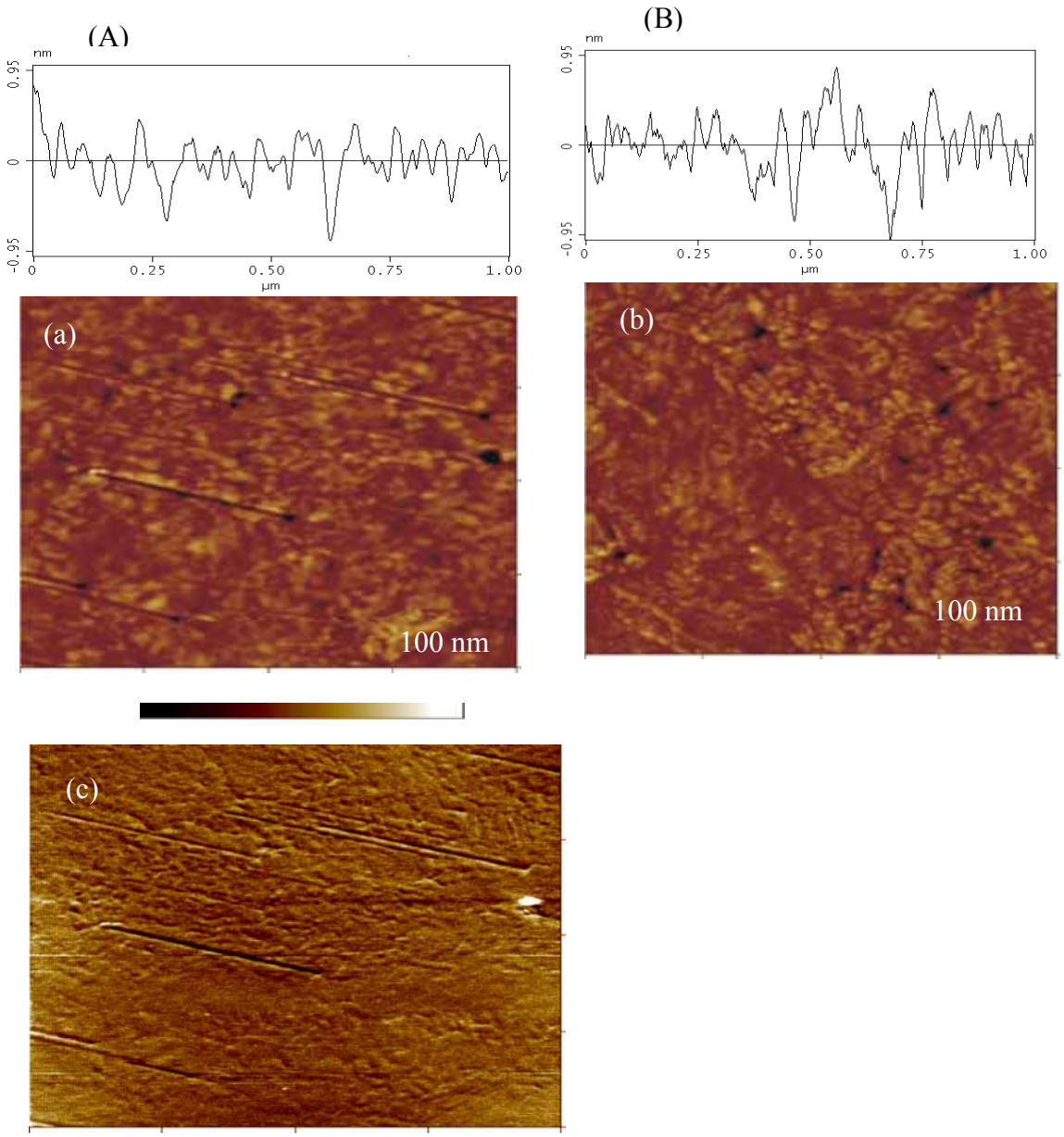

Figure 5.9: *Contact mode AFM images of template stripped gold (TSG) before (a) and after (b) formation of the mixed SAM of DPTL/TEGL. The surface cross section profiles of each sample is given at the top of (A) and (B).Curve (c) represents the friction mode AFM image of the mixed SAM.*

5.6.2 Morphological change during the formation of bilayer

Figure 5.10 shows the AFM images of a mixed SAM before and after incubation with vesicles. Figure 5.10 A shows a very flat surface for the mixed monolayer, and the

surface roughness is approximately 0.5 nm. The image of bilayer also indicates a flat surface with the surface roughness of 0.2 nm. The surface roughness decreases from 0.5 nm for a mixed monolayer to 0.2 nm for a bilayer, suggesting that the bilayer smoothes out the actual surface roughness. No clear difference can be detected by the AFM image scan compared with the image of mixed monolayer as expected, because DPhyPC is fluid at all temperatures, so that the bilayer formed eventually is flexible and soft and hard to detect by a simple AFM image scan, indicated only as dragging traces shown in Fig.5.10B.

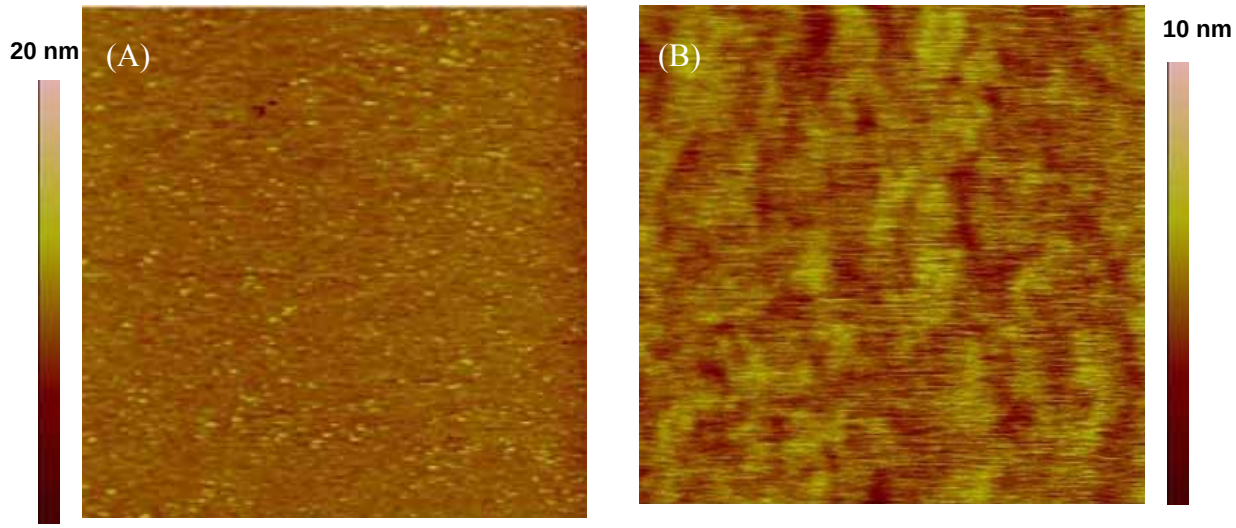

Figure 5.10: *Tapping mode of AFM height images of mixed self-assembled monolayer in buffer before (A) and after (B) addition of vesicles. The image size of (A) is 2 x 2 µm^2 and (B) is 1 x1 µm^2.*

After 60 min. of vesicle fusion, the surface was again observed by AFM. Vesicle absorption on top of the previously formed bilayer could be detected, displayed as white spots located on the surface. The AFM image scans of vesicle adsorption are shown in the Figure 5.11. It indicates that within 60 min. after vesicles were added to cell, the vesicle fusion was completed, and after that the vesicle adsorption would take over. These additionally adsorbed vesicles could be removed by rinsing 15 min. with buffer solution.

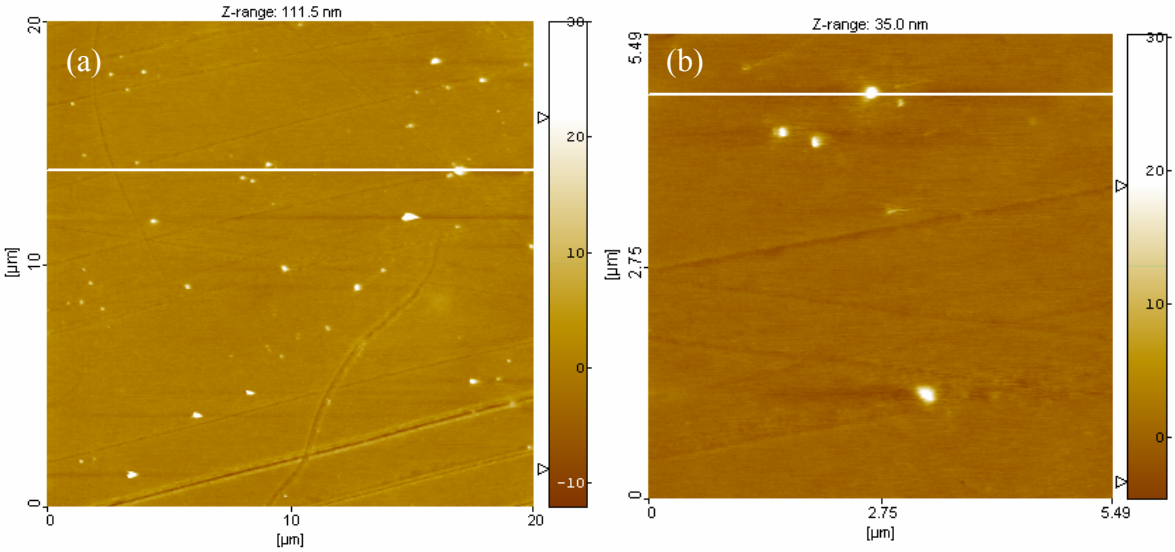

Figure 5.11: *Tapping model of AFM images of vesicle adsorption onto mixed self-assembled monolayer before rinsing. (a) The image size is 20 x 20 µm^2 and amplitude image with z-scale = 111.5 nm. (b) Deflection image size is 5.5 x 5.5µm^2 and amplitude image with z-scale = 35 nm*

5.6.3 Force measurements on the bilayers

Besides imaging, force measurements can be done to obtain additional information. In order to investigate whether a supported bilayer was present, we performed a series of force measurements (Figure 5.12). Before and after incubation with vesicles, two distinct types of force curves were observed (Figure 5.12b –d). Panels c and d of Figure 5.12 are typical force curves taken on a tBLM.

When measuring force curves on surface layers a jump of the tip is often observed once a certain threshold force has been exceeded. In this work we focus on jumps that are observed on bilayers made by spreading liposomes on mixed SAMs. Panel a and b of Figure 5.12 are recorded before vesicle fusion and after short time of addition of vesicles. Panel c and d of Figure 5.12 are typical force curves on the bilayer.

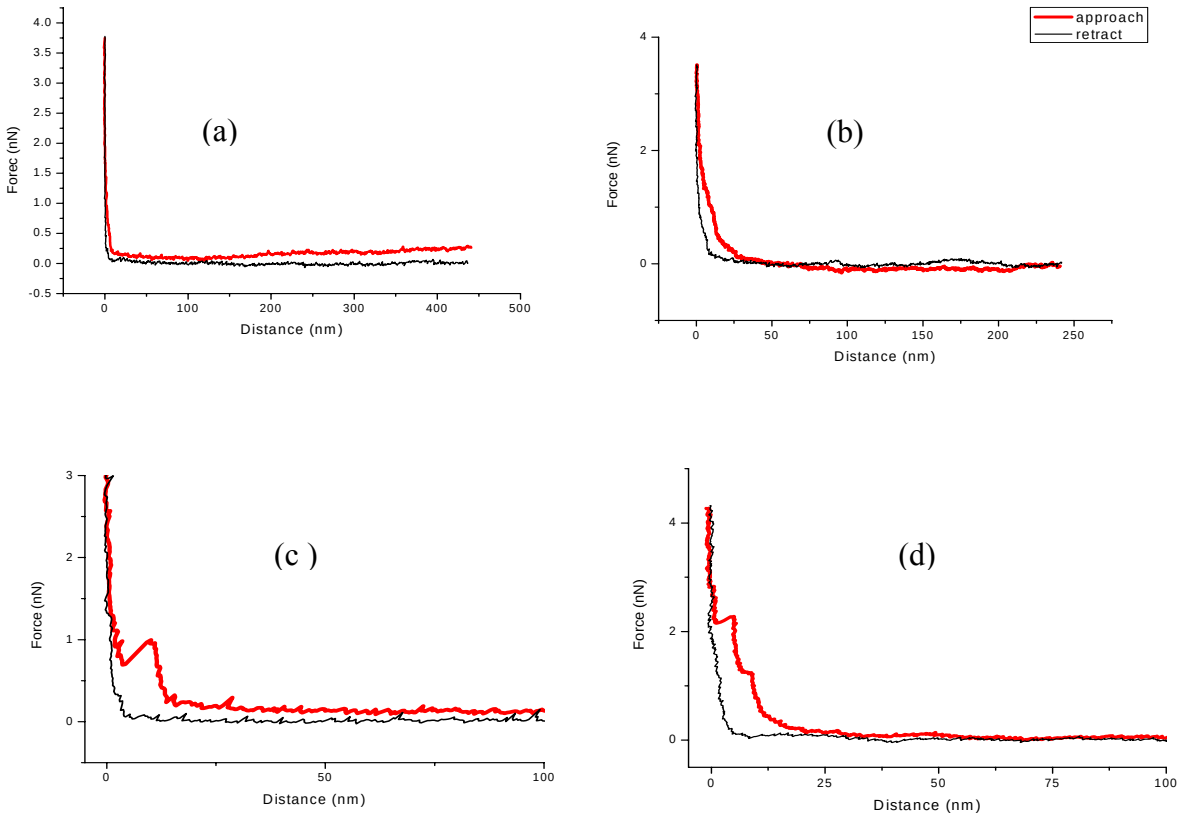

Figure 5.12: *(a-d) Force curve measurements of TSG modified with DPTL/TEGL (90:10) in molar ratio before (a) and after (b-d) incubation with mixed membrane vesicles. Three types of force curves were observed: (b) no jump at all, (c) one jump, and (d) two jumps*

As illustrated in Figure 5.12, no force is acting on the tip far away from the surface. Decreasing the distance between the tip and sample, the force increases. After the exponential regime a rather linear part follows that displays mechanical deformation in combination with hydration and steric forces[132]. Finally an abrupt break-through appears. Force curves of areas without vesicle spreading never showed the typical force signal obtained when piercing a bilayer, confirming that no bilayer formed underneath the vesicles (Figure 5.12b).

The presence of a bilayer after vesicle fusion was verified by taking force curves at different points on the surfaces. In the presence of a bilayer, a characteristic instability and a jump of ~3 nm have been observed after applying a certain load of typically 2-10 nN.

Figure 5.13 represents more detail about a typical force curve captured on bilayers. Force increased from zero to ~ 1nN (F_{fusion}) before a "jump" was observed. The jump is due to the sudden movement of the AFM tip toward the substrate. Then it was followed by the second "jump" at ~ 2nN. This instability was interpreted as the formation of a hole in the solid-supported bilayer and penetration of the tip[133-136]. These holes in the bilayer formed reversibly. When the tip retracted, the bilayer filled the holes again and a subsequent force curve looked identical to that obtained before bilayer penetration.

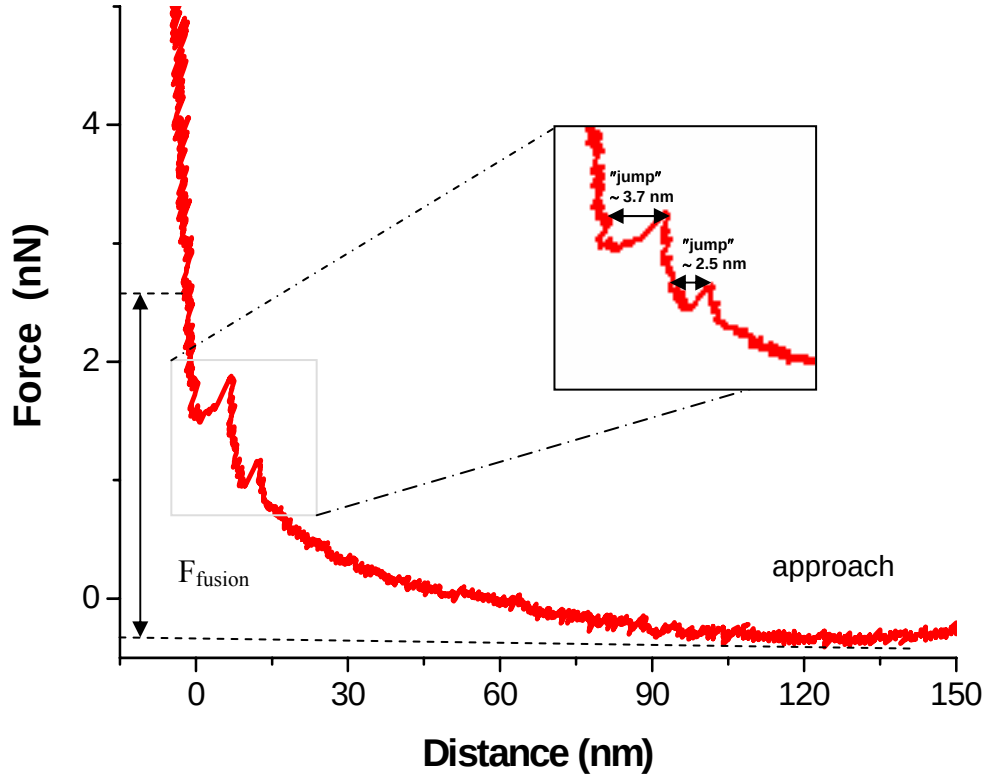

Figure 5.13: *AFM force scan during approach showing the increase in force as the lipid bilayers are compressed against one another. The sudden movement of the tip causes the jumps. The jump distance (inset) is on the order of a lipid bilayer thickness.*

Within one experiment, break-through forces were relatively constant and only varied slightly from force curve to force curve. Although the exact locations of the breaks

varied somewhat, the gap distance between the beginning and the end point of the jump-in was at the range of 3.5 to 4.3 nm. This unique gap distance corresponds to the thickness of lipid bilayer. We assumed that during the approach of the tip to the sample, the outlet position at the top of the bilayer gives way to the pressing tip and slides aside, followed by continuous compression of the tip on the bilayer, until the tip approaches and breaks through the bilayer. The jump distance (inset) is on the order of a lipid bilayer thickness and in interpreted as the result of the coalescence of the two approach bilayer into one, meaning that vesicle fusion process has taken place.

Measurements performed on tBLM either from pure DPTL SAM or mixed SAM hasve shown a similar phenomenon, with two breakthroughs being observed. A first break-through at approximately 1 nN is followed by a second one at 2 nN. The height of the first one corresponds to a monolayer with the values approximately 2.5-3 nm while after the second break-through the tip penetrates 3.2- 4 nm deeper. The situation of two break-through occurred without any apparent change of the experimental parameters. The stepwise deformation during the approach is illustrated schematically in Figure 5.14 as a (a) compression of upper layer, (b) break-through of tip portion, (c) further compression of bilayer with tip bridging the top potion, and (d) further break-through of bottom portion and going into spacer region.

The studies done by other groups reported that occasionally multiple break-through events were observed[137-138]. The authors found that the break-through distances do not agree with the thickness of one lipid bilayer. Müller *et al*.[139] report on the occurrence of a jump in distance of 7-8 nm corresponding to a penetration of both layers in one jump, respectively. They explained that it is conceivable that only a comparatively big tip radius allows for the formation of a second lipid layer on the tip and this lipid layer might be a monolayer or a bilayer with tilted lipid molecules. In our case, we have thiolipids tethered on gold substrate with a thickness of 4.5 nm and after vesicle fusion the second lipid leaflet with a thickness of 3.7nm is formed on top of the monolayer. The total thickness of a tBLM is about 8 nm.

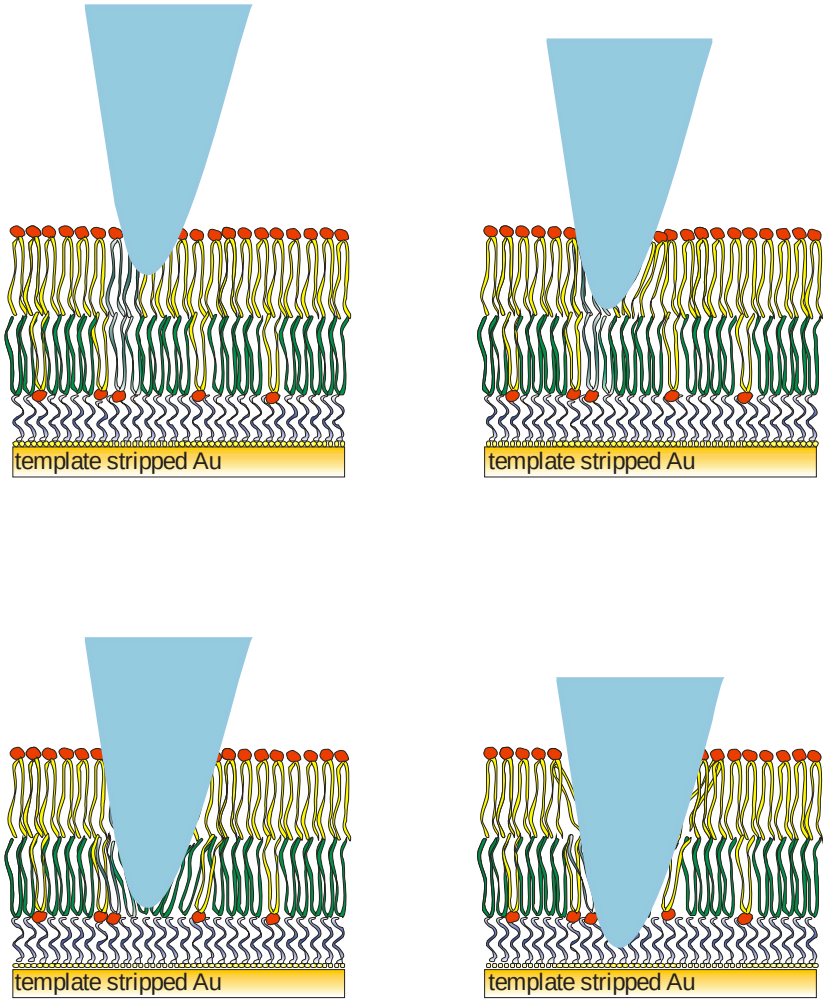

Figure 5.14: *Scheme of the tip effect on bilayer during approach force measurement.(A) Elastic compression of the vesicle top fraction. (B) Tip penetration of the upper bilayer. (C) Further compression with tip breaking the gap. (D) Tip penetration of the lower bilayer and further bridging the spacer region.*

We assume that the first break-through occurred when the tip penetrated into the outer leaflet of the bilayer formed by vesicle fusion to mixed SAM on the gold surface. The second break-through happened due to the further penetration of tip through the bilayer to the spacer part. A clear explanation or knowledge about these events needs more investigations. The total break-through distance we observed in this study on tBLM fit well to a single bilayer which is tethered on Au substrate. Such observations are comparable to the results obtained from solid supported BLMs on mica showing the

thickness of a bilayer to be in the range of 6 nm. The average values obtained from our studies done by the force curve measurements are summarized in Figure 5.15.

The information we got from Figure 5.15 tells us the thickness of the monolayer is approximately 4.5 nm, the second lipid leaflet is about 3.5 nm and the thickness of a tBLM is in the range of 8 nm. Force measurements thus appear to be a good indicator for the quality of tBLM. These results correspond to the thickness of DPTL SAM and bilayer eventually formed as determined by SPR.

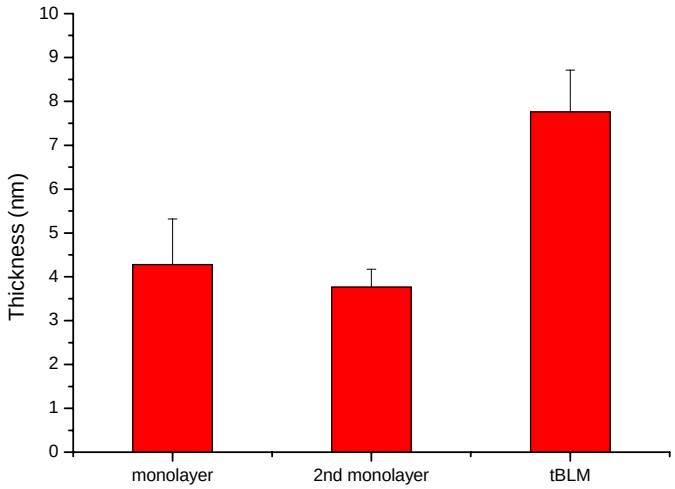

Figure 5.15: *Calculated thickness obtained by AFM force measurement as a function of the layer formation*

5.6.4 Conclusion

The results obtained using the atomic force microscopy demonstrate that this novel approach offers the temporal and spatial resolution and sensitivity to detect formation of bilayers. No difference could be seen from the undiluted tBLMs and mixed tBLMs. It could be shown that indentation of tBLMs results in large adhesion only if mechanical failure of the membrane occurs upon penetrating the membrane. The penetration of an AFM tip through a lipid bilayer tethered on Au substrate in aqueous

solution can be detected in the jumps by force-vs-distance curve. The force curves showed the gaps with a fixed gap distance equal to the lipid bilayer thickness. These gaps are interpreted as an abrupt jump of the AFM tip across the top or bottom portion of the bilayer tethered onto the gold substrate. But the exact explanation of these gaps needs further mechanical analysis. It proves that formation of bilayer by fusion of liposomes onto mixed self-assembled monolayer tethered onto gold substrate is achieved. The bilayer formed by fusion of vesicle onto pure DPTL monolayer has also been detected by AFM technique; it does not show any difference between the bilayers basis of either pure DPTL or mixed DPTL / TEGL monolayers. The AFM method offers new insights into adsorption, spreading, fusion, self-healing and mechanical properties of liposomes at the nanoscale.

5.7 Incorporation of Melittin in mixed tBLMs

Protein-lipid interactions play a crucial role in the formation of the stable structure of the biomembrane and in functioning of proteins in a two-dimensional lipid matrix[140-141]. So far, there is no full understanding of how proteins interact with the lipid membrane. Biophysical studies of protein-lipid interactions are usually performed on a model system composed of charged or uncharged α-helical peptides of different hydrophobic lengths and of lipid bilayer containing phospholipids of different head groups and of different length of hydrocarbon chains. These peptides can span the lipid bilayers and thus model the behaviour of integral proteins.

Supported lipid membrane provides the possibility to study the functional membrane proteins in quasi-natural environment, especially for the investigation of ion transport due to their exceptional mechanical functional stability. The system presented in this work offers in this context one of most promising approaches.

In the present study, the action of melittin on tBLMs was investigated, focusing on its capability to form channel forming defects, its lytic behaviour and propensity to change the morphology of the membrane. Electrochemical impedance analysis of tBLM on gold substrates was used to observe and quantify the formation of defects induced by melittin. SPR was done to monitor the kinetic formation of the bilayer incorporated with melittin.

5.7.1 SPR measurements

All SPR spectra were simulated using Fresnel equations. From the Fresnel's equation, the optical thickness of the coating can be calculated by assuming a refractive index of n = 1.45 for thiolipid, and a refractive index of n = 1.5 for lipids. Fusion of liposomes with the mixed SAMs (mixing ratio DPTL/TEGL = 90:10) was followed

by recording the reflectivity as a function of time for a fixed angle, θ = 56.5°. The recording was transferred into a time-dependent increase of the thickness by calibration of the start- and endpoint. For small shifts in the resonance angle, the intensity in the quasi-linear range of the reflectivity scan can be assumed to be a linear function of the layer thickness (Figure 5.16).

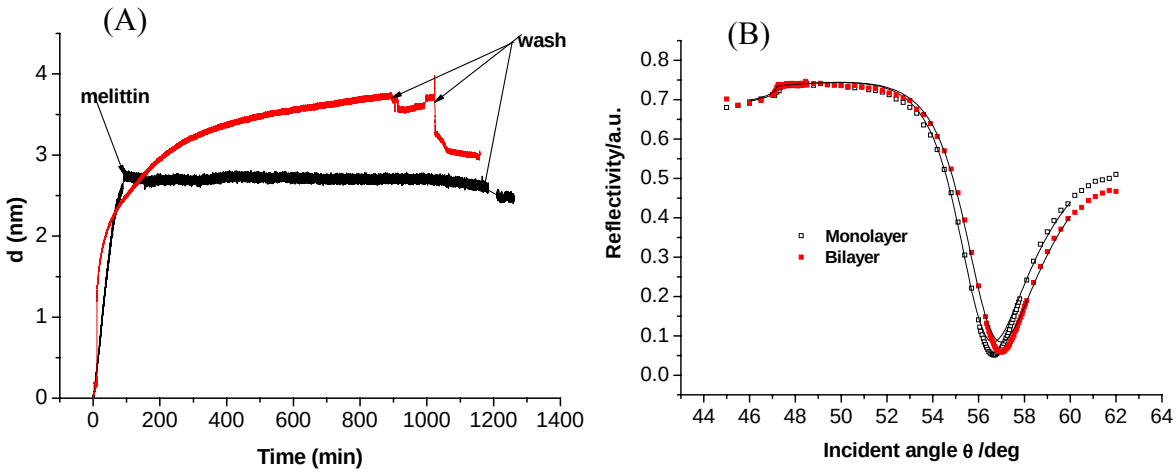

Figure 5.16: *(A) Kinetic measurement of vesicle fusion processes with (red) and without (black) addition of melittin .(B) represents the reflectivity scan of monolayer (■) and bilayer with melittin (●) by SPR.*

5.7.2 EIS measurements

The monolayer and bilayer formed after vesicle fusion were investigated by electrochemical impedance spectroscopy (EIS). Figure 5.17 shows the Bode plots of the spectra before and after vesicle fusion with and without melittin added. Impedance spectra were fitted to the equivalent circuit shown in the inset of Figure 5.17, which consists of a solution resistance R_{ex} in series with the membrane resistance and capacitance, R_m and C_m, respectively, in series with an internal reservoir capacitance C_{in}.

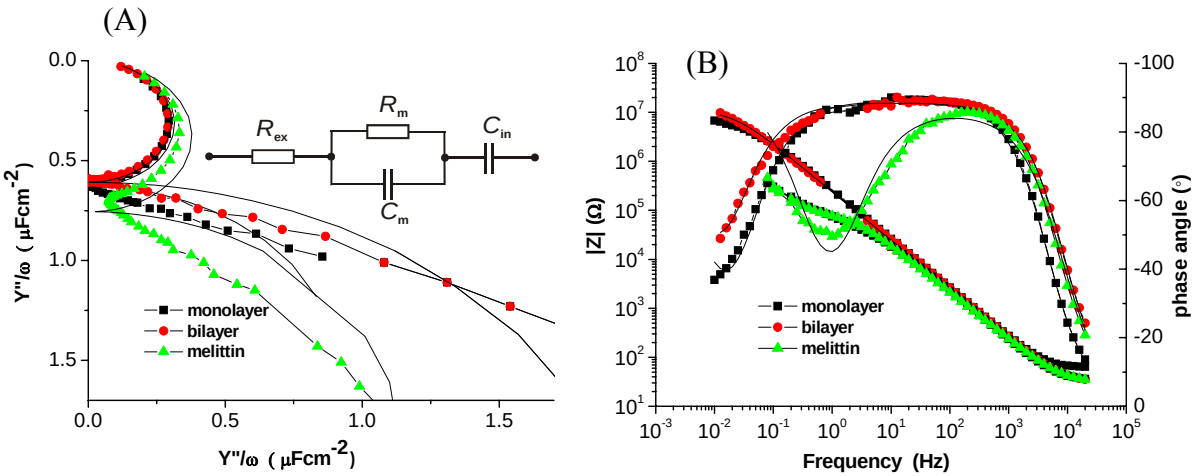

Figure 5.17: *Electrochemical impedance spectra of the mixed SAM before (■) and after (●) fusion with liposomes and with (▲) the incorporation of melittin into the tBLM.*

Surface	R_m/MΩ cm^2	A_{CPE}/(F cm^{-2})$^{\alpha}$	α	C_{in}/μF cm^{-2}
SAM	5.1	0.88	0.98	3.2
Lipid bilayer	7.4	0.73	0.99	5.0
Lipid bilayer with melittin	0.062	1.1	0.95	4.8

Table5.7: *EIS fitting parameters for the Data in Figure 5.17. A_{CPE} is the fit parameter for the CPE obtained from the ZVIEW fit routine, α represents the distribution parameter of time constants, for α=1, the CPE becomes a pure capacitor.*

The impedance spectra data by fitting to the equivalent circuit is listed in Table 5.7. Capacitance and resistance of the monolayer was in the range of 0.8 – 1.2 μFcm^{-2} and 1 to 2 MΩcm^2, respectively, in accordance with the high proportion of thiolipid. A constant phase element (CPE) was introduced into the equivalent circuit in place of C_m to account for heterogeneity of the mixed layers. During fusion, the resistance increased from 5 to 10 MΩ cm^2 and the capacitance decreased from 0.88 to 0.73 μF

cm^{-2} due to the increased thickness of the alkyl moiety from the lipid bilayer. If an ethanolic solution of melittin was added towards the final stage of vesicle fusion, the resistance decreased from 7.4 MΩ cm^2 to 0.06 MΩ cm^2 indicating ionic conductivity through the melittin channel. Throughout the experiment the inner membrane capacitance remained relatively unchanged.

5.7.3 AC voltammetry

Although EIS results show a clear transport of K^+ ions across the membrane, more detailed information can be extracted from the membrane/protein superstructure by monitoring the conductivity as a function of applied potential as measured by the in-phase component, Y′ of the electrode admittance at 10 Hz. In this case a potential sweep of ~10 mV/s was used with a 10 mV AC perturbation between 0.2 V to –0.7 V. The results are shown in Figure 5.18.

Initially, the conductivity of a tBLM prepared without any channel-forming protein was examined. A steady increase in the conductivity from 0.2 V to ~-0.6 V was observed which indicates a slight decrease in the insulating properties of the bilayer. At –0.6 V the conductivity increased rapidly, indicating significant failure in the stability of the tBLM. The reverse cycle showed a rapid decrease in the conductance until ~-0.4 V (see inset) where the conductivity reduces to $<1 \times 10^{-6}$ S/cm^2. In the reverse sweep a small peak was observed likely suggesting either expulsion of any residual cations within the submembrane space or a rearrangement of the tBLM. Despite the clear features in the plot, the insulating properties of the tBLM are clearly good enough to discriminate between specific ion transport through a protein and the simple electric-field driven ion transport through the membrane. Additionally, at large negative potentials, the membrane stability decreases, presumably allowing for additional cations to access the submembrane space.

Nevertheless, the decrease in stability is fully reversible as the potential is swept in the reverse direction. It should be noted that the exact potentials for membrane breakdown and cation transient peaks are highly dependent on the quality (insulation) of the membrane itself.

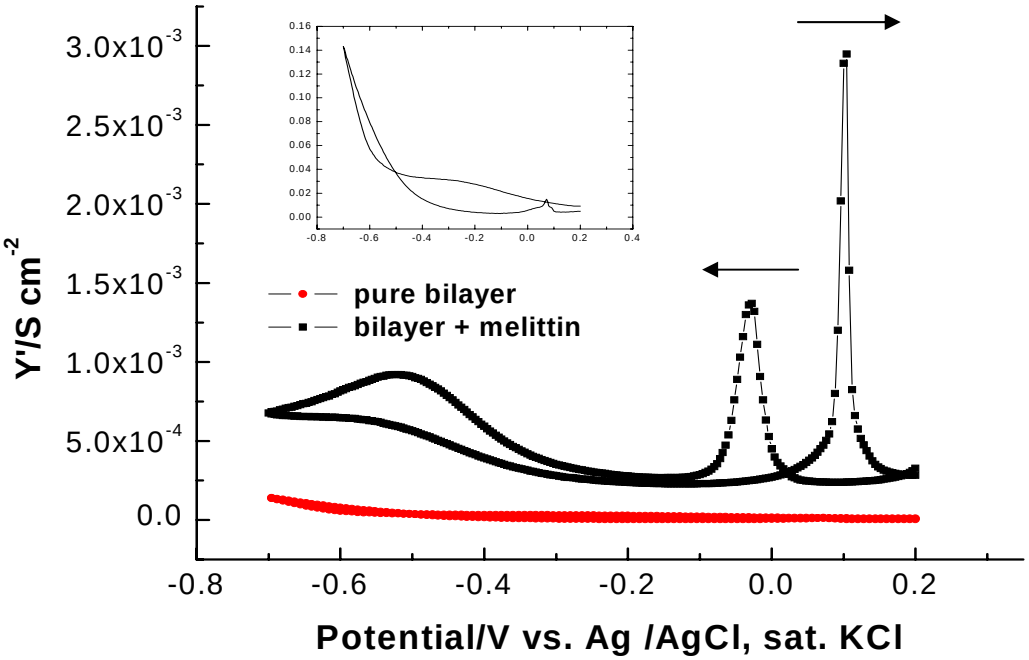

Figure 5.18: *In phase component of the admittance as a function of potential at a scan rate of 10 mV/s and a fixed frequency of 10 Hz of the mixed tBLM in a buffer solution NaCl (140 mM), KCl (6 mM), HEPES (10 mM) pH 7.4, with (black) and without (red) melittin incorporated to a final concentration of 4.57 µM. The inset shows an enlarged plot of the blank curve without mellitin.*

If melittin is incorporated into the bilayer and 6 mM K^+ are present in the solution, a conductance is noted at ~2.5 × 10^{-4} S/cm^2, which is significantly higher than the respective value of the channel free tBLM. As the potential is scanned from positive to negative potentials, a sharp peak at ~-0.032 V (FWHM ≈ 33 mV) ~1.4 × 10^{-3} S/cm^2 in height is observed, followed by a steady-state conductance of 2.7 × 10^{-4} S/cm^2. Beyond ~-0.3 V, the conductance increases until a broad peak is reached at -0.52 V. In the reverse scan the conductivity decays gradually from –0.7 V to ~-0.3 V, where a similar steady state is reached. After that the reverse scan maintains a conductivity of 2.3 × 10^{-4} S/cm^2 until a narrow peak (FWHM ≈ 12 mV) at +0.101 V is observed.

Beyond the peak the conductivity attains the original basic conductance of ~2.5×10^{-4} S/cm^2.

5.7.4 Discussion

The SPR kinetic trace shows that the thickness increased rapidly for the first ~30 min. and then continued to gradually increase well beyond the 2.5 nm expected for the second bilayer leaflet. The continuous gradual increase of the thickness in the kinetic trace is indicative of adsorption of additional liposomes. Some of the adsorbed liposomes can be washed off the surface when the surface is rinsed with the original buffer solution. When melittin is injected during the early stages of fusion (~60 min, Fig.5.16), a plateau in thickness of ~ 2.7 nm is abruptly reached. Thus, addition of proteins at the earlier stage of fusion process, in this case, melittin appears to aid in the stability of the bilayer structure.

This result indicates that contrary to the pure tBLM, melittin is in fact inserted into the membrane rather than adsorbed on the surface, in accordance with the dimension of the melittin molecule, the height of which does not exceed the thickness of a lipid bilayer.

The impedance measurements also indicate the successful incorporation of melittin into tBLMs. The decrease of the membrane resistance is in good agreement with the respective data in the literature.

Melittin is a polypeptide that binds to biomembranes such as BLMs where, at low concentrations, it induces voltage-gated channels. When bound to lipid bilayers, it adopts a α-helical conformation with most hydrophobic residues located on one side and most hydrophilic residues located on the opposite side of the helix long axis. At zero voltage, these amphipathic helices are believed to accumulate on the surface of the membrane parallel to the plane of the bilayer. At voltages negative on the opposite side with respect to the melittin, the helices form membrane spanning

aggregates that induce pore conductance[142]. Melittin has been incorporated into tBLMs also on Hg and analyzed by impedance spectroscopy[43,143]. A similar peak shaped signal was obtained in the admittance plot in the case of tBLMs based on the same DPTL molecule used in the present investigation[115], whereas in tBLMs based on oligoethyleneoxythiols a sigmoidic increase of the conductivity was obtained[126]. However, in both cases the potentials at which the signals were observed were shifted in the negative direction as compared to the gold surface. This is not surprising in view of the differences in the potential of zero charge (pzc) of both metals. Actually, Guidelli et al. made use the admittance plots of valinomycin inserted into a tBLM on mercury and on gold to find out about the potential difference across the stratified layer and as a proof of principle of equation[144]:

$$\Delta\phi - \chi_e \equiv \psi = \sigma_M \left(C_{OEO}^{-1} + C_{mem}^{-1}\right) + \chi_{OEO} + \chi_{PC,PG} \qquad \text{Equ. 21}$$

where $\Delta\phi$-χ_e is the applied potential, $\Delta\phi$, corrected for the dipole potential at the metal interface, χ_e, resulting in ψ, the potential difference across the entire gold | solution interface, σ_M is the surface charge density on the Au electrode, C_{OEO} and C_{mem} are the capacitances of the submembrane space and the membrane respectively and χ_{OEO} is the permanent dipole potential of the OEO groups in the submembrane space and $\chi_{PC,PG}$ is the dipole potential of the phospholipid head-groups. According to this equation, the potential drop across the interface is determined by the relative capacitances of each effective layer of the monolayer/bilayer system. If we assume that the dipole moments for the spacer and head-groups do not change with potential, we can show that 90-95% of the overall effective potential, ψ, drops across the lipid membrane while only 5-10% drops across the OEO spacer. This arises naturally from the relative capacitance of each "layer" previously determined from EIS measurements. Moreover, from this equation the overall potential, ψ, can be obtained at which the transmembrane potential vanishes. This effective potential is not known due to the uncertainty in the dipole potential at the metal interface, χ_e, of the polycrystalline gold surface due to electron spillover. However, comparative

measurements of valinomycin doped tBLMs on gold and on mercury performed by the Guidelli group indicated a shift in the positive direction on the gold surface. The applied potential vs. SCE when the potential across the bilayer vanishes on gold was expected to lie at about +0.2V, whereas the pzc of polycrystalline gold was reported to be +0.003 V vs. Ag|AgCl, 3M KCl[145]. In any case, at potentials at positive extremes, K^+ ions should be driven out of the submembrane space to equilibrate the potential gradient/concentration difference existing across the membrane whereas at negative extremes they are driven in. From this consideration applied to the result shown in Fig.5.18 as well as Fig.5.23 further below, the applied potential at which the transmembrane potential vanishes would be deduced to lie at around +0.05 V vs. Ag | AgCl in our case.

5.8 Incorporation of Gramicidin in mixed tBLMs

Gramicidin is a channel-forming peptide. Two of these helical peptides linked transiently to form a channel, which selectively allows monovalent cations to flow down their electrochemical gradients. The effect of gramicidin conductance has been reported using a biosensing concept[6,146-148]. Gramicidins offer experimental advantages because of their small size and exceptionally well-defined function. The incorporation of gramicidin in tBLMs is illustrated schematically in Figure 5.19.

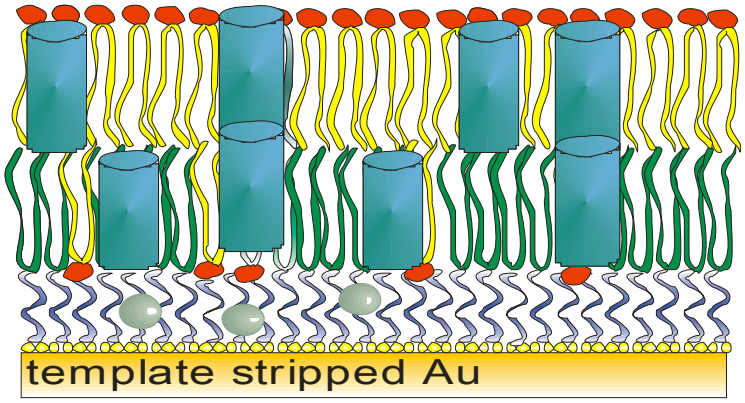

Figure 5.19: *Schematic view of the gramicidin containing bilayer*

5.8.1 Functionality of gramicidin channel in mixed tBLMs

The gramicidin was added to the flow cell before the fusion of liposomes was completed. The ion conductance of gramicidin channel in tBLMs was investigated by impedance spectroscopy. The measurements was carried out in a buffer solution of 50 mM KCl and 10 mM HEPES at pH 7.4. The impedance spectra of the monolayer and bilayer with and without gramicidin are shown in Figure 5.20.

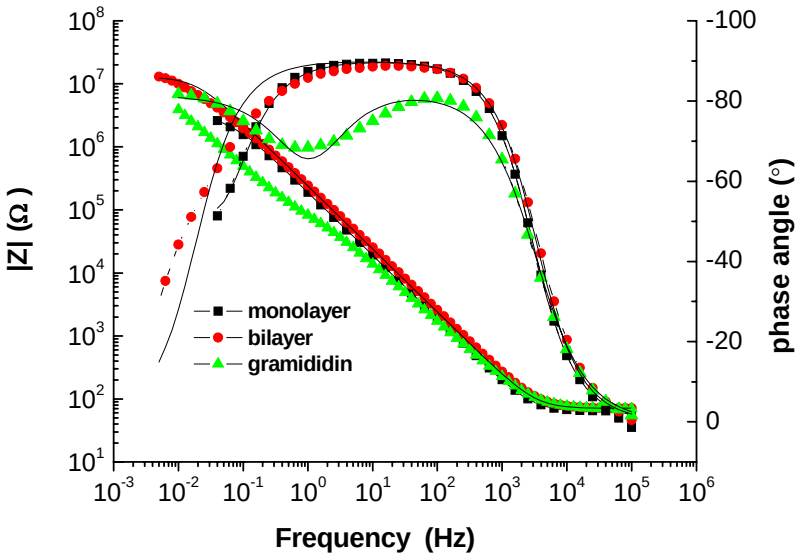

Figure 5.20: *Electrochemical impedance spectra of the mixed SAM before (■) and after (●) fusion with liposomes and with (▲) incorporation of gramicidin into the tBLM*

	R_m/MΩcm^2	Purrucker	C_m/µF cm^{-2}	C_{in}/µF cm^{-2}
SAM	2.1		1.1	3.4
Bilayer	8.7		0.7	5.1
Bilayer + Gramicidin	0.036	0.029	0.98	3.8

Table 5.8: *Fitted parameter of Figure 5.20. Measurements performed in a buffer solution KCl (50 mM), HEPES (10 mM) pH 7.4*

The data in Figure 5.20 are fitted by the equivalent mentioned above is listed in Table 5.8. An increase of the membrane resistance and decrease of the membrane capacitance due to bilayer formation is observed as demonstrated in Fig.5.16 (melittin) as well as Fig.5.20 shown monolayer in black squares, bilayer in red dots, and gramicidin insertion in green triangles. In this case the capacitance decreases from 1.1 µF/cm^2 to 0.74 µF/cm^2 while the resistance increases from 2.1 MΩ cm^2 to 8.7 MΩ cm^2, which when taken together indicates a tight bilayer. The decrease of bilayer resistance from 8.7 MΩ cm^2 to 36 kΩ cm^2 corresponding to 27 µS cm^{-2} can be attributed to the incorporation of the gramicidin channels. These values are in

agreement with the 29 kΩ cm^2 reported by Purrucker et al. for K^+ conductivity through the gramicidin D channel inserted into a lipid bilayer prepared from a lipid mixture containing cholesterol on a Si/SiO_2 surface[21].

The ion conductance effect due to gramicidin channel can be clearly displayed in the column bar plot shown below (Figure 5.21)

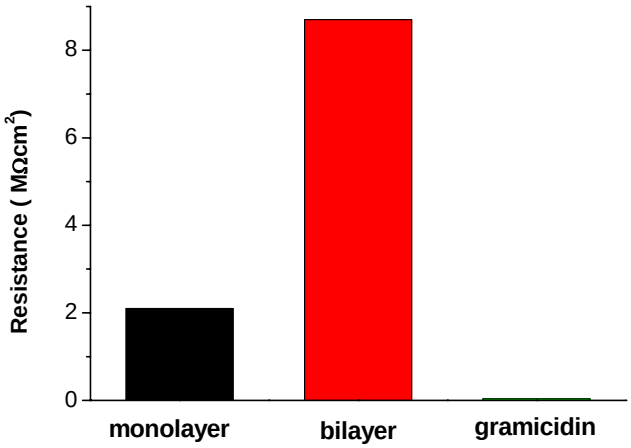

Figure 5.21: *Impedance plots as a function of insetion of gramicidin*

5.8.2 Specificity of cation conductance

Unlike melittin, gramicidin shows conductance specific for particular ions, the gramicidin conductance is dependent on the dimerization constant and on the species and the concentration of ions in the bathing solution, whereas the K^+ and Na^+ ions penetrate the channel, other ions like the bigger tetramethylammonium ($(CH_3)_4N^+$) or ammonium (NH_4^+) ions are excluded. As opening and closing of gramicidin channel can be organized through the size of ions through the channel, further investigation of changes of ions in the bathing solution was performed. Figure 5.22 shows the impedance analysis results if the cation in the bathing solution is changed from 50 mM K^+ (buffer A, black squares) to 100 mM Na^+ (buffer B, red dots) to 50 mM $(CH_3)_4N^+$ (buffer C, green triangles).

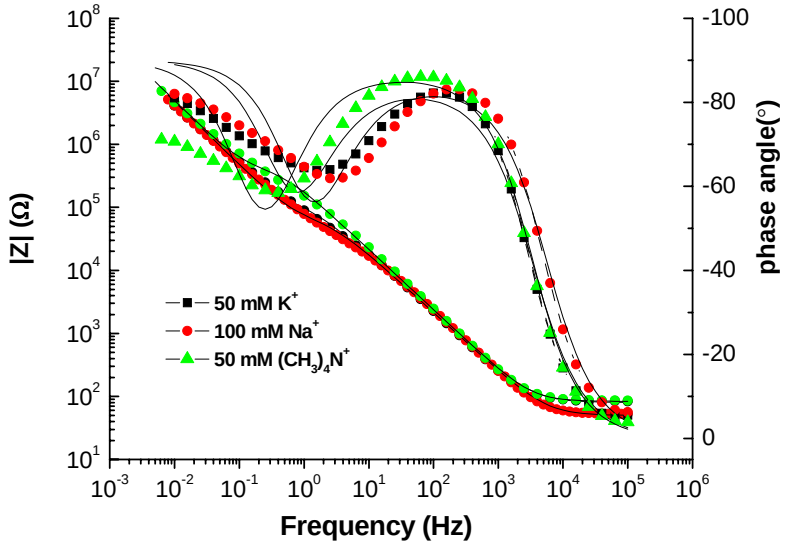

Figure 5.22: *Impedance spectra of changing of ions in bathing solution*

The data are fitted using the same approach as above and listed in Table 5.9.

These changes result in an increase of the resistance from 36 kΩ cm^2 for buffer A to 53 kΩ cm^2 for buffer B to 250 kΩ cm^2 for buffer C. These results compare favorably to the 46 kΩ cm^2 reported by Purrucker et al (for 100 mM Na^+) and 680 kΩ cm^2 for $(CH_3)_4N^+$. The decrease in resistance in the presence of $(CH_3)_4N^+$ reported here compared to that reported by Purrucker can be explained by two possible factors: the degradation of the bilayer with time or an incomplete exchange of the K^+ or Na^+ bathing solutions. This indicates the influence on the size of ions will affect the channel opening dominated by gramicidin channels. Furthermore, it proves that the gramicidin channels have been successfully incorporated into tBLMs prepared from mixed SAMs and the channel is activated.

surface /buffer	R_m/MΩcm^2	C_m/µF cm^{-2}	C_{in}/µF cm^{-2}
SAM	2.1	1.1	3.4
Lipid bilayer	8.7	0.74	5.1
Lipid Bilayer with Gramicidin 50 mM K^+	0.036	0.98	3.8
100 mM Na^+	0.053	0.99	3.2
50 mm $(CH_3)_4N^+$	0.25	0.88	3.0

Table 5.9: *EIS fitting parameters for the data in Figure 5.22.*

5.8.3 AC voltammetry

Similar results as previously described for melittin can be obtained when observing the in-phase admittance for gramicidin. Figure 5.23 (black) shows the conductance of gramicidin channels incorporated into a tBLM in the presence of K^+ ions.

As the DC potential is scanned from positive to negative potentials, an initial basic conductance is noted at ~4×10^{-5} S/cm^2. At ~0.027 V a sharp peak (FWHM ≈ 12 mV) ~2.3×10^{-4} S/cm^2 high is observed, followed by a steady-state conductance of 5×10^{-5} S/cm^2. Beyond ~-0.2 V the conductance increases gradually to the reversal potential of -0.5 V. The reverse scan follows the trend in the forward scan from –0.5 V to ~0 V. At this point the reverse scan maintains a conductivity of 5×10^{-5} S/cm^2 until a narrow peak (FWHM ≈ 10 mV) at –0.127 V is observed. Beyond the peak the conductivity attains the original basic conductance of ~4×10^{-5} S/cm^2. The peak separation of ~100 mV is significantly smaller than the observed 130 mV for melittin channels in similar bilayers.

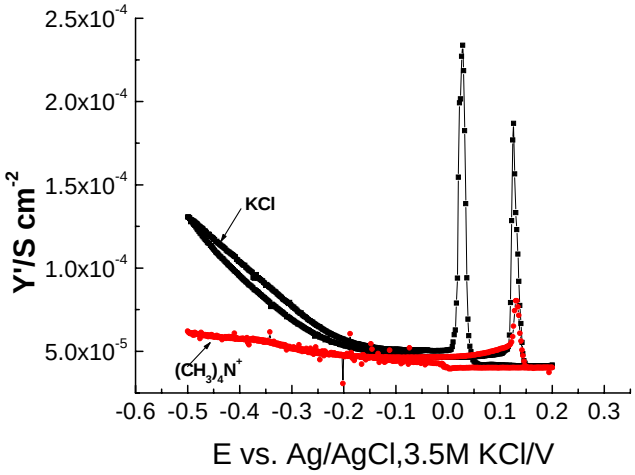

Figure 5.23: *In phase component of the admittance as a function of potential at a scan rate of 10 mV/s and a fixed frequency of 10 Hz of the mixed tBLM with gramicidin D incorporated (final concentration of 4 × 10-7 M in the bathing solution), (black) Buffer A [KCl (50 mM), HEPES (10 mM) pH 7.4]; (red)Buffer C [imidazol (10 mM) tetramethylammonium chloride (50 mM) pH 7.4].*

As a control experiment, the buffer cation was switched from K^+ to $(CH_3)_4N^+$ which should be too large to be transported by a gramicidin channel (Fig.5.23 red line). The conductivity is severely diminished as K^+ is excluded from the experiment. This result indicates that all of the observed conductivity with K^+ present can be attributed to K^+ ions specifically transported by the protein rather than non-specific electric field driven membrane decomposition. The small peak in the reverse wave can be attributed to small amounts of residual K^+ remaining after the exchange of buffers.

5.8.4 Discussion of AC-voltammetry

Ion transport through gramicidin channels incorporated into tBLMs was reported previously[143]. The physical model proposed relied on changes in the potential drop across the membrane as function of applied potential rather than the details of the transport process. More detailed kinetic analysis of gramicidin-mediated ion transport in solid-supported lipid bilayers can be found in the papers by Steinem *et al*. [149] and later by Gervasi *et al* [150]. In these reports the EIS spectra were analyzed on the basis

of equivalent circuits using the continuum model of ion transport according to which diffusion and migration of ions is regarded to take place within the membrane considered to be a thin homogeneous macroscopic phase. Potential dependence was only considered in terms of small ac perturbation on the fitted values for their equivalent circuit (i.e. no potential dependent experiments were performed). In Steinem's treatment, the authors consider the binding and desorption of the cation to the ion channel to be the potential dependent step. Other ion mobility is considered to be simple diffusion and migration. We prefer to attribute the rate limiting behavior to transport within the channel for the activated process as utilized by Gervasi. In this case, the rate coefficients for the forward and reverse transport, k_f and k_b, are potential dependent according to eq. 23 and 24

$$k_b = k_t \exp\left[-F\Delta E / 2RT\right] \qquad \text{Equ. 22}$$

$$k_f = k_t \exp\left[F\Delta E / 2RT\right] \qquad \text{Equ. 23}$$

where k_t is the potential independent, and thus the directionally independent K^+ transport rate constant and ΔE is the transmembrane potential. When non-potential dependent K^+ binding and dissociation rate constants at the solution/membrane and membrane/spacer interfaces are included, these relationships suggest a sigmoidal increase in the ion flux and hence a sigmoidal increase in the admittance as the electrode potential is swept negatively.

The sharp peaks noted in these tBLM/protein systems suggest a further limit to the observable admittance in the experiment. Two factors limit the capacity of the submembrane space: the transmembrane charge balance and the physical volume of the spacer. The volume limitation suggests a maximum physical space for cation "storage" while the charge balance suggests that the electrical capacitance of the submembrane space will change as ions accumulate[115].

The potential dependence of the channel activity is further supported by two other observations. First, the peak positions are reproducible within ±5 mV, and are

different for each channel. Second the specificity of the peak positions as shown by the ~30 mV difference in the peak hysteresis between the gramicidin D and the melittin containing membranes show a striking difference between the two ion channels in similarly-constructed membranes demonstrated in Fig.5.18 and Fig.5.23. This suggests channel specific rate coefficients of ion transfer k_t. The hysteresis can be accounted for by changes in the electrical potential distribution as ions accumulate in the submembrane space during the forward potential sweep. The accumulation of potassium cations in the submembrane space is expected to cause the applied potential to drop across the oxyethylene spacer rather than the lipid layer. This assertion is deduced from simulations that are currently conducted in our laboratory and which will be published in a forthcoming paper. Upon reversal of the potential sweep direction, the net K^+ flow is from the submembrane space to the bulk solution; however, if much of the potential drop after K^+ accumulation occurs in the submembrane space rather than across the membrane, a more positive potential will be required to expel the ions from the submembrane space.

The increased admittance observed at potential significantly negative from the peaks arising from carrier transport can be attributed to increased ionic permeability of the tBLM. This permeability effect can be subtly noted in the “blank” sample, which under ideal conditions would show no admittance changes over the entire observed potential range.

5.9 Incorporation of α-hemolysin in mixed tBLMs

The next test candidate used in this work is wild-type α-hemolysin. Different from ion channels, such as melittin and gramicidin, α-hemolysin is a simple porin, which renders the membrane permeable to any ion.

The formation of a tBLM prepared by fusion of liposomes on a mixed self-assembled monolayer based on thiolipids (DPTL) and complementary dilution molecules (TEGL) and assembly of proteinaceous α-hemolysin pores were monitored by surface plasmon spectroscopy. Electrochemical impedance measurements were performed to investigate the effect of the electrophysical features of the bilayer. α-hemolysin was injected into cell after the second leaflet of the layer has been formed by fusion of vesicle mixture onto the self-assembled mixed monolayer. Furthermore, the EIS indicated the assembly of α-hemolysin monomers to lytic pores, resulting in an increase in conductance mediated by α-hemolysin.

5.9.1 SPR measurements

SPR spectra (Figure5.24) were simulated using a three layer model including the prism, gold, and the thiolipid layers. After vesicle fusion, a fourth layer was added with respect to the phospholipids. The refractive indices used were n = 1.7, n = 1.84, n = 1.45, and n = 1.52, respectively. The thickness of the monolayer is ~ 4.6nm. A further increase in thickness occurs during the vesicle fusion, as deduced from the kinetic trace of SPR at a fixed angle of incidence. It indicates the spreading of liposomes to a distal lipid monolayer on top of the proximal lipid monolayer of mixture of DPTL and TEGL molecules to eventually form a complete tBLM[111]

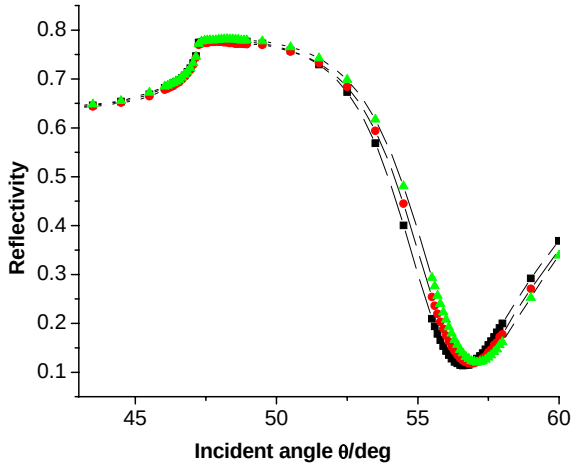

Figure 5.24: *SPR spectra of the SAM (■), bilayer (●) and addition of hemolysin (▲)*

5.9. 2 EIS measurements

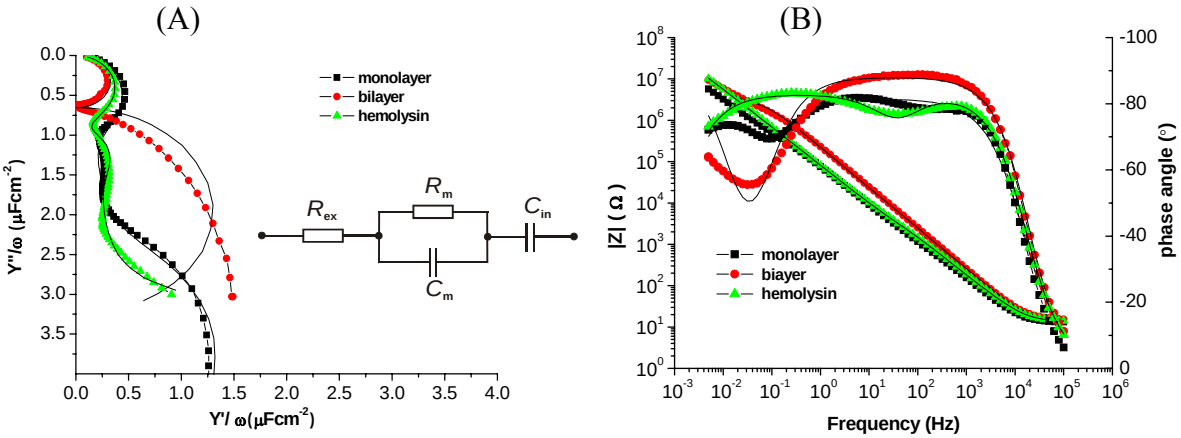

Figure 5.25: *EIS data from DPTL/TEGL mixture based tBLM with incorporation of hemolysin. Admittance plot (A) represents the change in membrane capacitance and Bode plot (B) shows the change in membrane resistance. Curves show the monolayer (■) and bilayer without (●) and with (▲) incorporated hemolysin*

Resistance and capacitance of the membrane with and without hemolysin incorporated were determined by impedance spectroscopy. The Admittance plot (Figure 5.25 A) and Bode plot (Figure 5.25 B) present the hemolysin containing

bilayer built on a DPTL/TEGL mixed monolayer in 140 mM NaCl, 10 mM HEPES solution. The data are fitted using the equivalent circuits metioned before. The values obtained by fitting for the bilayer capacitance and resistance are listed in Table 5.10.

	R_m /M Ωcm^2	C_m /μFcm^{-2}	C_{in} /μFcm^{-2}
Monolayer	0.63	1.94	4.41
Bilayer	2.06	0.82	3.25
Hemolysin	0.00056	1.54	2.17

Table 5.10: *EIS fit parameters for the Data in Figure 5.25* .

Capacitance and resistance of the monolayer was 1.94 μFcm^{-2} and 0.63 MΩcm^2, respectively, as expected for a non-homogenous monolayer due to addition of dilute molecules. During fusion, the resistance increased to 2 MΩcm^2 and the capacitance decreased to 0.82 μFcm^{-2}, indicating the insertion of free lipids and the completion of the lipid bilayer. After the addition of hemolysin, the membrane resistance decreased from 2 MΩcm^2 to 0.56 kΩcm^2, indicating ionic conductivity through the insertion of hemolysin. Throughout the experiment the inner membrane capacitance changes only slightly, but the capacitance of bilayer increases dramatically, indicating a perturbation of the bilayer structure.

5.9. 3 Incorporation of α-hemolysin as a function of time

The functionality of α-hemolysin pore was further characterized by using time-dependent impedance measurements at a constant frequency. The frequency of 10 Hz was chosen. Figure 5.26 shows the change in capacitance and resistance of bilayer as a function of time.

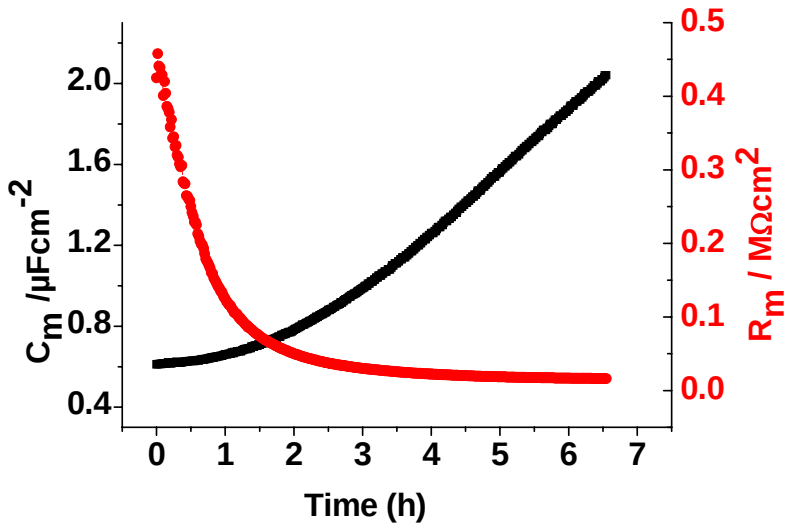

Figure 5.26: *Capacitance and resistance of bilayer at 10 Hz as a function of time.*

The result shows that the resistance decreased rapidly at the first hour, then it kept decreasing gradually during the next few hours, slowly reaching a saturation state. The capacitance changed accordingly, but to a much smaller extent. These results indicated that the α-hemolysin formed open pores with increasing time. The pores led to the decrease in the membrane resistance and further resulted in a slight perturbation the membrane as displayed in the increase in membrane capacitance.

5.9. 4 Discussion

SPR and EIS data of the mixed monolayers and tBLMs are in good agreement with the respective data described above for channel peptides such as melittin and gramicidin. From this we conclude, that a mixed tBLM had been formed prior to the incorporation of α-hemolysin. The decrease in membrane resistance by 4 orders of magnitude could then be observed as a result of incorporation of α-hemolysin in the tBLM, forming a lytic pore and allowing ions to cross the membrane.

5.10 Incorporation of M2 in mixed tBLMs

In this part, the channel-forming segment M2 from nAchR was incorporated into the tBLM in a functionally active form.

5.10.1 SPR measurements

The fusion the proteoliposomes containing M2 onto the mixed self-assembled monolayer containing mixture of thiolipid and TEGL molecules was followed by SPR at a constant angle of incident light. Figure5.27 represents the SPR kinetic and the scan results before and after vesicle fusion.

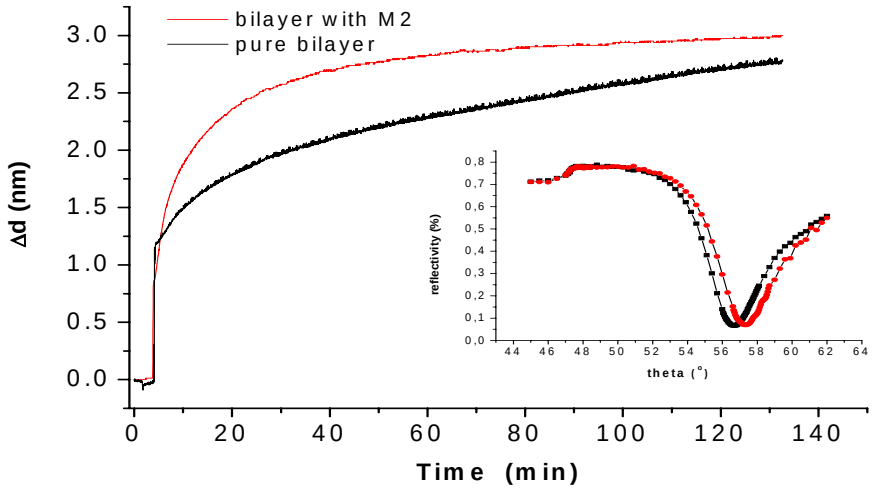

Figure 5.27: *Kinetic measurement of vesicle containg M2 fusion process. Inset represents the reflectivity scan of monolayer (■) and bilayer with M2 (●) by SPR.*

The SPR scan looks similar to the results obtained by other channel-forming peptides. The kinetic curve of the fusion of proteoliposomes shows better saturation behaviour as compared to the fusion of pure liposomes. The two phase characteristic with an increasing slope in the second phase indicates a considerable extent of vesicle adsorption, not observed in the case of proteoliposomes. This indicates a stabilizing effect of the channel protein on the formation of a lipid bilayer. The thickness of the 2nd monolayer thus obtained by vesicle fusion is about ~3 nm. Compared to the actual

pore forming sequence with only 23 to 25 amino acid residues in length, the obtained thickness from vesicle fusion is quite reasonable.

5.10.2 EIS measurements

The incorporation of M2 in tBLMs was investigated by EIS. Figure 5.28 shows the formation of monolayer and bilayer after vesicle fusion. Impedance spectra were fitted to the equivalent circuit described above, which consists of a solution resistance Rex in series with the membrane resistance and capacitance, R_m and C_m, respectively, in series with an internal reservoir capacitance C_{in}. The measurements were carried out in a buffer solution of 140 mM NaCl, 6 mM KCl and 10 mM HEPES at pH 7.4.

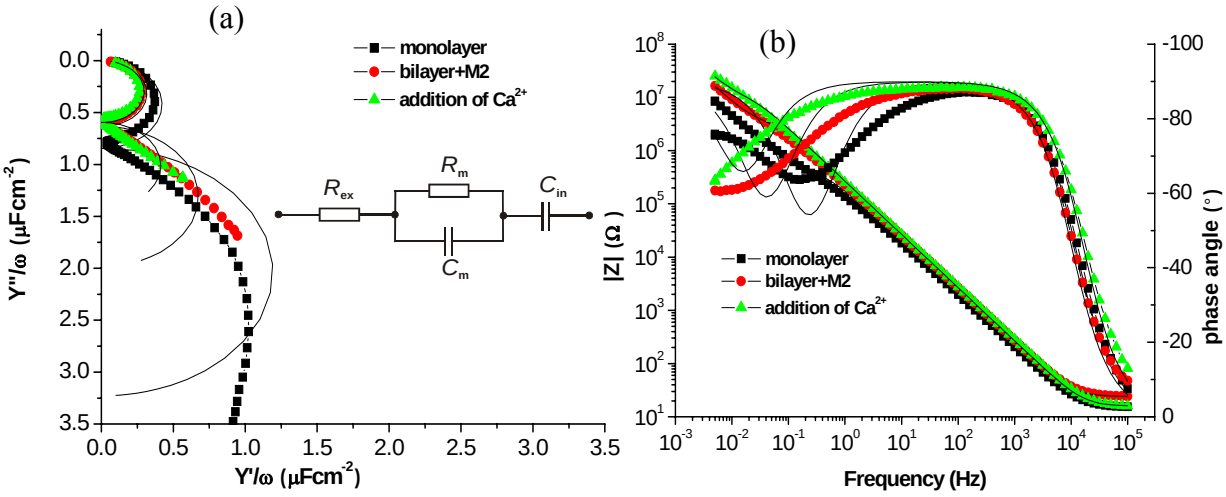

Figure 5.28: *EIS spectra of monolayer (■), bilayer with M2 (●), addition of Ca^{2+} (▲)*

The impedance spectra data by fitting to the equivalent circuit is listed in Table 5.11.

	R_m /M Ωcm^2	C_m /μFcm^{-2}	C_{in} /μFcm^{-2}
Monolayer	0.3	1.2	3.2
Bilayer + M2	2.4	0.8	1.9
Addition of Ca^{2+}	6.4	0.9	1.4

Table 5.11: *EIS fitting parameters for the data in Figure 5.28.*

The decrease in membrane capacitance and increase in membrane resistance demonstrate the formation of a bilayer containing M2. The membrane capacitance decreased from 1.2 μFcm^{-2} to 0.8 μFcm^{-2}, whereas the membrane resistance of the self-assembled monolayer increased from 0.3 $M\Omega cm^2$ to 2.4 $M\Omega cm^2$. Compared to ~ 7.2 $M\Omega cm^2$ for a bilayer without any channel, it displays moderate channel conductivity at zero bias potential. As the M2 channel is permeable to Na^+ and K^+, other ions such as Ca^{2+} are expected to have a lower permeability. With the addition of 10 mM Ca^{2+} to the flow cell, the membrane resistance increased to about 6.4 $M\Omega cm^2$, indicating that Ca^{2+} can inhibit the opening of the M2 channel

5.10.3 AC voltammetry

AC voltammetry was performed for the M2 channel incorporated in the mixed tBLM. Figure 5.29 shows the conductance of M2 channels in the presence of Na^+ and K^+ ions.

As the potential is scanned from positive to negative potentials, a sharp peak at 0.01 V 1.5 S/cm^2) in height is observed, followed by a steady-state, with a further gradually increase in conductance until a broad peak is reached. In the reverse scan, the conductivity decays gradually from -0.7 to -0.3 V, where a similar steady-state is reached. After that another sharp peak with conductivity beyond 2.5 x 10^{-3} S/cm^2 is attained. Such result obtained by AC voltammetry is a good indication of functionality of M2 channel in mixed tBLMs.

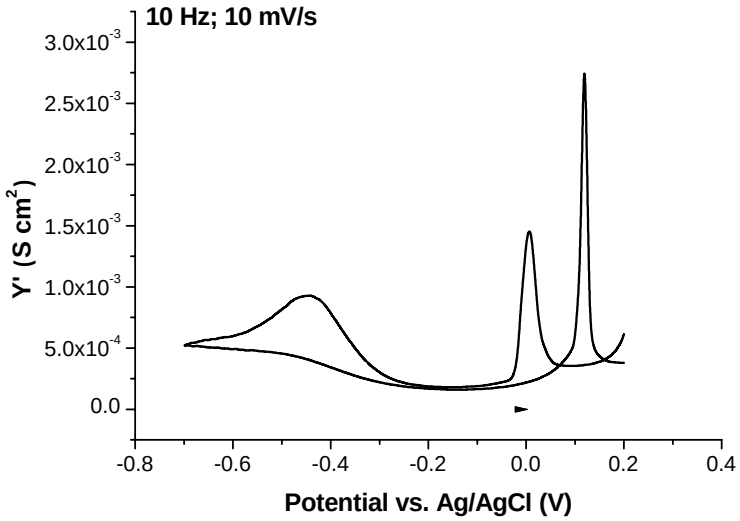

Figure 5.29: *In phase component of the admittance as a function of potential at a scan rate of 10 mV/s and a fixed frequency of 10 Hz of the mixed tBLM in a buffer solution NaCl (140 mM), KCl (6 mM), HEPES (10 mM) pH 7.4, with M2 incorporated.*

5.10.4 Discussion

The fusion of M2 containing proteoliposomes to the mixed self-assembled monolayers results in reconstitution of the M2 in the tBLMs. This is concluded from the the kinetic measurement monitored by SPR showing a clear saturation behaviour. The functionality of the channel has been investigated by impedance spectroscopy. The decrease in membrane capacitance and increase in membrane resistance are in good agreement with the formation of a bilayer. The value obtained from impedance spectra after fitting with the equivalent circuit displays a bilayer with channel conductivity, indicating that the M2 channel was inserted into the bilayer. Furthermore, the increase in membrane resistance after addition of Ca^{2+} indicates the inhibition effect, leading to a decreased permeability of ions across the membrane. The most convincing proof of the functional incorporation comes from AC voltammetry. The sharp peak signals observed correspond to the ones for other channel forming proteins whereas the location of the peaks seems to be channel specific[14]

5.11 Incorporation of Maxi-K channel in mixed tBLMs

As described above, the porin such as hemolysin, channel-forming peptides like Melittin, Gramicidin, and M2 have been successfully incorporated into such tBLMs in a functionality active form. The question to be answered is: Can a large channel protein also be incorporated retaining its activity in mixed tBLMs? Therefore, the next candidate for further investigation will be the Maxi-K channel, which is more complicated and more interesting for biosensor applications. The schematic representation of the Maxi-K channel incorporated is shown in Figure 5.30.

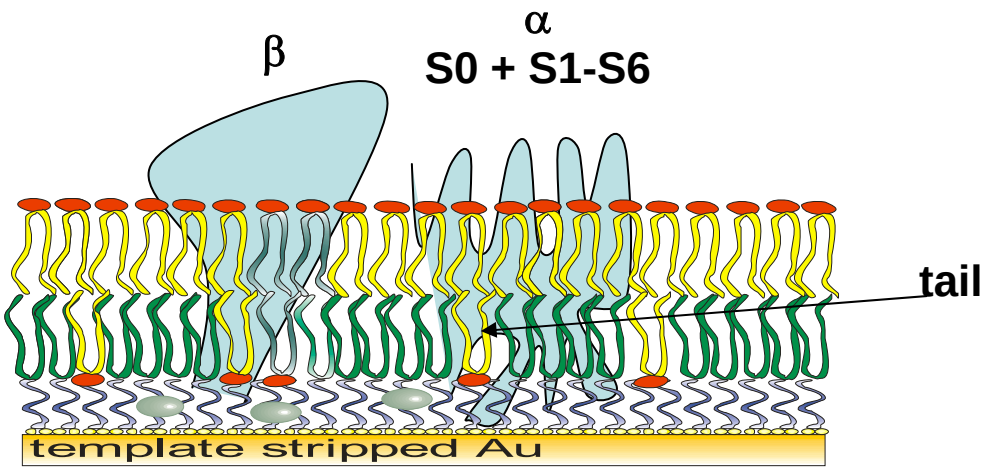

Figure 5.30: *Schematic representation of Maxi-K channel incorporated into tBLM*

5.11.1 SPR measurements

The conversion of the self-assembled monolayer mixed thiolipids with dilution molecules into the tethered lipid bilayer membrane was achieved by vesicle fusion as described under Material and methods. Fusion of vesicles containing Maxi-K resulted in an increase of thickness about 3.5 nm shown in Figure 5.31.

The obtained 2nd layer corresponds to the expected average thickness of a bilayer with Maxi-K channel protein, which has an estimated molecular weight of 120,000 Da.

The kinetics of the fusion of Maxi-K containing vesicles shows better saturation behaviour as compared to the fusion of pure liposomes. Such observation is similar to that which we obtained from M2. This further proves that fusion of liposomes containing channel forming proteins can stabilise the formation of a lipid bilayer. The 2nd layer thickness obtained by fusion suggests that reconstituted Maxi-K channels contribute to the layer thickness. The thickness between with the Maxi-K containing and without Maxi-K is about 1 nm. Rinsing of the surface did not change the thickness of the layer thus formed, implying the Maxi-K channel forms a stable second monolayer on top the self-assembled mixed monolyer.

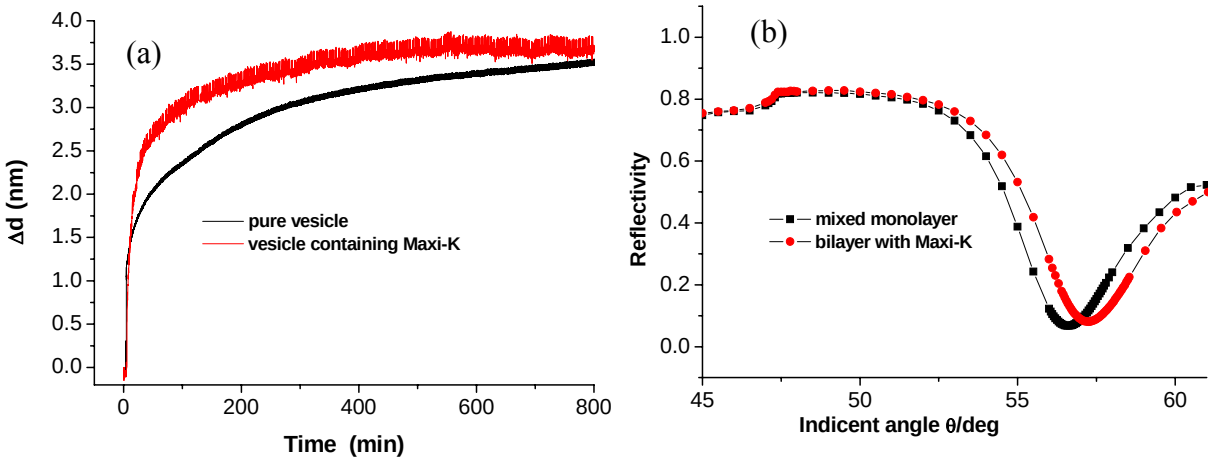

Figure 5.31: *(a) SPR kinetic trace(a) and (b) scan curves of formation of bilayer with Maxi-K..*

5.11.2 Activity of Maxi-K channel in mixed tBLMs

The Maxi-K channel have been well-studied by the patch-clamp technique for ion permeability, but the incorporation of this big channel into a tBLM has never been reported. In order to study the ion transport across a tBLM through Maxi-K channel, impedance spectroscopy was further employed to investigate ion conductivity by changing the bias potential since the Maxi-K channel is a voltage-gated channel.

Maxi-K channel is potassium channels formed a family of K+ selective, voltage-gated channels in excitable membrane such as neuronal and muscle cell membranes. Such gated ion channels are open or closed depending on whether the associated receptor has been activated by a change in transmembrane electrical potential. Impedance spectra of a mixed self-assembled monolayer, bilayer formed after fusion of vesicle containing Maxi-K channel to the monolayer, and activity of channel incorporated after changing of bias potential are shown in Figure 5.32.

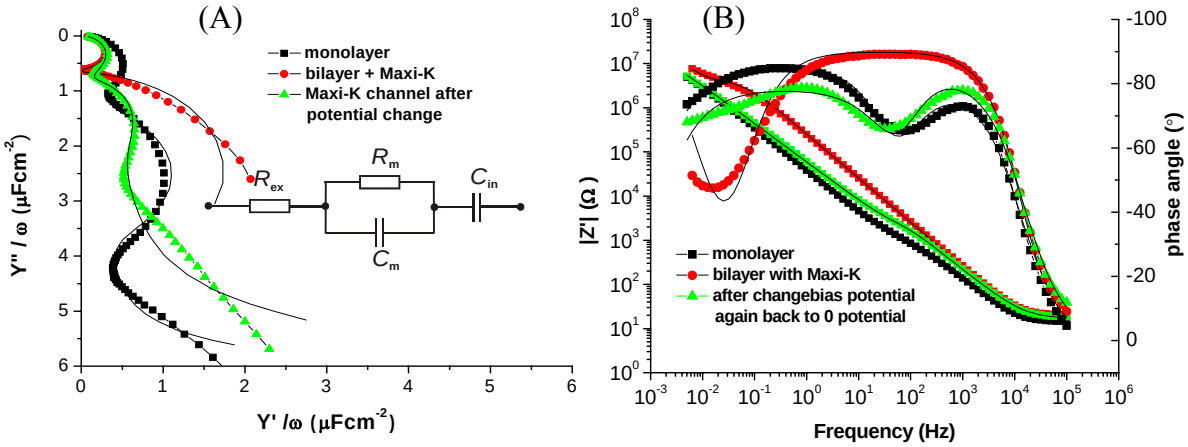

Figure 5.32: *Impedance spectra of monolayer (■), bilayer with Maxi-K channelbefore (●) and after application of a bias potential of -0.2V and back to 0V (▲).*

The EIS data are fitted using the equivalent circuits shown in the inset. The fitting results are listed in Table 5.12. The membrane capacitance decreased from 1.7 μFcm^{-2} to 0.7μFcm^{-2}, while the membrane resistance increased from 2.84 kΩcm^2 to 3.5 MΩcm^2, indicating the formation of a bilayer containing Maxi-K channel. To activate the channel, a bias potential of -0.2V was applied for ~30 min. The membrane capacitance kept constant during the change in bias potential. The subsequent measurement was taken again at a bias potential of 0V immediately after finishing the EIS measurement at -0.2V. The EIS spectrum measured shows a decreased membrane resistance of 3.34 kΩcm^2.

	R_m / MΩcm^2	C_m / µFcm^{-2}	C_{in} / µFcm^{-2}
SAM	0.002844	1.66	4.32
Bilayer +Maxi-K	3.5044	0.74	3.95
After application of a bias potential of -0.2V, then back to 0V	0.003342	0.78	3.14

Table5.12: *EIS fitting parameters for the data in Figure 5.32.*

This observation is taken as an indication of a voltage-gated channel, leading to an increased permeability. Figure 5.33 demonstrates the incorporation of Maxi-K channel into a tBLM and its activity as a voltage-gated channel.

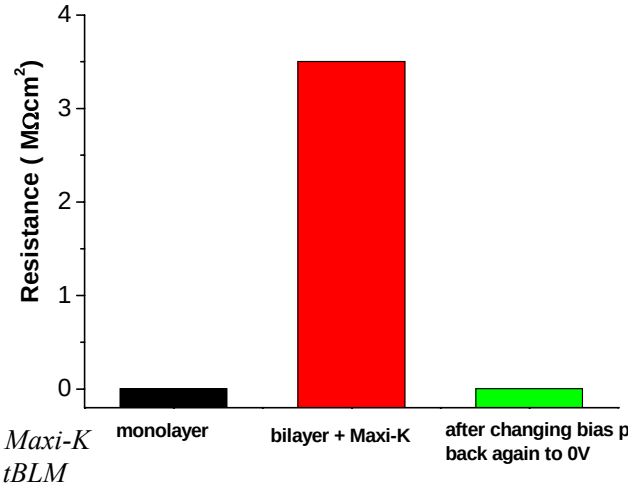

Figure 5.33: *Maxi-K channel incorporated into a tBLM*

5.11.3 Activation of Maxi-K channel by changing calcium concnetration

As Maxi-K channels are activated by intracellular Ca^{2+} and membrane depolarization in a highly synergistic manner[151-152], the calcium ion effect on the ion conductance of Maxi-K channel was investigated by changing of Ca^{2+} concentration of the buffer from low concentration to high concentration. After application of a bias potential of -0.2V, and back to 0V again, the Ca^{2+} solution was then added to the bathing solution.

Electrochemical impedance spectroscopy monitored the changes in membrane capacitance and resistance as a function of [Ca^{2+}] without changing of the membrane potential. Figure 5.34 presents the changes in membrane resistance as a function of Ca^{2+} concentration.

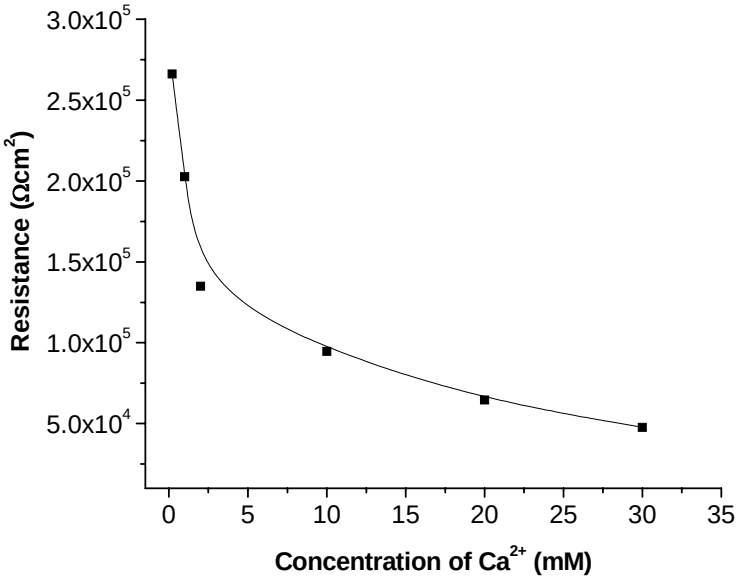

Figure 5.34: *Ca^{2+} effect on membrane resistance*

The result clearly displays that the membrane resistance decreases with the increase of calcium ions in the buffer. It indicates that the opening of the channel is affected by changing the Ca^{2+} in bathing solution.

5.11.4 Inhibition effect of the Maxi-K channel

The Maxi-K channel has been successfully incorporated into tBLMs by using our system. The opening of Maxi-K channel has been proven as well either by changes in membrane potential or by increasing of Ca^{2+}. One question still remains, how can we prove that the decrease of membrane resistance is caused by the opening of channel instead of a defect in the bilayer membrane? In order to answer this question, inhibitors of the Maxi-K channel were studied.

High conductance calcium-activated Maxi-K channels are potently blocked by a family of indole diterpenes that includes paxilline. Paxilline stimulates binding of charybdotoxin (ChTX) to Maxi-K channels in vascular smooth muscle and blocks these channels in electrophysiological experiments[153]. These results suggested that paxilline blocked Maxi-K channels at a site distinct from the ChTX binding site located near the external entrance to the pore. Here we have examined the blocking of Maxi-K channel after application of paxilline. The experiment was done in such way: first of all, a bias potential of -0.2V was applied, then EIS was measured again at a bias potential of 0V, furthermore, EIS spectra were measured at 0V after addition of Ca^{2+} in the bathing solution. Finally paxilline was added in order to test the blocking of Maxi-K channel. The dose-response relation for channel block by paxilline is shown in Figure 5.35.

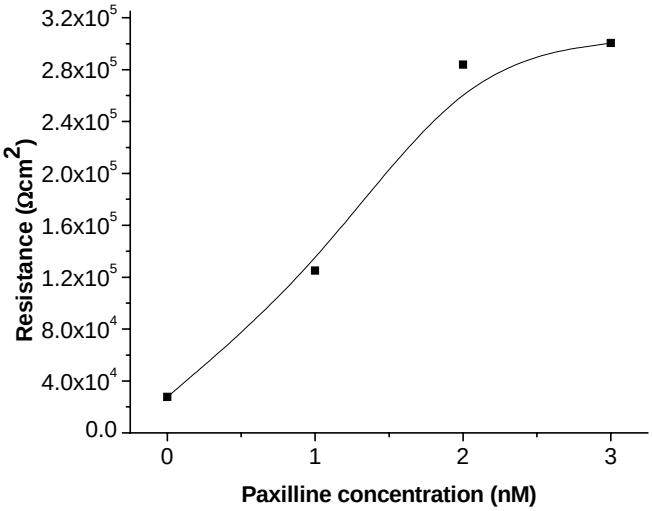

Figure 5.35: *Dose-response relation for Maxi-K channel block by paxilline*

The data shows inhibition of membrane resistance in a single experiment with the increase in concentration of paxilline. The membrane resistance increased when the paxilline was added as inhibitor, indicating that the channel was blocked.

A quite interesting finding is that the channel was closed by the application of paxilline, but after some time, the channel opens again, displaying a decrease in

membrane resistance again. It implies that paxilline blocks the channel for a short time only and after that the channel is recovered.

5.11.5 Conclusion

The Maxi-K channel has been successfully incorporated into tBLMs by using our system. The opening of Maxi-K channel has been proven as well either by application of a membrane potential or by increase of Ca^{2+}. As inhibitor of Maxi-K channel, paxilline was shown to inhibit the opening of these channels by binding to the ChTX site of the channel.

To summarize the successful incorporation of large Maxi-K channels into tBLMs based on the self-assembled monolayer of DPTL thiolipids with TEGL as complementary dilution molecules, Figure 5.36 displays the complete results in one column bar graph. It clearly demonstrates the large Maxi-K channels has been successfully inserted and the activity of the channel is proven by the opening and closing of channels after changes of membrane potential or Ca^{2+} concentration and after addition of paxilline.

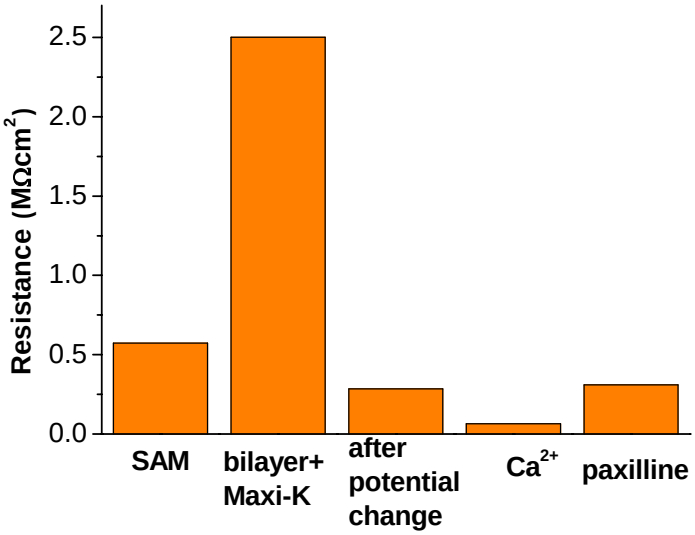

Figure 5.36: *Membrane resistances as a function of Maxi-K channels incorporation*

5.12 Incorporation of nicotinic Acetylcholine Receptor in tBLMs

The nicotinic acetylcholine receptor (nAChR) is the neurotransmitter-gated ion channel responsible for the rapid communication between cells at the nerve-muscle synapse and the brain[154-156]. The nAChR is a postsynaptic membrane protein composed of five integral membrane proteins in a stoichiometry of $\alpha_2\beta\gamma\delta$. The five subunits are arranged in a circular fashion around a central hole that provides an ion pathway across the postsynaptic cell membrane. The receptor complex binds two molecules of acetylcholine. Acetylcholine binding induces the opening of the channel. The coupling between the two acetylcholine binding sites and the channel is an allosteric mechanism because the binding of a ligand causes a conformational change on a distant place in the receptor unit[157]. Among the family of the ligand-gated ion channels, the nAChR is the best characterized. This receptor has been studied in planar lipid membrane[158], black lipid membrane[159], supported lipid membrane[78], and tBLMs[79].

In the present study, an attempt is made to directly fusion of membrane fragments containing the AChR with the mixed monolayers, to eventually obtain the AchR incorporated in a tBLM.

5.12.1 SPR measurements

Fusion the membrane fragments isolated from Torpedo electric organ containing acetylcholine receptor onto the mixed self-assembled monolayer was followed by SPR at a constant angle of incident light. The result of kinetic measurement is shown on Figure 5.37. SPR spectra measured before and after the fusion process are given in the inset of Figure 5.37 and illustrate the increase in layer thickness. The AchR fragment containing solution is injected into the flow cell and a rapid increase in the SPR response is observed, followed by a clear saturation behavior. The optical thickness of the final layer was ~5 nm, definitely higher than the thickness obtained by the fusion of pure liposomes. The increment between the layer of receptor

containing AchR membrane fragments and pure vesicle layer is ~ 2.2 nm. Compare to the dimension of AchR with 120Å length and 65Å diameter, this difference could be an indication of the incorporation of acetylcholine receptor in the mixed tBLM, particularly in view of the clear saturation kinetics of the fusion process.

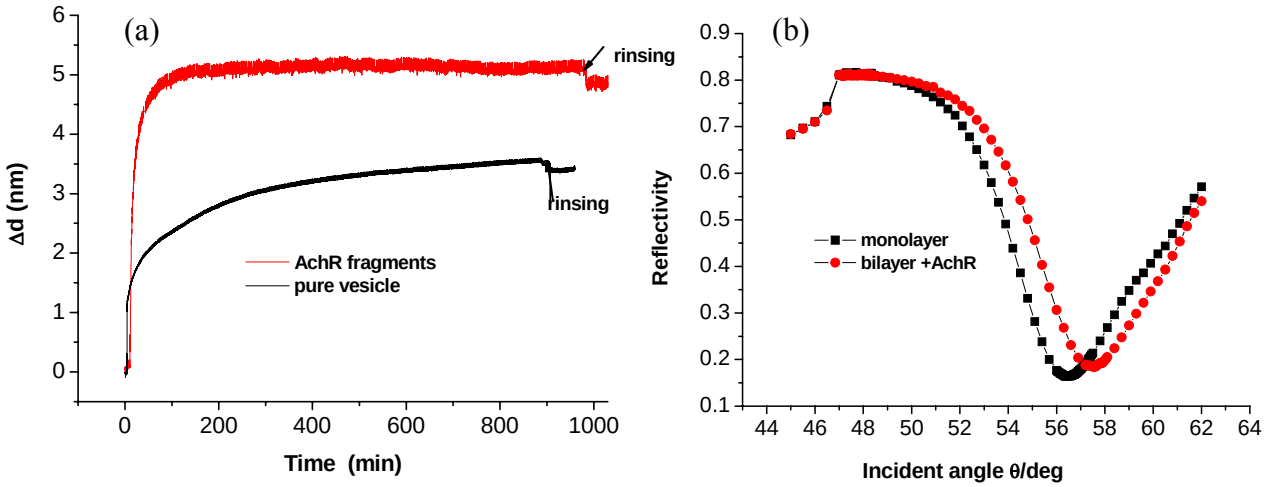

Figure 5.37: *Formation of AChR containing bilayer monitored by SPR..(a)*

5.12.2 SPFS measurements

Surface Plasmon Resonance Fluorescence Spectroscopy (SPFS) was used to further investigate the incorporation of nAChR in a tBLM. The labelled neurotoxin α-bungarotoxin was used to recognize nAChR inserted in the membrane. In this work, α-bungarotoxin labelled with Alexa Fluro 647, a fluorescent dye was used as a probe to detect nAChR inserted in the model membrane. The fluorescence of α-bungarotoxin labelled with Alexa Fluro 647 was measured simultaneously as a function of the angle of the incident light. The binding of the fluorescence of α-bungarotoxin labelled with Alexa Fluro 647 to the receptor is illustrated in Figure 5.38.

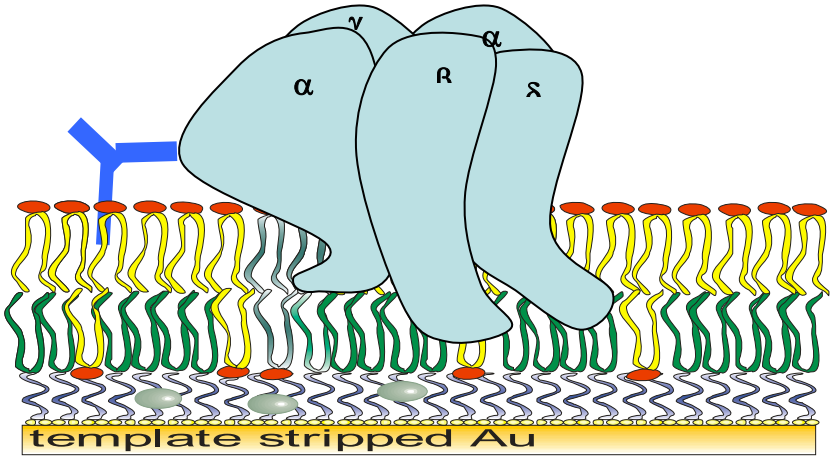

Figure 5.38: *Schematic illustration of the detection of acetylcholine-receptor interaction at a tBLM by the α-bungarotoxin labeled with a fluorescent molecule using SPFS*

First of all, nAChR fragments were injected to the flow cell, and after termination of the fusion, excess of fragments were removed by rinsing with buffer. The solutions of the AF α-bungarotoxin at a final concentration of 0.01 mg/ml were injected into the flow cell at a flow rate of 36 µl/min. After incubation for 30 min, the surface was rinsed with buffer for 10 min until equilibrium was reached in order to remove free and loosely associated dye molecules on the membranes, where SPS/SPFS scan were performed to obtain the fluorescence signals of the AF α-bungarotoxin binding to the lipid surface. Binding of AF α-bungarotoxin to the nAChR at the membrane was determined by the fluorescent intensity of the AF α-bungarotoxin bound to the receptor.

As shown in Figure 5.39, the SPFS scan displays the effects before and after the AF α-bungarotoxin binds to the receptor. As α-bungarotoxin has strong binding affinity to the receptor, when both of them bind to each other, a significant increase in fluorescence signal was detected. The minimum in reflectivity of the SPR spectrum coincides with the maximum in fluorescence of the SPFS spectrum. The increase in fluorescence on the surface indicates the binding of α-bungarotoxin to the AChR.

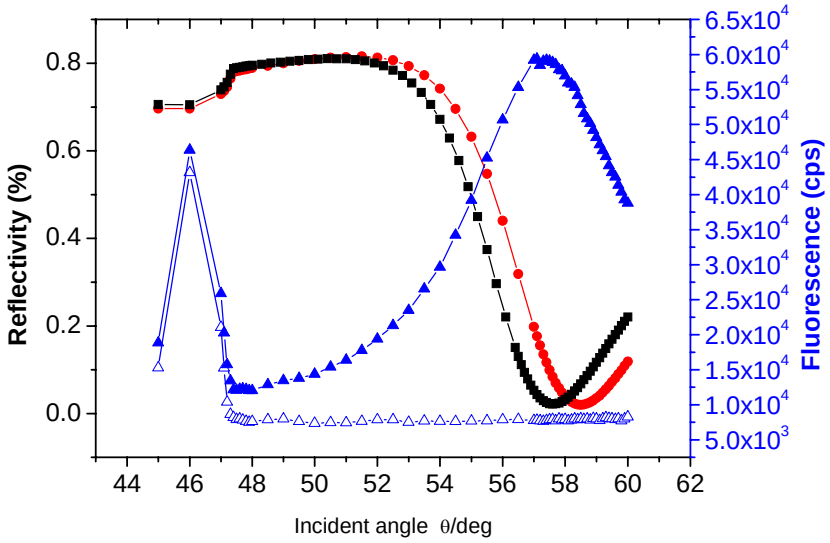

Figure 5.39: *Reflectivity and fluorescence curve scans in the SPR and SPFS mode, respectively. Reflectivity scans for monolayer (■) and bilayer with AChR incorporated (●). Fluorescence scans of the tBLM with (▲) and without (△) α-bungarotoxin labelled with Alexa Fluro 647 binding to nAChR at the membrane.*

To make sure of the specific binding of α-bungarotoxin to the AChR at the membrane, another experiment was done by first adding non-fluorescent labelled α-bungarotoxin to the bilayer containing AChR, then it was rinsed with buffer before the addition of the solution of fluorescence labelled α-bungarotoxin. Incubation took about 20 min, after that the sample was rinsed with buffer, whn the fluorescence scan was performed to detect whether there was any increase in the fluorescent intensity. The SPFS results are shown in Figure 5.40.

The results shows no big change in fluorescent intensity compared to the results shown in Figure 5.39, indicating that no fluorescent labelled α-bungarotoxin binds to the AChR, while the binding sites were bound by the non AF-labelled α-bungarotoxin thus AF labelled α-bungarotoxin had no chance to bind again and no fluorescence signal could be detected by SPFS.

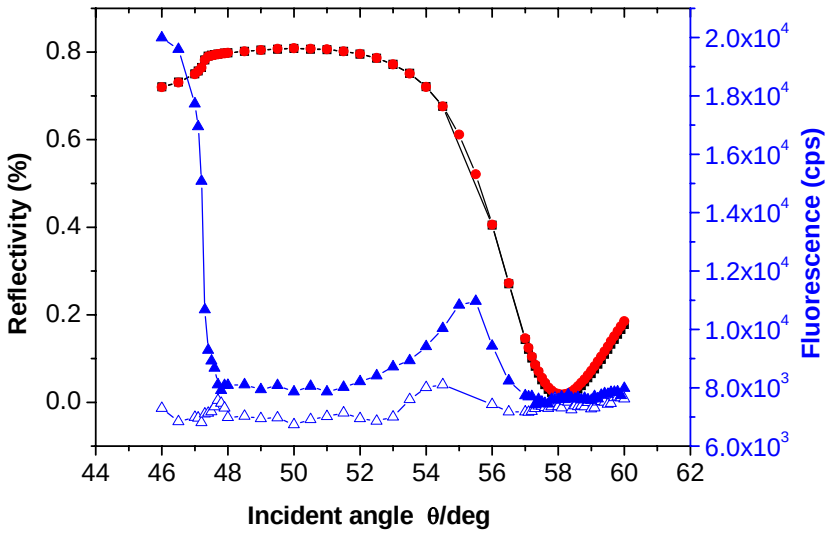

Figure 5.40: *Reflectivity and fluorescence curve scans in the SPR and SPFS mode, respectively. Reflectivity scans for free toxin (■) and α-bungarotoxin labelled with Alexa Fluro 647 (●). Fluorescence scans of the tBLM with (▲) and without (Δ) α-bungarotoxin labelled with Alexa Fluro 647 binding to nAChR at the membrane.*

5.12.3 Activity of incorporated nAChR in mixed tBLMs

The acetylcholine is a neurotransmitter and the neutral agonist of the acetylcholine receptor. The binding of acetylcholine molecules to the extracellular ligand-binding domain of the receptor triggers a structural change on the glycoprotein complex that opens transiently the cation-permeable ion channel located in the cell membrane. The flux of cations through the receptors rapidly depolarizes the postsynaptic membrane, and the signal is propagated along the electrically excitable membrane toward the next nerve cell.

The formation of a bilayer containing AchR fragments was monitored by EIS as well. Figure 5.41 presents the time dependence to form AChR containing bilayer at a fixed frequency of 10Hz. The decrease in membrane capacitance and increase in membrane resistance demonstrate the formation of a bilayer containing AChR.

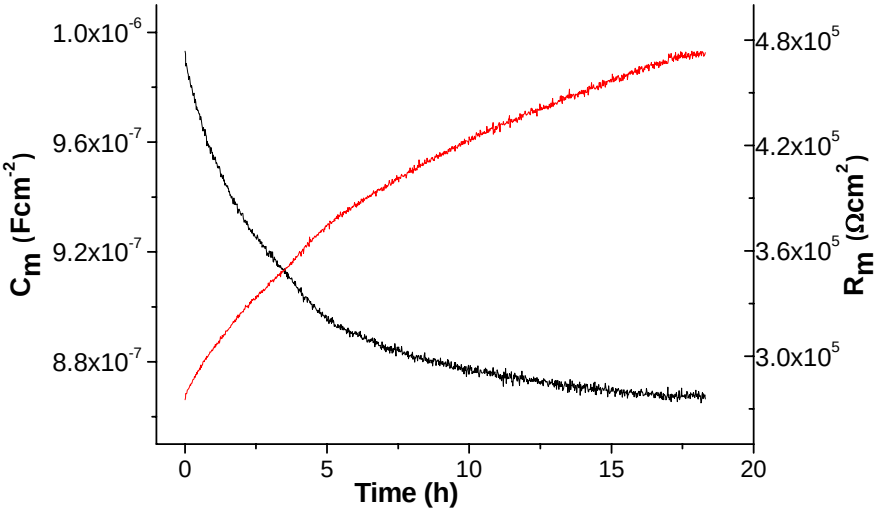

Figure 5.41: *Capacitance and resistance as a function of time detected at 10 Hz.*

With the addition of agonist acetyl choline to the flow cell, an indication of decrease in membrane resistance is displayed in the Bode plot (Figure5.42).

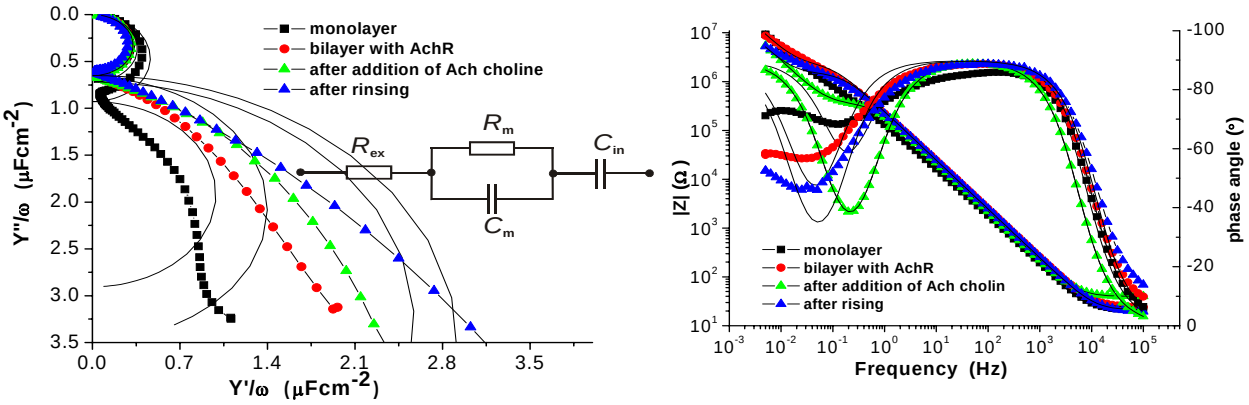

Figure 5.42: *EIS spectra of monolayer (■), bilayer with AChR (●), addition of acetylcholine (▲), rinsing (▲)*

The EIS data are fitted using the equivalent circuits shown in the inset. The fitting results are listed in Table 5.13.

	R_m / MΩcm^2	C_m / µFcm^{-2}	C_{in} / µFcm^{-2}
Monolayer	0.3	1.4	2.9
Bilayer + AchR	1.8	0.8	3.5
Addition of Ach choline	0.34	0.8	5.6
After rinsing	1.6	0.7	6.5

Table5.13: *EIS fitting parameter for data in Figure 5.42.*

The resistance of the self-assembled monolayer increased from kΩcm^2 to ~ 1.8 MΩcm^2, which indicates a highly insulated bilayer. At the addition of AchR the membrane resistance drops to 341.5 kΩcm^2, after rinsing with buffer, the membrane resistance returns to 1.6 MΩcm^2. This experiment demonstrates that the opening and closing of the channel are regulated by the binding of acetylcholine to the receptor.

5.12.4 Discussion

Fusion of the nicotinic Acetylcholine receptor membrane fragments with the mixed monolayers, directly leads to the formation of a tBLM with the AchR receptor successfully incorporated into our model system. The fusion of AChR containing membrane fragments resulted in 5 nm increment obtained by SPR. This observation suggests that AChR was incorporated into mixed tBLMs, compared to the thickness increase of 3 nm obtained by fusion of pure vesicle to the mixed monolayers.

The binding of the α-bungarotoxin labelled with fluorescence dye to the AChR at the membrane was detected using SPFS. α-bungarotoxin recognized the AChR binding site within the membrane. These results demonstrate a successful incorporation of acetylcholine receptor in the membrane in an orientation with the AchR binding side pointing into the bating solution. The negative control measurement indicates that no binding signal was detected by SPFS when the binding sites had been firstly occupied by non-labelled toxins.

Still more convincing both the formation of a lipid bilayer and the functionality of immobilised AchR in the mixed tBLMs are the data obtained by EIS. The EIS spectra display a decrease in membrane capacitance and an increase in membrane resistanc, indicating the incorporation of AchR in mixed tBLMs. The capacitance of 0.8µF/cm2 in particular is very characteristic for a lipid bilayer. The further decrease in membrane resistance after addition of acetylcholine showed the opening of the channel, but the effect observed by EIS was comparatively small, indicating that the channel was not fully functional.

5.13 Incorporation of Bacteriorhodopsin in mixed tBLMs

Bacteriorhodopsin (bR) is the light driven proton pump from the purple membrane of *Halobacterium salinarium* containing a retinal moiety covalently attached by a Schiff-base linkage to Lys[216]. Few reports exist concerning the reconstitution of BR into solid supported membranes. Seifert *et al.*[160] managed to adsorb purple membrane sheets onto a solid supported bilayer immobilized on a gold substrate. Their results were similar to those using a BLM published earlier by Bamberg *et al.*[161] Puu *et al.*[162] prepared bR-containing SBLMs either by direct fusion of vesicles onto platinum substrate or by fusion of vesicles on a preformed LB-monolayer. Steinem *et al.*[163] showed the incorporation of bR into a solid supported bilayer by fusion of reverse phase vesicles on chemisorbed monolayer of DMPTE on gold surface. Here we present an alternative reconstitution technique based on fusion of vesicles containing bR onto a self-assembled monolayer prepared from a mixture of thiolipids and spacer TEGL molecules tethered on gold electrodes (Figure 5.43).

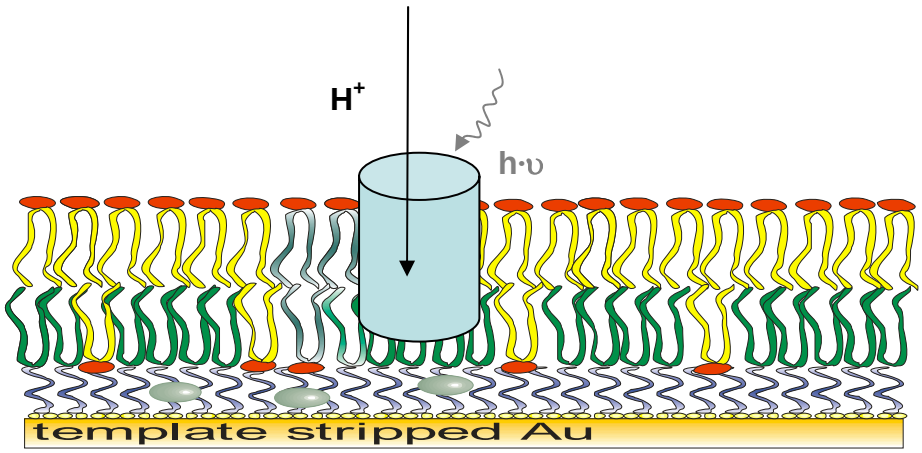

Figure 5.43: *The schematic architecture of tBLM with incorporated bacteriorhodopsin*

5.13.1 Fusion of purple membranes with mixed SAMs

The formation of the bilayer in which bR was incorporated was monitored by means of impedance spectroscopy. It enables us to follow the formation process and to determine the electrical properties of the bilayer as a measure of its quality. Figure

5.44 shows the typical impedance spectra before and after fusion of purple membranes.

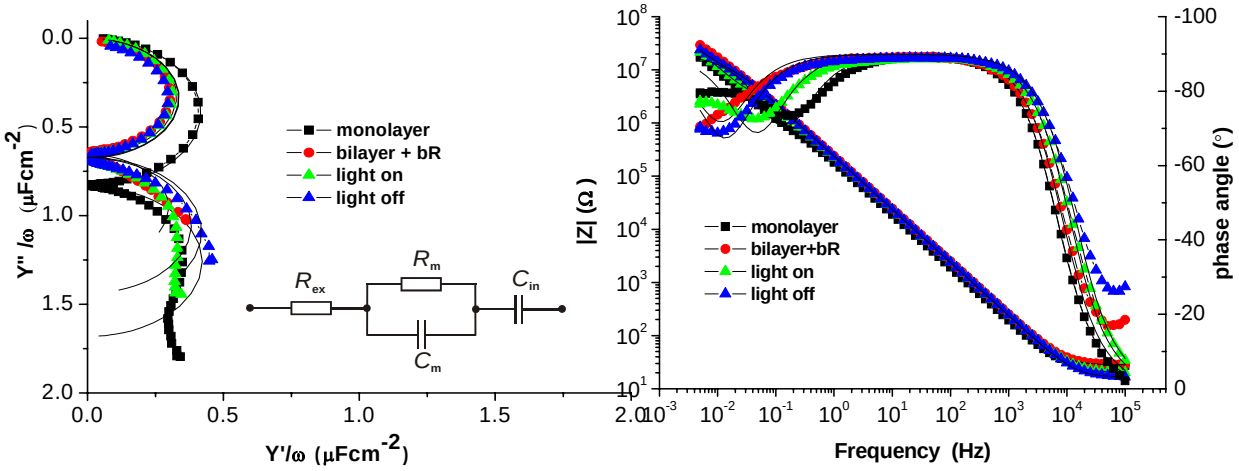

Figure 5.44: *Impedance spectra of a monolayer (black ■) and bilayer (red ●) obtained by fusion of bR-containing vesicles, and proton transfer induced by light on (green ▲), light off (blue ▲) The continuous lines with corresponding colours are the results of the fitting to the equivalent circuit given in the inset of Figure 5.45.*

	R_m / MΩcm^2	C_m / μFcm^{-2}	C_{in} /μFcm^{-2}
SAM	0.48	1.66	1.68
Bilayer + bR	7.29	0.9	1.4
Light On	1.82	0.9	1.4
Light Off	6.96	0.9	1.5

Table 5.14: *EIS fitting parameters for the data in Figure 5.44.*

The fitting results for data in Figure 5.44 are listed in Table 5.14. The capacitance and resistance of the monolayer are 1.7μFcm^{-2} and 476.6 kΩcm^2, respectively. Values of 0.9μFcm^{-2} for the membrane capacitance were obtained for the second monolayer produced by the fusion of bR-containing vesicles to the mixed monolayers. During the fusion process, the membrane resistance increased to 7 MΩcm^2, indicating a highly insulated tBLM eventually formed. These observations demonstrate the

formation of single lipid bilayers, in which the purple membrane has been incorporated. The length of the bR molecule is sufficient to span the thickness of the liplid bilayer. When the film was illumilated, the membrane capacitance did not change, but the membrane resistance decreased. When the light was off, the membrane resistance could be recovered.

5.13.2 Light-induced proton pumping

Measuring the membrane resistances upon illumination of the coated gold surfaces made it possible to check the proton pump activity of the immobilized bR. Figure 5.45 indicates a typical result of experiment. The changes in membrane resistance measured after switching the light on or off demonstrate that the bR protein was successfully reconstituted and maintained its pump activity.

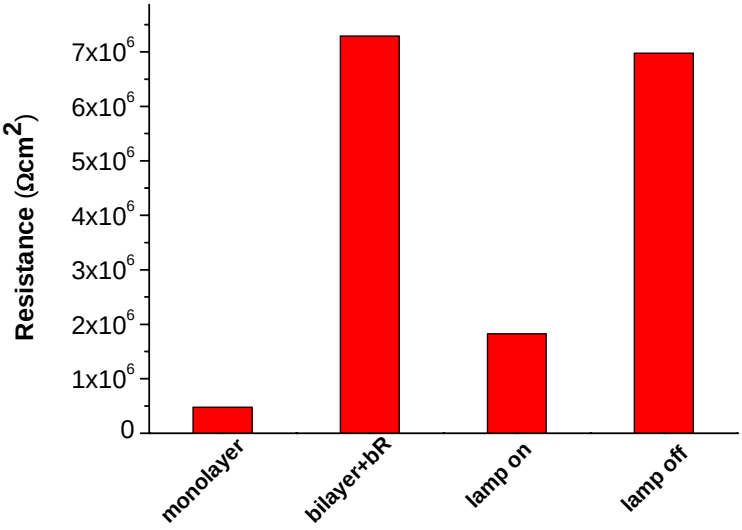

Figure 5.45: *Membrane electrical response after switching the light on and off.*

The results indicate that the membrane resistance decreases when the light is on, and it increases again and lead to an almost recovery of the initial resistance when the light is switched off. This can be explained that light energy is converted into an electrochemical pH gradient across the cell membrane upon illumination, leading to proton transport across the membrane

5.13.3 Functionality of bacteriorhodopsin in mixed tBLMs

In order to investigate how long does it take for the membrane resistance to recover, we monitored the recovery of membrane resistance in real time. The change in membrane resistance as a function of time when the light was switched off is shown in Figure 5.46. The result indicates that the initial high resistance is fully recovered by switching off the light. It indicates that the illumination effect due to bR activity is fully reversible.

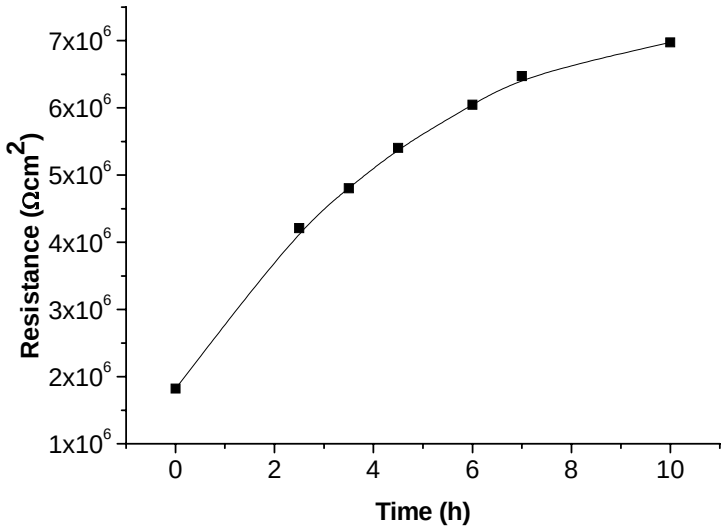

Figure 5.46: *Impedance as a function of time when the light was off.*

5.13.4 Discussions

By means of impedance spectroscopy the insulating properties of the membranes obtained by fusion of purple membranes onto mixed tBLMs were investigated. It led to the formation of bilayers in which bR was successfully incorporated. The membrane capacitance and the resistance of the bilayer containing bR were extracted by applying an appropriate equivalent circuit to the spectra. Impedance spectra revealed that the membrane resistance is in the $M\Omega cm^2$ range, the capacitance of $0.7\mu Fcm^{-2}$ for the bilayer is in the same range as those obtained for pure tBLMs,

which are in the range of ~0.5μFcm^{-2}. Thus, the capacitances demonstrated the formation of lipid bilayers and the resistances indicated the sealing electrical properties of the bilayers.

To prove the functionality of immobilised bacteriorhodopsin in the tBLMs, light was applied. When the light was on, the membrane capacitance did not change, but the membrane resistance decreased. The functionality of bR insertion was obtained by decrease of membrane resistance from MΩcm^2 range to the some kΩcm^2, indicating the successful incorporation of bR into the tBLMs in an active form. When the light was switched off, the membrane resistance could be recovered, however, in a slow process.

6. Final conclusion

The purpose of the present work was to establish a tBLM based on a mixed monolayer made up from the thiolipid DPTL and a lateral spacer molecule TEGL. To form a lipid bilayer, the DPTL tethers have been mixed with small spacer molecules (dilution molecules) which allow phospholipids to enter both leaflets of the bilayer. Membranes are bound to the gold electrode using thiolipid tethers which are separated from the gold-thiol bond via a glycerol-tetraethyleneoxy chain.

The purpose of using the spacer and the addition of extra spacer molecules between the substrate and the bilayer is that this architecture provides an ionic reservoir underneath the membrane, avoiding direct contact of the embedded membrane proteins with the gold electrodes and at the same time to increase the lateral mobility of the bilayer, thus allowing for the incorporation of complex channels proteins which was not achieved in non-diluted systems.

Varying the mixing ratio, the optimum mixing ratio was obtained at a dilution factor of DPTL and TEGL at 90%:10%. Only under these conditions, the mixed tBLM showed electrical properties, as shown by EIS, which are comparable to a BLM. With higher dilution factors, a defect-free lipid bilayer was not formed.

The relatively small amount of dilution molecules, however, allowed for the incorporation of a number of peptides and proteins in a functionally active form. Channel peptides such as gramicidin, melittin showed activities comparable to freely suspended solid supported membranes. Also α-hemolysin was incorporated in a fully functional form.

However, larger more complex proteins, such as the Maxi-K and the AchR, although incorporated into the lipid bilayer, showed a restricted activity, as shown by the small

effects on the membrane resistance and also by the sluggish responds to external stimuli such as bias potentials, agonists and antagonists. These responses were, however, qualitatively the same as expected from independent measurements.

This is a proof for the incorporation of these proteins in a functionally active form into a very stable tBLM environment. We conclude from this that the mixed tBLM was successfully designed as a general platform for biosensing and screening purposes of membrane proteins.

7. References

1. Singer S.J., Nicolson G.L., *Science*, **1972**, *175*, 720-731

2. Mouristsen, O.G. In Life-as a matter of fate: The Emerging science of lipidomics; Dragomann, D. Dragomann, M. Elitzur, A.C. Silverman, M.P., Tuszynski, J. and Zeh, H.D., Eds.; The Frontiers Collection; Springer: Germany, **2005**; Vol. *1*, pp 27

3. A. Charbit, C. Andersen, J. Wang, B. Schiffler, V. Michel, R. Benz and M. Hofnung, Mol. Microbiol., **2000**, *35*, 777

4. T. K. Rostvtseva, T. T. Liu, M. Colombini, V. A. Parsegian and S. M. Bezrukov, Proc. Nat. Acad. Sci. USA, **2000**, *97*, 7819.

5. M. Akeson, D. Branton, J. J. Kasianowics, E. Brandin and D. W Deamer, J. Biophys., **1999**, *77*, 3227.

6. B. A. Cornell, V. L. Braach-Maksvytis, L. G. King, P. D. Osman, B. Raguse, L. Wieczorek and R. J. Pace, Nature, **1997**, *387*, 580.

7. S. Heyse, T. Stora, E. Schmid, J. H. Lakey and H. Vogel, Biochim. Biophys. Acta, **1998**, *1376*, 319.

8. K. Seifert, K. Fendler and E. Bamberg, Biophys. J., **1993**, *64*, 384

9. T. Stora, J. H. Lakey and H. Vogel, Angew. Chem. Int. Ed. Engl., **1999**, *38*, 389

10. M. Winterhalter, Colloids Surf. A, **1999**, *149*, 547.

11. Banerjee, R. J. Biomater. Appl. **2001**, *16*, 3-21

12. Lasic, D.D. Trends Biotechnol., **1998**, *16*, 307-321

13. Müller, P., Rudin, D.O., Tien, H.T., Wescott, W.C. *Nature*, **1962**, *194*, 979-980

14. Tien, H.T. and Ottova-Leitmannova, A., eds., Elsevier, Amsterdam, **2003**

15. Castillo, J.D., Rodriguez, A., Romero, C.A. and Sanchez, V., Science, **1966**, *153*:185-188

16. Ashcroft, R.G., Coster, H.G.L., Laver, D.R. and Smith, J.R., Biochmica et Biophysica Acta, **1983**, *730*:231-238

17. Fettiplace, R., Andrews, D.M. and Haydon, D.A., J. Membrane Biol., **1971**, *5*:277-

18. Hianik, T., Miklovicova, J., Bajci, A., Chorvat, D. and Sajter, V., Gen. Physiol. Biophys., **1984**, *3*:79-84

19. Coster, H.G.L. and Laver, D.R., Biochim. Biophys. Acta, **1986**, *857*:95-104

20. Hendry, B.M., Urban, B.W. and Haydon, D.A., Biochim. Biophys. Acta, **1978**, *513*:106-116

21. Purrucker, O., Hillebrandt, H., Adlkofer, K. and Tanaka, M., Eletrochim. Acta, **2001**, *47*:791-798

22. Plant, A L, *Langmuir*, **1993**, *9*, 2764-2767

23. Lingler S, Rubinsten I, Knoll W, Offenhäusser A, *Langmuir*, **1997**, *13*, 8085-7091

24. Guidelli, R.; Aloisi, G.; Becucci, L.; Dolfi, A.; Moncelli M.R.; Buoninsegni, F T. *J. Electroanal. Chem.* **2001**, *504,* 1-28.

25. Tien, H.T. and Ottova, A.L., Colloids and Surfaces A. Physicochemical and Engineering Aspects, **1999**, *149*:217-233 (1999).

26. Ide, T. and Yanagida, T., Biochemical and Biophysical Research Communications, **1999**, *265*:595-599

27. Cheng, Y., Boden, N., Bushby, R.J., Clarkson, S., Evans, S.D., Knowles, P.F., Marsh, A. and Miles, R.E., Langmuir, **1998**, *14*:839-844

28. Bunjes, N., Schmidt, E.K., Jonczyk, A., Rippmann, F., Beyer, D., Ringsdorf, H., Gräber, P., Knoll, W., Naumann, R., Langmuir, **1997**, *13*:6188-6194

29. Cornell, B.A., Braach-Maksvytis, V.L.B., King, L.G., Osman, P.D.J., Raguse, B., Wieczorek, L. Pace, R.J., Science, **1997**, *387*:580-583

30. Raguse, B., Braach-Maksvytis, V., Cornell, B.A., King, L.G., Osman, P.D.J.,Pace, R.J. Wieczorek, L., Langmuir, **1998**, *14*:648-659

31. Jenkins, A.T.A., Bushby, R.J., Boden, N., Evans, S.D., Knowles, P.F., Liu, Q., Miles, R.E. Ogier, S.D., Langmuir, **1998**, *14*:4675-4678

32. Schmidt, C., Mayer, M. and Vogel, H., Angew. Chem. Int. Ed., **2000**, *39*:3137-3140

33. Kiessling V, Tamm LK, *Biophys J*, **2003**, *47*, 105-113

34. Sackmann, E., Science, **1996**, ***271***:43-48

35. Tampé, R., Dietrich, C., Gritsch, S., Elender, G. and Schmitt, L., Nanofabrication & Biosystems, Hoch, H.C., Jelinsi, L.W. and Craighead, H.G., eds., Cambridge University Press, Cambridge, **1996**

36. Plant, A.L., Langmuir, **1999**, *15*:5128-5135

37. Lang, H.; Duschl, C.; Vogel, H. *Langmuir,* **1994,** *10,*197.

38. Steinem C, Janshoff A, Goossens J, Galla H-J, *Bioelectrochem Bioenergetics*, **1998**, *45*, 17- 26

39.Naumann, R.; Jonczyk, A.; Kopp, R.; v.Esch, J.; Ringsdorf, H.; Knoll, W.; Gräber, P. *Angew. Chem.,* **1995**, 34, 2056.

40. Williams, L. M.; Evans, S. D.; Flynn, T. M.; Marsh, A.; Knowles, P. F.; Bushby, R. J.; Boden, N. *Langmuir* **1997**, *13,* 751.

41. Naumann R, Schmidt EK, Jonczyk A, Fendler K, Kadenbach B, Lieberman T, Offenhäussser A, Knoll W, Biosens Bioelectronics, **1999**, 14, 651-662

42. Woodhouse, G., E.; King, L., G.; Wiezcorek, L.; Cornell, B., A. *Faraday Disc*., **1998**, *111*, 247

43. Cornell, B., A.; Krishna, G.; Osman, P.,D.; Pace, R.J.; Wieczorek, L. *Biochemical Soc. Transactions*, **2001**, *29*, 613.

44. Schiller, S.M.; Naumann, R.; Lovejoy, K.; Kunz, H.; Knoll, W.; *Angew. Chem. Int. Ed*., **2003**, *42*, 208

45. W.J. Miller,N.L.Abbott, *Langmuir*, **1997**, *13*, 7106

46. Hucho F., Weise C. (2001) *Angew. Chem. Int.* Ed. 40, 3100-3116

47.Hille B. (2001) I*on Channels of Excitable Membranes*, 3rd ed. Sinauer Associates, Inc, Sunderland, Massachusetts.

48. Bayley, H., Cremer, P. S. *Nature*, **2001**, *413*, 226-230
49. Walker, B., Krishnasastry, M., Zorn, L., Bayley, H. *J.Biol. Chem*. **1992**, *267*, 21782-21786

50. Walker, B., Braha, O., Cheley, S., Bayley, H. *Chem. Biol*. **1995**, *2*, 99-105

51. Demspsey, C. E. Biochim. *Biophys. Acta.* **1990**, *1031*, 143

52.Sansom, M.S. Prog. Biophys. Mol. D. Noble and I. Blundell, editors. Pp. 139-235. Pergamon Press, Oxford, England

53. Eisenberg, D., T.C.Terwilliger, and F.Tsui. *Biophys. J.* **1980**, 32:252-254

54. Sarges, R.; Witkop, B. *J. Am. Chem. Soc.* **1965**, *87*, 2011-2020

55. Veatch, W.R.; Fossel, E.T.; Blout, E.R.; *Biochemistry*, **1974**, *13*, 5249-5256

56. Wallace, B.A.; Ravikumar, K.; *Science*, **1988**, *241*, 182-187

57. Woolley, G.A.; Wallace, B.A.; *J. Membrane Biol.* **1991**, *55*, 139

58. Myrta, O, Montal, L, K, Bühler; T, Iwamoto; J, M, Tomich; M, Montal, *J. Biochemistry*. **1993**, *268*, 14601-14607

59. F, J, Raucci. Master Thesis University of Florida

60. S.J.Opella; F.M.Marassi; J.J.Gesell; A.P.Valente, Y.Kim; M.Oblatt-Montal; M.Montal. *Nature Structure Biology*. **1999**, *6*, 374-379

61.Hille B. (2001) I*on Channels of Excitable Membranes*, 3rd ed. Sinauer Associates, Inc, Sunderland, Massachusetts.

62. Moczydlowski, E., Latorre, R. *J.Gen Physiol*. **1983**, *82*, 511-542

63. Talukder, G., Aldrich, R.W. *Biophys.* **2000**, *117*, 253-274

64. Horrigan, F.T., Cui, J., Aldrich, R.W. *J.Gen. Physiol.* **1999**, *114*, 277-304

65. Barrett, J.N., Magleby, K.L., Pallotta, B.S., *J. Physiol*. (London), **1982**, *331*, 211-230

66. Cox, D.H., Cui, J., Aldrich, R.W. *J. Gen. Physiol.* **1997**, *110*, 257-281

67. Larsson, H.P., Baker, O. S., Dhillon, D. S. Isacoff, E.F. *Neuron*, **1996**, *16*, 387-397

68. Wei, A., Solaro, C., Lingle,C., Salkoff,L. *Neuron*, **1994**, *13*, 671-681

69. Knaus, H.G., Folanker, K., Garcia-Calvo, M., Garcia, M.L., Kaczorowski, G. J., Smith, M., Swanson, R. *J. Biol. Chem.*, **1994**, *269*,17274-17278

70. Volgalis, F., Vincent, T., Qureshi, I., Schmalz, F., Ward, M.W., Sanders, K.M., Horowitz, B., *Am. J. Physiol.* **1996**, *271*, G629-G639

71. Wallner, M., Meera, P., Ottolia, M., Kaczorowski, G.J., Latorre, R., Garcia, M.L., Stefani, E., Toro, L. Receptors Channels, 1995, 3, 185-199

72. Changeux, J. P. *Scien. Amer.* **1993**, *1*, 58-62

73. Hille, B. **1992**, Ionic Channels of Excitable Membranes, 2nd ed. Sinauer Associates, Sunderland, MA

74. Karlin, A., Akabas, A. *Neuron*. **1995**, *15*, 1231-1244

75. Grosmann, C., M. Zhou, Auerbach, A. *Nature*, **2000**, *414*, 223.224

76.Boheim, G., Hanke, W., Barrantes, F.J., Eibl, H., Sakmann, B., Fels, G., Maeliche, A. *Proc.Natl. Acad. Sci*. **1981**, *78*, 3586-3590

77. Eray, M., Dogan, D.F., Silber, M., Davis, W.C. *Biosystems*, **1995**, *35 (2)*, 183-188

78. Tien, H.T., Samamon, Z. *Bioelectrochemistry & Bioenergetics*, **1989**, *22(3)*, 211-218

79. Schmidt, E.K., Tieberman, T., Kreiter, M., Jonczyk, A., Naumann, R., Offenhäusser, A., Neumann, E., Kukol, A., Maelicke, A., Knoll, W. *Biosensor & Bioelectronics*, **1998**, *13*, 585-591

80. Liedberg, B., Nylander, C. and Lundström, I., *Sensor and Actuators,* **1983**, *4,* 299-304

81. Pockrand, I., Swalen, J.D., Gordon, J.G. and Philpott, M.R., *Surf. Sci.*, **1978**, *74***,** 237-244.

82. Swalen, J.D., Gordon, J.G., Philpott, M.R., Brillante, A., Pockrand, I. and Santo, R., *Am. J. Phys.*, **1980**, *48*, 669-672

83. Agarwal, G. S. *Physical Review B* **1973,** *8*, 4768-79.

84.(a) Matsuoka, T.; Kuribara, H.; Takubo, K.; Akiyama, H.; et al. *J. Agric. Food Chem.* **2002**,*50*, 2100-2109.
(b) Anklam, E. *Anal. Chim. Acta.* **1999**, *393*, 177-179.
(c) Quist, D.; Chapela, I. H. *Nature* **2001**, *414*, 541.

85. (a) Metz, M.; Futterer, J. *Nature* **2002**, *416*, 10.
(b) Mann, C. C. *Science* **2002**, *295*, 1617.
(c) Quist, D.; Chapela, I. H. *Nature* **2002**, *416*, 11.
(d) Meyer, R. *Food Control.* **1999**, *10*, 391-399.

(e) Wurz, A.; Bluth, A.; Zeltz, C.; Pfeifer, C.; Willmund R. *Food Control.* **1999**, *10*, 385-389.

86. (a) Feriotto, G.; Borgatti, M.; Mischiati, C.; Bianchi, N.; Gambari, R. *J. Agric. Food Chem.* **2002**, *50,* 955-962.
(b) Nielsen, P. -E.; Egholm, M.; Berg, R. -H.; Buchardt, O. *Science* **1991**, 254, 1497-1500.
(c) Egholm, M.; Buchardt, O.; Christensen, L.; Behrens, C.; *Nature.* **1993**, *365*, 566-568.

87. (a) Nielsen, P. -E.; Christensen, L. *J. Am. Chem. Soc.* **1996**, *118*, 2287-2288.
(b) Mugweru, A.; Wang, B. –Q.; Rusling, *J. Anal. Chem*. **2004**, *76*, 5557-5563.
(c) Bottomley, L. -A.; Poggi, M. –A.; Shen, S. –X. *Anal. Chem*. **2004**, *76*, 5685-5689.

88. Knoll. W. *Annu. Rev. Phys. Chem.* **1998,** *49*, 569-638

89. Otto, A. *Z. Physik,* **1968**, *216*, 398-410

90. Kretschmann E, Raether H, Z. *Naturforsch*. **1968**, *23*, 2135-2136

91. J. R. Macdonald, *Impedance spectroscopy*, John Wiley & Sons, New York, **1987**

92. Lyklema, J. *Fundamentals of interface and colloid science Vol.II: solid-liquid interface, Academic press, London*, **1995**

93. Hunter, R.J., *Foundations of colloid science, Oxford University, New York*, **2001**

94. Helmholtz, J.H.L.F. von, *Wiedemanns Ann. (Ann. Phys. Leipzig)*, **1877**, *7*, 377

95. Gouy, M.; *J. Phys.*, **1910**, *9*, 475

96. Chapmann, D. L., *Phil. Mag.*, **1913,** *25*, 474

97. Stern, O., *Zeit, Elektrochem. Angew.Phys.*, **1924**, *30*, 508

98. Meerwall, E. D.; Frank, C. W.; Semerak, S. N.; Koenig, J. L.; *Adv. Poly. Sci*.; Springer Verlag Berlin Heidelberg New York Tokyo, **1984**, 87

99. Wang, X. M.; Gershman, Z.; Kharitonov, A.B.; Katz, E.; Willner, I. *Langmuir*, **2003**, *19*, 5413

100. Uilk, J.M.; Mera, A.E.; Fox, R.B.; Wynne, K.J. *Macromolecules*, **2003**, *36*, 3689-3694

101.Zisman, W.A. *Contact Angle Wettability and Adhesion*, Gould, R.F. (Ed), *Am. Chem. Soc.*, Washington, D.C., 1964

102.Young, T. *Philos.Trans.R.Soc.Lond*,**1805**, *95*, 65

103.Binning, G.; Quate, C.F.; Gerber,C. *Phys. Rev. Lett*. **1986**, *56*, 930-33

104.Capella, B.; Baschieri, P.; Frediani, C.; Micoli, P.; Ascoli, C. *IEEE Eng. Med. Biol. Mag.* **1997**, *16,* 58-65

105.Quate, C.F. *Surf.Sci.***1994**, *299/300*, 980-995

106. Yves, F.; Dufrene. *J. Bacteriology*, **2002**, *184*520

107. Ducker, W.A.; Senden,T.J.; Pashley, R.M. *Nature* **1991**, *353*, 2239-41

108. Israelachvili, J. *Intermolecular & Surface Forces*, 2nd ed.; Academic Press; London, **1991**

109. Giessibl, F. J. *Rev. Mod. Phys*., **2003,** *75,* 949

110. G. Sauerbrey, *Z. Phys*., **1959**, *155*, pp. 206-222.

111. R.Naumann; S.M.Schiller; F.Giess; B.Grohe; K.B.Hartman; I.Kärcher; I.Köper; J.Lübben; K.Vasilev; W. Knoll. *Langmuir* , **2003**, *19*, 5435-5443

112. Moncelli, M.R.; Becucci, L.; Schiller, S.M. *Biolectrochemistry*, **2004**, *63*, 161

113. Terretaz, S.; Mayer, M.; Vogel, H. *Langmuir***, 2003**, *19*, 5567.

114. P.Vitovic; S.Kresak; R.Naumann; S.M.Schiller; R.N.A.H.Lewis; R.N.McElhaney; T.Hianik; *Bioelectrochemistry* **2004**, *63*, 169-176

115. Krishna, G.; Schulte, J.; Cornell, B.A.; Pace, R.; Wieczorek, L.; Osman, P.D. *Langmuir* **2001**, *17*, 4858.

116. Baumgart, T.; Kreiter, M.; Lauer, H.; Naumann, R.; Jung, G.; Jonczyk, A.; Offenhäusser, A.; Knoll, W.; *J. Coll. Interface Science*, **2003**, *258*, 298.

117. Bunjes, N.; Schmidt, E.K.; Jonczyk, A.; Rippmann, F.; Beyer, D.; Ringsdorf, H.; Gräber, P.; Knoll, W.; Naumann, R. *Langmuir*, **1997**, *13*, 6188.

118. Vanderah, D. J. ; Meuse, C. W. ; Silin, V. ; Plant, A.L. *Langmuir* **1998**, *14*, 6916.

119. Krueger, S.; Meuse, C., W. ; Majkrzak, C., F. ; Dura, J., A.; Berk, N. F.; Tarek, M.; Plant, A., L. Langmuir, **2001**, 17, 511.

120. Naumann, R.; Schmidt, E. K.; Jonczyk, A.; Fendler, K.; Kadenbach, B.; Liebermann, T.; Offenhäusser, A.; Knoll, W. Biosens. Bioelectron. **1999**, *14*, 651.

121. Naumann, R.; Baumgart, T.; Gräber, P.; Jonczyk, A.; Offenhäusser, A.; Knoll, W. Biosens. Bioelectr., **2002**, *17*, 25.

122. Glazier, S., A.; Vanderah, D., J.; Plant, A.,L.; Bayley, H.; Valincius, G.; Kasianovic, J. Langmuir, **2000**, *16*, 10428.

123. Madhusudhana, N.; Silin, V.; Ridge, K., D.; Woodward, J.; T.; Plant, A., L. Analyt. Biochemistry, **2002**, *307*, 117.

124. Peggion, C.; Formaggio, F.; Toniolo, C.; Becucci, L.; Moncelli, M.R.;Guidelli, R. Langmuir, **2001**, *17*, 6585.

125. Krysinsky, P.; Zebrowska, A.; Michota, A.; Bukowska, J.; Becucci, L.; Moncelli, M., R. Langmuir, **2001**, *17*, 3852.

126. Becucci, L.; Guidelli, R.; Liu, Q.; Bushby, R., J.; Evans, S., D. J. Phys. Chem. B **2002**, *106*, 10410.

127. Keller, C., A.; Glasmästar, K.; Zhdanov, V. P.; Kasemo, B. *Phys. Rev. Lett*., **2000**, *84*, 5443.

128. Kalb, E.; Frey, S.; Tamm, L., K. *Biochim. Biophys. Acta*, **1992**, *1103*, 307

129. Keller, C.A.; Kasemo, B. *Biophys. J.* **1998**, *75*, 1397-1402
130. Reimhult, E., et al., *Langmuir*, **2003**, *19*, 1681

131. Keller, C.A.; Glasmästar, K.; Zhdanov, V.P.; Kasemo, B. *Phys. Rev. Let.* **2000**, *84* (23), 5443-6.

132. Dufrene,Y.F.; Boland, T; Schneider, J.W.; Barger,W.R.; Lee, G. U. *Faraday Discuss.* **1998**, *111*, 79-94

133. Schneider, J., Barger, W., Lee, G. U. *Langmuir*, **2003**, *19*, 1899-1907

134. Schneider, J., Dufrene, Y. F., Barger, W.R., Lee, G. U. *Biphys. J.* **2000**, *79*, 1107-1108

135. Richter, R.P.; Brisson, A. *Langmuir*, **2003**, *19*, 1632-1640

136. Franz, V.; S. Loi; H. Müller; E. Bamberg, and H. J. Butt, *Colloids & Surfaces B. Biointerfaces*, **2003**, *23*, 191-200

137. Loi, S.; G, Sun.; Franz, V.; Butt, H. J.; *Phys. Rev. E.*, **2002**, *66*, 031602-031602/7

138. Schneider, J., Barger, W., Lee, G. U. *Langmuir*, **2003**, *19*, 1899-1907

139. Müller, H., Butt, H. J., Bamber, E., *Biophys. J.*, **1999**, *76*, 1072-1079

140. White, S.H., Wimley, W.C. Biochim. *Biophys. Acta.* **1998**, *1376*, 339-352

141. Killian, J. A. Biochim. *Biophys. Acta.* **1998**, *1376*, 401-415

142. Pawlak,M; Stankowski,S.; Schwarz, G.; *Biochim. Biophys.Acta,* **1991**, *1062*, 94.

143. Moncelli, M.R.; Becucci, L.; Schiller, S.M. *Biolectrochemistry*, **2004**, *63*, 161

144. Becucci, L.; Moncelli, M., R.; Guidelli, R *Langmuir*, **2003**, *19*, 3386

145. Trasatti, S.;Lust, E. In Modern Aspects of Electrochemistry, White, R.E. Bockris, J.O'M., Conway, B.E. Eds. Kluwer/Plenum: New York, **1999**, Vol. *33*, p.1.

146. Sancho M. Solid State Ionics, 1997, 97, 63-74.

147. Nikolelis D, Siontorou C. *Analytical Chemistry*, **1996**, *68*, 1735-1741.

148. Hirano A, Wakabayashi M, Matsuni Y, Sugawara M. *Biosensors & Bioelectronics*, **2003**, *18*, 973-983.

149. Steinem, C., Janshoff, A., Galla, H.-J., Sieber, M. *Bioelectrochem.* **1997**, *42*, 213.

150. Vallejo, A.E., Gervasi, C.A., *Bioelectrochem.*, **2002**, *57*, 1.

151. Marty, A. *Nature* **, 1981**, *291*, 497-500

152. Barrett, J. N., Magleby, K.L., Pallotta, B. S. *J. Physiol*. **1982**, *331*, 211-230

153. Knaus, H. G., McManus, O.B., Lee., S.H., Schmalhofer, W.A., Garcia-Calvo, M., Helms, L.M.H., Sanchez, M., Giangiacomo, K., M., Reuben, J.P., Smith, A.B.III, Kaczorowski, G.J., Garcia, M. L. *Biochemistry*, **1994b**, *33*, 5819-5828

154. Changeux, J. P. *Scien. Amer.* **1993**, *1*, 58-62

155. Hille, B. **1992**, Ionic Channels of Excitable Membranes, 2nd ed. Sinauer Associates, Sunderland, MA
156. Karlin, A., Akabas, A. *Neuron*. **1995**, *15*, 1231-1244

157. Grosmann, C., M. Zhou, Auerbach, A. *Nature*, **2000**, *414*, 223.224

158. Boheim, G., Hanke, W., Barrantes, F.J., Eibl, H., Sakmann, B., Fels, G., Maeliche, A. *Proc.Natl. Acad. Sci*. **1981**, *78*, 3586-3590

159. Eray, M., Dogan, D.F., Silber, M., Davis, W.C. *Biosystems*, **1995**, *35 (2)*, 183-188

160. Steifer, K., Fendler, K., Bamberg, E. *Biophys. J*. **1993**, *64*, 384-391

161. Bamberg, E., Apell, H.-J., Dencher, N.A., Sperling, W., Stieve, H., Läuger, P. *Biophys. Struct. Mech*. **1979**, *5*, 292-312

162. Puu, G.., Gustafson, I., Artursson, E., Ohlsson, P.A., *Biosens.Bioelelctron*. **1995**, *10*, 463-479

163. Steinem, C., Janshoff, A., Höhn, F., Sieber, M., Galla, H.-J. *Chemistry & Physics of Lipids,* **1997**, *89*, 141-152

164. L.He, J.Robertson, J.Li, I.Kärcher, S.M.Schiller,W.Knoll,R.Naumann, *Langmuir* **2005**, *21* 11666-11672

8. Appendix

8.1 Materials

• Thiolipid and spacer molecule

2,3-di-*O*-phytanyl-sn-glycerol-1-tetraethylene glycol-D,L-α-lipoic acid ester lipid (DPTL) was synthesized as described earlier[44]. Tetraethylene glycol-D,L-α-lipoic acid ester (TEGL) was synthesized as described by He *et al*.[164] TEGL is soluble in methanol, ethanol, and trifluorethanol but has a tendency to oxidize after which it dissolves only after prolonged stirring of the suspension. Only monomers are found in the solution with no indication of higher oligo- or polymers.

• Lipids

The lipids used in this work 1,2-diphythanolyl-sn-glycero-3-phosphocholine (DPhyPC), 1,2-diphytanoyl-sn-glycero-3-phosphate (DPhyPG), and cholesterol were supplied from Avanti Polar Lipids, Inc., Alabaster, Al, USA.

• Salt

Sodium chloride (NaCl) was from SigmaUltra; Potassium chloride (KCl), Calcium chlorid ($CaCl_2$); and N-(2-Hydroxyethyl) piperazine-N'-(2-ethanesulfonic acid) (HEPES) were obtained from Sigma-Aldrich;

• Proteins

Gramicidin from *bacillus brevis* were purchased from Sigma-Aldrich; melittin was supplied from Fluka, Buchs, Switzerland; α-hemolysin was provided by Dept. of Medical Biochemistry and Genetics, Texas A & M Health Science Center, USA:; M2 was received from Mc Knight Brain Institute, University of Florida, USA.; Maxi-K was provided from University of Florida; USA; Nicotinin acetlcholine receiptor from *T.californica* was provided from Institut für Chemie-Biochemie, Freie Universität, Berlin and bacteriodophosin were provided from MPIP Mainz.

• **Solvents**

Ethanol (pure), Chloroform, Methanol and Aceton were purchased from Riedel, Germany. For cleaning purpose and for the buffer preparations, purified water (>18 MΩ cm) from a Milli-Q (Millipore, Inc) system was used throughout.

• **Buffers**

For melittin-containing bilayers, the SAMs were placed in a buffer solution of NaCl (140 mM), KCl (6 mM), HEPES (10 mM) pH 7.4 and mixed liposomes were added for a final lipid concentration of 0.04 mg/ml. Vesicle fusion was monitored by SPR and, shortly before the kinetic trace reached saturation, 20 µl of a melittin stock solution (0.65 mg/ml in ethanol ≡ 2.28×10^{-4} M) was added to 1 ml of the bathing solution to obtain a final concentration of 4.57×10^{-6} M.

For gramicidin containing bilayers, SAMs were placed in a buffer solution of KCl (50 mM), HEPES (10 mM) pH 7.4 and mixed liposomes were added for a final concentration 0.04 mg/ml. Vesicle fusion was monitored by SPR and, shortly before the kinetic trace reached saturation, gramicidin was added to a final concentration of 4×10^{-7} M in the bathing solution, from a stock solution (8×10^{-5} M) in ethanol.

For M2-containing bilayers, the SAMs were placed in a buffer solution of NaCl (140 mM), KCl (6 mM), HEPES (10 mM); pH 7.4 and mixed liposomes were added for a final lipid concentration of 0.04 mg/ml.

For Maxi-K containing bilayer, SAMs were placed in a buffer solution of KCl (150 mM), NaCl (6 mM), HEPES (10mM), $CaCl_2$ (2mM); pH 7.4 and liposome mixture for a final concentration of 0.04 mg/ml and 20µl Maxi-K containing vesicle were added to the cell so as to form a bilayer.

For AChR containing bilayer, SAMs were placed in a buffer solution of NaCl (140 mM), KCl (6 mM), HEPES (10mM); pH 7.4 and liposome mixture for a final

concentration of 0.04 mg/ml and 200µl AChR containing fragments (0.5 mg/ml) were added to the cell so as to form bilayer.

8.2 Sample preparation

- **Preparation of the template stripped gold (TSG)**

Silicon wafers were carefully cleaned with NH_3 : H_2O_2 : H_2O in 1:1:5 ratio mixed solution at 75°C for 15 min, then extensively rinsing with Mill-Q water. The cleaned silicon wafers were deposited with 50 nm thick gold films on top by electrothermal evaporation (rate 0.01 nm/sec -0.05 nm/sec, 2×10^{-6} mbar) under vacuum in a commercial instrument (Edwards). Gold films on silicon wafers were then glued with EPO-TEK 353ND-4, (n=1.5922 at 633 nm) to LaSFN9 glass slides and cured for 60 min at 150°C. The silicon wafers were detached from the gold film immediately before use.

- **Preparation of the SAMs**

0.2 mg/ml DPTL and 0.02 mg/ml TEGL were dissolved in ethanol to prepare a mixed assembly solution as both of them are soluble in ethanol. Template stripped gold (TSG) slides were then placed in the mixed assembly solution at room temperature for 24 hours to tether the monolayer. The samples were then rinsed in ethanol and dried in a stream of nitrogen. The slide was immediately mounted to an electrochemical cell for using.

- **Preparation of the liposome mixture**

The mobile lipid leaflet (out layer) was then formed by fusion of liposome mixture. In this work, the assay depends on a source of unilamellar vesicles prepared under standard conditions to ensure maximum reproducibility. A phospholipid mixtures composed of 1,2-diphythanolyl-sn-glycero-3-phosphocholine (DPhyPC), 1,2-diphytanoyl-*sn*-glycero-3-phosphate (DPhyPG) and cholesterol in molar ratio 6:3:1 were used. The lipid mixture was dissolved in chloroform and stored in a

refrigerator as a stock solution. The solvent was evaporated to give a dry lipid film. The lipid film was then dissolved in Milli-Q water and the residue was hydrated at 40°C at a concentration of 1 mg lipid/ml for 4 hours. Thereafter liposomes were prepared by extrusion through a 50 nm polycarbonate filter. The solution was then diluted with Milli-Q water to a final concentration 0.2 mg/ml.

- **Preparation of quartz crystals**

The QCM crystals were taken directly from the manufacturers and cleaned before depositon of a surface overlay. The quartz crystals were either immersed in a 6:1:1 (vol:vol:vol) solution of H_2O: NH_3 (25%):H_2O_2 (30%) and heated to 70°C for 10 min followed by thorough rising with milli Q water and drying in a stream of nitrogen gas, or subjected to an oxygen plasma of 350 W for 10 min. Both processes create a cleaned surface for preparation of self assembled monolayer.

After cleaning, the crystals were first functionalized with a self-assembled monolayer (SAM) of thiolipids and dilution molecule. After the gold electrode of the quartz crystal was immersed for 24h in the mixed thiol solution, it was rinsed with ethanol, dried in a stream of nitrogen gas. Then quartz plates were mounted into QCM reaction chamber, filling with buffer for further investigation.

8.3 Characterizaton methods

- **Surface plasmon resonance spectroscopy (SPR)**

SPR measurement is carried out with a setup shown in Figure8.1. In brief, a HeNe laser beam is mechanically chopped at a frequency of 1150 Hz and then passes though two polarizers. The second polarizer generates a plane wave with the desired polarization, whereas, the first one is used for the attenuation of the laser. The reflected beam is collected and focused onto a photodiode. The incident angle (θ) is varied by rotating the prism sample on a fine goniometer with an angle resolution of 0.001 degree. The collection lens and the detector are rotated by an angle of 2θ in

order to catch the reflected light. The output of the photodiode circuit is sent to a lock-in amplifier to demodulate the signal voltage. In this method, a curve of reflectivity versus incident angle is obtained.

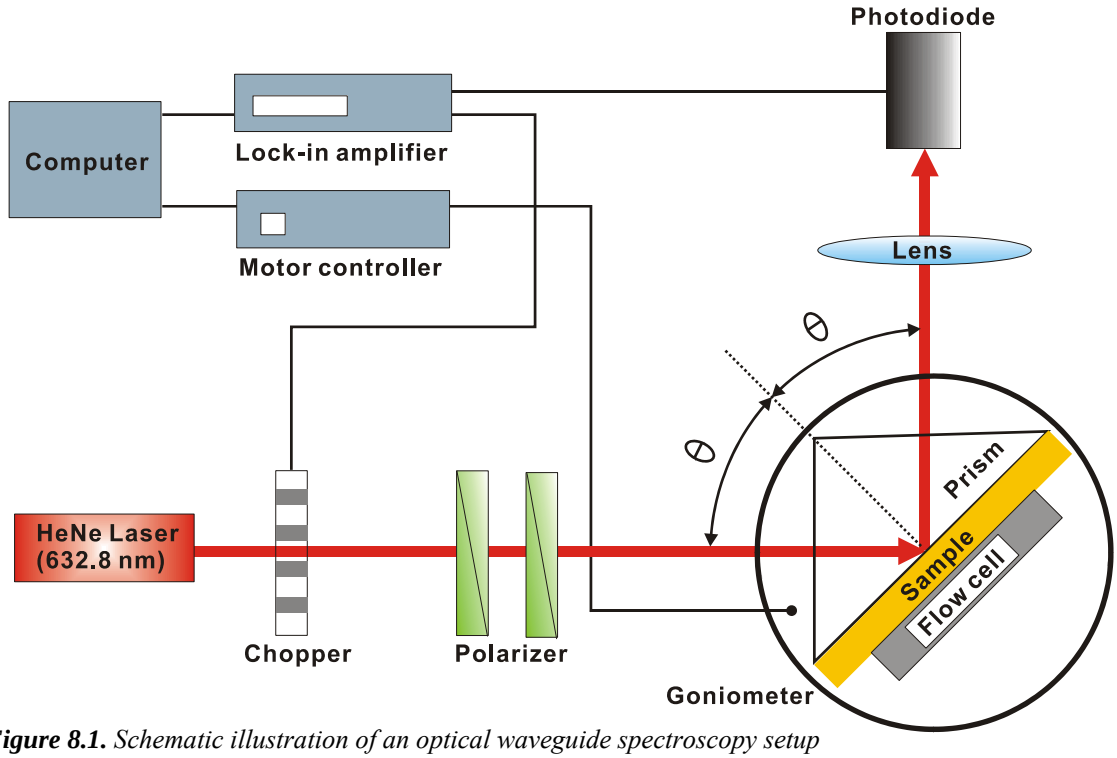

Figure 8.1. *Schematic illustration of an optical waveguide spectroscopy setup*

LaSFN9 glass slides (n = 1.844) are used as substrates for SPR measurements. On one side Au film is evaporated with certain thickness. The other side of the glass slide is optically matched to the base of a LaSFN9 glass prism (n = 1.844 at λ = 633 nm) by using a refractive index oil (n = 1.700). This allows for the excitation of evanescent waves at the metal/dielectric interface, upon the total internal reflection of a laser beam (λ = 633 nm, power ca. 5 mW) at the prism base. The usual reflectivity scan, R versus θ, is achieved by monitoring the reflected light intensity as a function of the incident angle. If the reflected intensity (at a fixed angle near the SPR angle) is recorded as a function of time, kinetic information about interfacial changes can be monitored. Another approach to obtain kinetic information is to follow the angle shift by tracking the minimum of a reflectivity dip, which is suitable for large angle shifts.

- **Electrochemical impedance spectroscopy (EIS)**

EIS experiments were performed with an EG&G 273 potentiostat/galvanostat equipped with a Solartron 1260 frequency response analyzer. Potential control and data collection were obtained with the Zplot/Zview software package (Scribner Associates, Inc). A three-electrode setup was employed using a Pt wire counter electrode and a reference electrode Ag|AgCl, 3 M KCl. Experiments were performed in the buffer solutions described above for the different channel peptides.

Data analysis was performed by utilizing the equivalent circuit-fitting algorithm included in Zview. Data are fitted using the simplest model that adequately describes the data. To account for a distribution of time constants a constant phase element (CPE) was used. The CPE has the general form

$$Z_{CPRE} = (A_{CPE}\, j\omega)^{-\alpha} \qquad \text{Equ. 24}$$

where Z_{CPE} is the frequency dependent impedance of the CPE, A_{CPE} is the software determined fit value with units ($F\ cm^{-2}\ \alpha$), ω is the frequency in rad/s and α represents the deviation from a pure capacitor (when $\alpha = 1$, A_{CPE} becomes a capacitance).

- **Quartz crystal microbalance (QCM)**

Vesicle fusion and adsorption kinetics measurements were taken using QCM-D setup. The general design for all home-built cells is with the sensor crystal vertically aligned with the inlet and outlet, and a rapid (static) exchange of the bulk liquid by gravitational flow from a cup mounted on top of the cell. The QCM-D cell used for optimum performance with respect to baseline stability and temperature control was the commercial Q-Sense QAFC 302 cell, with the QE 301 electronics unit, but also an earlier prototype cell from Q-Sense of simpler design, but similar measurement volume and geometry, was used. The commercial cells have sample volumes of ~50 µl. The cell designed for combined SPR and QCM-D measurements had a sample volume of ~300 µl, while older cells for 1-inch crystals had sample volumes of >500 µl.

- **Atomic force microscopy (AFM)**

The setup used for AFM measurements was a commercial AFM (PicoSPM; Molecular Imaging, Inc.) equipped with a large area scanner (100 .100 μm2). All imaging was done on SAMs described above. An outer bound for the tip shape was obtained by scanning the tip across a tip-characterization grating (TGT01; MikroMasch, Estonia) and subsequently applying a blind recon struction algorithm, as originally suggested by Villarrubia 311 and as implemented in a slightly modified version in the Scanning Probe Image Processor (SPIP; Image Metrology, Denmark), to the recorded image.

AFM measurements were performed in liquid using a Nanoscope IV-Multimode (VEECO, Dourdan, France), equipped with a J-scanner (120 μm). Before using, the tapping mode fluid cell was rinsed in successive baths of ethanol and ultrapure water, followed by extensive rinsing in ethanol and blow-drying in a stream of nitrogen. Tubings and O-ring were sonicated in ethanol and water, rinsed with ethanol and blow-dried in nitrogen. Then the gold substrate with coated self-assembled monolayer was mounted to AFM setup, and the liposome mixtures were then added so as to form a bilayer. After at least 40 min. to check the formation of a bilyer, AFM images and force measurements were carried out by tapping mode.

- **Contact angle**

Experimentally, a 2 μl drop is recorded with a camera, while standing on the surface. The experimental setup used is DSA 10 from Krüss CA, Germany. The shape of the droplet is simulated with the software, Drop Shape analysis v1.5, and gives the static contact angle as a mean value of the angle of each side of the droplet. In average, five measurements were used per slide to obtain a mean value of the contact angle.

List of abbreviations

AFM	Atomic force spectroscopy
BLM	Bilayer lipid membrane, Black lipid membrane
bR	Bacteriorhodopsin
DPhyPC	1,2-diphythanolyl-sn-glycero-3-phosphocholine
DPhyPG	1,2-diphytanoyl-sn-glycero-3-phosphate
DPTL	2,3-di-O-phytanyl-sn-glycerol-1-tetraethylen glycol-DL-α-lipoic acid ester lipid
EIS	Electrochemical impedance spectroscopy
HEPES	N-(2-Hydroxymethyl) piperazin-N'-2-ethansulfic acid
LB	Langmuir-Blodgett
nAchR	Nicotinic acetylcholine receptor
psBLM	Polymer-supported bilayer lipid membrane
QCM	Quartz crystal microbalance
SAM	Self-assembled monolayer
sBLM	Supported bilayer lipid membrane
SPR	Surface plasmon resonance
SPFS	Surface plasmon resonance fluorescence spectroscopy
tBLM	Tethered bilayer lipid membrane
TEGL	tetraethylene glycol-D,L-α-lipoic acid ester
TSG	Template stripped gold